Spectroscopy of the Solar Corona Using Ground and Space-based Observations

A thesis submitted for the degree of

Doctor of Philosophy

in

The Department of Studies in Physics,
Mangalore University,
Mangalagangotri - 574 199, India

by

Maya Prabhakar

Indian Institute of Astrophysics
Bengaluru - 560 034, India

March 2023

Spectroscopy of the Solar Corona Using Ground and Space-based Observations

Maya Prabhakar

Indian Institute of Astrophysics
Bengaluru-560 034, India

Title of the Thesis :	**Spectroscopy of the Solar Corona Using Ground and Space-based Observations**

Name of the author :	**Maya Prabhakar**
Address :	Indian Institute of Astrophysics
	Bengaluru - 560 034, India
Email :	maya.prabhakar@iiap.res.in

Name of the supervisor :	**Prof. K.P Raju**
Address :	Indian Institute of Astrophysics
	Bengaluru - 560 034, India
Email :	kpr@iiap.res.in

Declaration of Authorship

I hereby declare that the thesis entitled "Spectroscopy of the Solar Corona Using Ground and Space-based Observations" is the results of the investigations carried out by me under the guidance of Prof. K.P Raju at the Indian Institute of Astrophysics, Bengaluru, India. I further declare that this thesis work has not been submitted elsewhere for the award of any degree or diploma or any other similar title to any other university or institution.

Date:

Place: Bengaluru **Maya Prabhakar**

Certificate

This is to certify that the thesis entitled "Spectroscopy of the Solar Corona Using Ground and Space-based Observations" submitted by Ms Maya Prabhakar to Mangalore University for the degree of Doctor of Philosophy in Physics is a bonafide record of the research work carried out by her at the Indian Institute of Astrophysics, India under my guidance and direct supervision. I further certify that this thesis or part of thereof has not been the basis for the award of any other degree or diploma or such other similar title of any other university or institution.

Date:

Place: Bengaluru **K.P RAJU**

List of Publications

Refereed:

- *Line Profile Studies of Coronal Active Regions in FeXII λ195.12 Using Hinode/EIS*, Maya Prabhakar & K.P Raju, 2022, The Astrophysical Journal, Volume 931, 40

  DOI: https://doi.org/10.3847/1538-4357/ac610e

- *Characteristics of the Solar Coronal Line Profiles from Fabry-Perot Interferometric Observations*, Maya Prabhakar, K.P Raju & T. Chandrasekhar, 2019, Solar Physics, Volume 294, 26

  DOI: https://doi.org/10.1007/s11207-019-1409-7

Manuscripts in preparation:

- *Dynamics of the coronal holes in FeXII λ195.12 Using Hinode/EIS*, **Maya Prabhakar** & K.P Raju

Conference Proceedings

International:

- Asia Pacific Solar Physics Meeting, 3 - 7 February 2020, Inter-University Center for Astronomy & Astrophysics, Pune, India

  Title: Study of the Physical Properties of the solar corona from EIS/Hinode observations

  Nature of presentation: Poster

  Authors: Maya Prabhakar, K.P Raju

- Exploring the universe: Near Earth Space Science to Extra-Galactic Astronomy, 14 - 17 November 2018, S. N. Bose National Centre for Basic Sciences, Kolkata, India

  Nature of presentation: Poster

  Title: Exploring the inner solar corona through Fabry-Perot interferometric studies

  Authors: Maya Prabhakar, K.P Raju

National:

- 40th Annual Meeting of the Astronomical Society of India(ASI), 25 - 29 March 2022, Indian Institute of Technology, Roorkee, India

  Nature of presentation: Poster

  Title: Coronal active regions' line profile studies from Hinode/EIS in Fe XII 195.12Å

  Authors: Maya Prabhakar, K.P Raju

- Young Astronomers Meet, India(ASI) September 24 - 28, 2018, Physical Research Laboratory, Ahmedabad, India

  Nature of presentation: Poster

  Title: Fabry-Perot interferometric studies of the solar coronal line profiles

  Authors: Maya Prabhakar, K.P Raju

In loving memory of

my father

Acknowledgements

It is an overwhelming feeling to have reached this stage of remembering and thanking each and every one who has helped me in various ways during my research journey. Words can never express how immensely grateful I am to all of them.

My research journey started with joining Prof. K.P Raju for an internship project on spectroscopic studies of the solar corona after my master's. Working with him not only introduced me to research life but also gave me the confidence to continue in astrophysics. When I decided to pursue PhD in solar physics, I could not think of anybody else but him to mentor me. His nature of functioning professionally with clear boundaries has built my personality all through these years. I am indebted to his immense patience, time and freedom that he has given me to discuss anything. He has always encouraged me in trying and achieving whatever I wished for. I must mention that he has been more than a supervisor to me.

This work is funded by the Department of Science & Technology and I thank them for providing financial support to carry out this project. I am thankful to the former Director of IIA, Prof. Sreekumar P for accepting me as a Woman Scientist Fellow and the present Director Prof. Annapurni Subramaniam, who has been helpful during my tenure particularly in communicating with the Department of Science & Technology. I am thankful to her for providing me with extensions. I am grateful to the Dean Prof. Eswar Reddy who has been extremely understanding and kind, especially with the funding matters. I appreciate the Board of Graduate Studies, IIA and Prof. Maheshwar Gopinathan for communicating and easing my tasks in dealing with Mangalore University administrative issues and facilitating my synopsis and thesis submissions.

I am thankful to the Director of ARIES, Prof. Dipankar Banerjee, for his support and encouragement during this journey. I am immensely grateful to Prof. Nat Gopalswamy, GSFC, NASA who mentored me during the COSPAR Capacity Building Workshop. He introduced me to the topics of flares and CMEs which I intend to explore in the coming years. He has guided me in academic scenarios whenever needed. Prof. Sunethra Giridhar, who mentored me during the Indo-French Astronomy School - 5 has to be remembered here for her patience in introducing me to the topics of stellar spectroscopy. She has been a passionate teacher who taught me to expand my understanding of spectroscopy to explore stellar spectroscopy. I thank Prof. K.B Vijay Kumar from Mangalore University for his guidance and support in dealing with the university formalities. I thank Profs. Ganesh Sanjeev, Y. Narayan, and V. Ravindrachary from the Department of Physics, Mangalore University for being extremely helpful. I take this opportunity to thank my teachers Dr Ashok Lamani, Kuvempu University and Mr Srinivasa Murthy, VVNL PU College, Jog for their faith in me. They have always encouraged me to do better.

I thank my friendly seniors Anantha, Amit, and Samyaday for helping and guiding me. Special thanks to Drs. Avijeet and Chandrashekar who have spent hours teaching me and being around

anytime I needed. The journey would not have been possible without Drs. Bibhuthi and Ritesh. They have been my go-to people for understanding concepts may it be solar physics or IDL. I thank Dr Vema Reddy for his classes on IDL during the covid times and Dr Anusha for her constant encouragement. I acknowledge the computer and data centre staff Mr Fayaz, Mr Ashok and Mr Anish for helping me out with various computer-related issues.

I thank Drs. Akanksha, Nancy, Pavana and Bhoomika for their constant support which has made my journey in IIA cherishable. I would not have reached this stage without the constant support, encouragement, and cooperation of Soumya and Manika. They have made my academic life less painful by being there during my tough times. I thank Drs. Raghubar and Meenakshi who were always there in my last-moment problems. My friends Dr Avyarthana, Debesh, Satabdwa and Sarthak cannot be spared from this list. Many thanks to Prateek for helping me format my thesis with his eagle eyes and Shivani for being the source of my fun during this phase. My friends from Mangalore University Dr Vijeth and Yashaswini are thanked for making my life at Mangalore University memorable and helping me in handling the long-distance administrative issues.

This PhD would not have been possible without my beloved father whom I wished lived longer to see this coming. I cherish his deep involvement in teaching me physics and mathematics. Without him, I would not have dreamed of making a career in astrophysics. I dedicate this thesis to him who dedicated his life to me. I thank my mother for pushing me to accomplish my dreams. She has been my strength to reach this phase. I thank her for being my support. She has surprised me with her courage during this journey. Special thanks to all my cousins and buddies Mala and Pooja who were always there to hear me out during this long tiring phase.

March 2023 Maya Prabhakar

Data Usage Acknowledgements

This paper is based on data acquired from Hinode/EIS. Hinode is a Japanese mission developed and launched by ISAS/JAXA, collaborating with NAOJ (Japan) as a domestic partner, NASA (USA) and STFC (UK) as international partners. Scientific operation of the Hinode mission is conducted by the Hinode science team organized at ISAS/JAXA. This team mainly consists of scientists from institutes in the partner countries. Support for the post-launch operation is provided by JAXA and NAOJ, STFC, NASA, ESA (Europe), and NSC (Norway).

Abstract

The outer solar atmosphere, the corona, is known for its million-degree temperature. The mystery surrounding the source of this high temperature is gradually being resolved with various theories, observations and models. However, the quest continues and the attempts to understand its detailed dynamics are in progress. Spectroscopy is a widely used technique to study the physical features of astronomical objects. The spectral line profile parameters are obtained and their features are examined. In this project, the coronal spectra from ground-based Fabry-Perot interferometric observations and space-based Hinode/Extreme ultraviolet Imaging Spectrometer (EIS) observations are studied. The various regions of the solar corona like active regions and coronal holes are analyzed. The primary aim is to study the intensity, Doppler velocity, line width and centroid, their inter-dependencies and their spatial and temporal variations.

The Fabry-Perot interferograms were obtained during the total solar eclipse of 21 June 2001, observed from Lusaka, Zambia. The duration of the totality was 3 min 37 sec during which 14 interferograms were obtained. EIS is one of the three instruments onboard Hinode which observes the solar corona in the EUV band. The data can be obtained from different regions like the active regions, quiet sun, coronal holes, flares, prominences etc. in different wavelengths. Solarsoft/Interactive Data Language (IDL) is used for the data analysis.

In the analysis using both the data, the Doppler velocity and the centroid obtained from the line profiles are mainly emphasized. It is observed that most of the line profiles have multiple components. A line profile is simulated by adding a stationary main component and a varying subsidiary component. The intensity, Doppler velocity and line width of the subsidiary component are changed to see how these two parameters affect the resultant Gaussian.

The primary findings from the Fabry-Perot interferograms analysis are the variation of the above-mentioned parameters during the totality and their correlations with the line width and the radial height. The nature of line profiles is studied in detail and it is seen how multiple components introduce asymmetry in them. The EIS spectral data were used to study the coronal active regions spread globally over the Sun for a duration of 13 years. The focus is on the Doppler velocity, centroid and line width, their inter-dependencies and cross-correlations with the solar cycle 24. The study is further extended to the coronal holes as well.

Outline of the Thesis

The primary motive of the thesis is to examine the dynamic nature of the solar corona. In the first chapter, a general introduction to the Sun and solar corona is given with an emphasis on their various physical features and why it is important to study them. In chapter-2, the details of line profile behavior and how they can be simulated to understand the properties of individual components are briefed. This gives information on the flows and the temperature of the source. The focus is on how the line profile analysis is useful in understanding the physical characteristics of the solar corona. Chapter-3 deals with the Fabry-Perot interferograms obtained from the ground-based observation of a total solar eclipse. The coronal line profiles are analyzed and the results are discussed. In chapter-4, the work on the line profile studies of the coronal active regions using the EIS data is reported. This is followed by chapter-5 on line profile studies of the coronal holes using similar data. The last chapter includes the conclusions and future studies.

Chapter 1: Introduction

This chapter describes the solar properties, its structure and the features of each of its layers. The solar coronal nature and dynamics are included in detail. The present understanding of the solar corona has come a long way. The topics on how one can study the solar corona using total solar eclipses and coronagraphs are elaborated. The early understanding of the corona with primitive instruments and how our understanding has changed gradually are mentioned. This would bring us to our current understanding of the corona and the present-day instruments. Here, the major solar instruments, both ground and space-based, which play a major role in studying our host star are briefed.

Chapter 2: Coronal Spectroscopy & Emission Line Profile Simulations

This thesis deals with the emission line profiles obtained from the solar coronal spectra. The basic principles of coronal spectroscopy and different types of spectrometers are mentioned. The emphasis is mainly on the variation of the Doppler velocity and the centroid of the line profile. It is important to understand how these two parameters are extracted and how they differ from each other. The earlier reports indicate that the majority of the line profiles have multiple components. In order to understand the behavior of the components, a line profile is simulated by adding a stationary main component and a varying subsidiary component. The intensity, Doppler velocity and width of the subsidiary component are changed to see how these two parameters affect the resultant line profile. This helps in getting information on the flows and temperature of the solar atmosphere and structures like coronal loops.

Chapter 3: Fabry-Perot Interferometric studies of the Solar Corona in the green line Fe XIV λ5303

This chapter is based on our paper "Characteristics of the Solar Coronal Line Profiles from Fabry-Perot Interferometric Observations" which is published in Solar Physics. Here, the details of the Fabry-Perot interferometer, and how it is designed and used to study the solar corona are explained. The circumstances of the total solar eclipse of 21 June 2001 during which the interferograms were taken are given. This is followed by the methodology of calibrating and analyzing the data. Further, the results along with their relevance are reported. A comparison of the results with similar studies is also mentioned. It is concluded by pointing out the need for further studies using space-based data like Hinode/EIS to have a better understanding of the physical parameters mentioned above.

Chapter 4: Studies of the Coronal Active Regions in Fe XII λ195.12 using Hinode/EIS

It is important to study the solar corona in EUV as this is the region in which the coronal emission dominates. Hinode is an ideal instrument for this purpose. The different types of EIS data from various coronal regions are briefed. The data considered include the coronal active regions starting from the time of the launch of Hinode in October 2006 till 2019, which covers the last two years of solar cycle 23 and solar cycle 24. This chapter is based on our paper "Line Profile Studies of Coronal Active Regions in FeXII λ195.12 Using Hinode/EIS" which is published in The Astrophysical Journal. The data extraction and analysis procedures are reported. Further, the results are discussed which are mainly concerned with the shifts seen in the centroid and the Doppler velocity with respect to the line width. The correlation of the former two parameters with the latter and with the solar cycle is also explained. The results are compared with similar works using EIS and other major space-based data.

Chapter 5: Dynamics of the coronal holes in FeXII λ195.12 using Hinode/EIS

This chapter deals with studies of the coronal holes for a duration of 13 years, covering the last two years of the solar cycle 23 and the full solar cycle 24. The behaviour of line profile parameters intensity, Doppler velocity, line width and centroid are explained in the coronal holes spread across the Sun. Various cases of the shifts seen in the centroid and the Doppler velocity with respect to the line width are discussed. A comparison of these results with the different shifts observed in the active regions is also reported.

Chapter 6: Conclusions

This chapter deals with the conclusions of our study. The aim of the thesis is to study the two most important and connected problems in astronomy, namely, solar coronal heating and the acceleration of solar wind. The solar cycle variation of the physical parameters of the solar corona is also studied. Two different emission lines are used in the observations which gives an opportunity to study the solar corona at two different levels. A line profile is simulated by combining a stationary main component and a varying subsidiary component. The intensity, velocity and line width of the subsidiary component are varied and the resultant profile is examined. Simulation studies show that the input parameters of the two components affect the resultant profile. The main emphasis of the study is to examine the variation of the line profile parameters like intensity, line width, non-thermal width, Doppler velocity, asymmetry and line centroid in different coronal regions like the active regions and the coronal holes. The inter-dependence of the line profile parameters and their variation with the coronal magnetic activity are studied. It has been shown that the coronal line profiles, in general, contain multicomponents. An excess of blueshifts over redshifts is seen in the line profiles. The results give valuable inputs to the understanding of coronal heating, acceleration of solar winds and solar irradiance. The work will be extended by studying other coronal regions like quiet sun, flares, prominences etc. from EIS data. Similar studies can also be carried out with data from other solar space missions like IRIS, SDO, Aditya-L1 etc.

Contents

List of Figures

List of Tables

Chapter 1

Introduction

1.1 How it all Started?

Our host star, the Sun has been nourishing us for ages. It has held man's curiosity all the time. Sten Odenwald, an astronomer, says that we study the Sun because it is the brightest thing around and it provides us light and heat, which gives wonderful climates.

It is known that ancient humans thought themselves to be at the centre of everything. They held themselves responsible for everything in the eternal cycle. Many civilizations had some sort of belief considering the Sun as a deity or as a supernatural force.

Sun as a deity can be found in ancient Egyptian civilization in the 14^{th} century B.C.E. Sun worshipping was common for the Pagan religion. Solar motifs are often found in cultures across the world. Some religions were formed with the Sun as their primary deity, like the Egyptian, Indo-European and Meso-American etc. The Egyptians, Babylonians, Greeks and Hindus worshipped Re, Shamash, Helios and Surya respectively.

In Hinduism mythology, Surya is the father of many illustrious sons like Manu (progenitor of the human race), Yama (God of the dead), the Ashvins (twin physicians to the Gods), Karna (Mahabharata), and Sugriva (Ramayana). Surya was considered so powerful to dispel darkness and cure diseases. Surya is invoked by most Hindus in many hymns recited even today.

Similar mentions can be found in ancient Greek scriptures as well. Helios, the Sun God is believed to ride a chariot daily from the east to the west across the sky. Helios was considered the chief God. Apollo was actually a subordinate deity of radiant purity which was later interpreted equally to the Sun God.

On the other hand, the Mayans are known to be avid astronomers. They could record and interpret many events in the sky. They connected the visuals of the sky to the will and actions of the Gods. Their buildings are built with astronomy in mind. The Sun, moon, and planets were studied. The Sun was given prime importance and they worshipped it as Kinich Ahau.

In Chinese mythology, Xihe was the Sun God. Mythology says that it was one of the two wives of Di Jun, the other being Changxi. She was the mother of ten Suns, all three-legged crows perching on

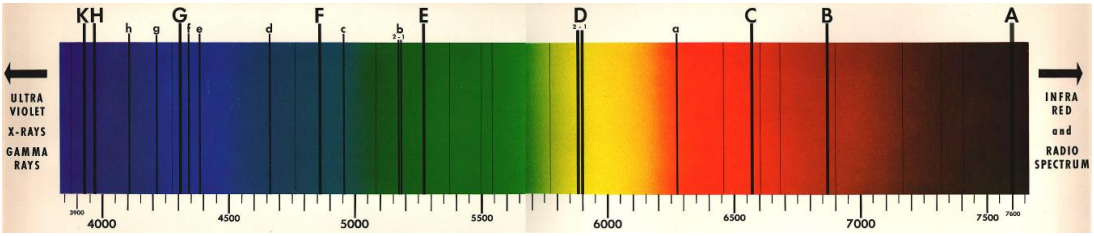

Figure 1.1: The Fraunhofer lines on the solar spectrum.

a mulberry tree! The Chinese were keen astronomers too. They recorded many important celestial events and were the first to observe the sunspots. Records dating back to 28 B.C. mentions the rising Sun having a coin-sized black vapour at its centre.

In the last few thousand years, humans learnt about the eclipses of the Sun depending on the motion of the moon. Rudimentary approaches were made for predicting eclipses. The absence of the Sun in broad daylight actually terrified humans through the ages. Those who could predict eclipses were considered powerful. Studying the Sun, its motion and its properties can be seen as a cumulative process in human history. The invention of a telescope greatly helped the study of the Sun. Galileo pointed his telescope at the Sun in 1609 which resulted in the scientific revolution. The Sun was no more seen as a mythical object but rather considered a physical object.

1.2 Historical Studies

Early Greek philosopher Aristarchus of Samos proposed the first heliocentric model where he put the Sun at the centre and the other planets around the Sun. However, in the later period, another Greek scholar Claudius Ptolemy proposed a geocentric model of the solar system in 150 A.D. The Sun, moon, and planets, were considered to revolve around the Earth. This model was considered up to the 16^{th} century until Nicolaus Copernicus, a Polish astronomer came up with a heliocentric model based on mathematical reasoning, the one which is followed today. Solar observations since then play a pivotal role in many major scientific studies carried out in modern days.

The advancement of the telescope led to several breakthroughs in science. Kepler's observations of the Sun and planets later on led to Newton's theory of Gravitation in 1687. Newton studied the properties of light by directing sunlight through a prism to discover its constituent colours. Further, Hyde Wollaston (1802) used sunlight through a narrow slit to discover dark absorption lines, which were wrongly interpreted as the borders between colours. In the 1800s, infrared and ultraviolet light was discovered. Spectroscopy was the new science that helped scientists to identify gases in the Sun's atmosphere. This led to the understanding of wavelengths of various radiations.

Fraunhofer in 1817, discovered hundreds of dark absorption lines in the solar spectrum (Figure 1.1). He made it clear that those lines were the inherent properties of the sunlight and had nothing to do with the Earth's atmosphere (although some lines arise due to the absorption by oxygen molecules in the Earth's atmosphere). The positions of these dark lines were equated with

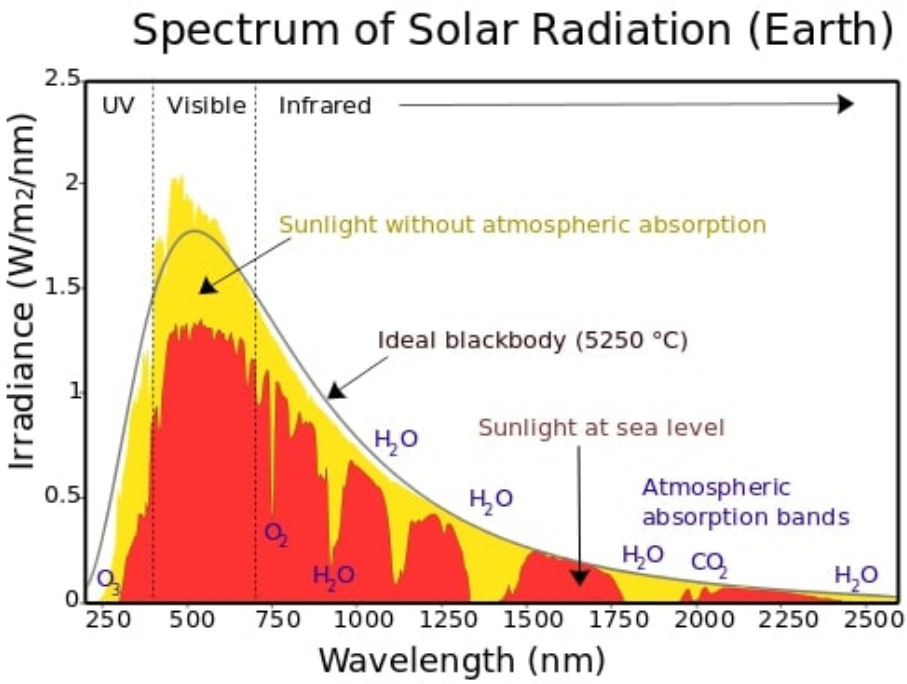

Figure 1.2: Planck's blackbody radiation curve.

similar bright lines observed in the Earth-based experiments. This led to the big step of inferring the chemical composition of the Sun. It was learnt that certain elements in the Sun were indeed present on the Earth as well.

However, despite all this progress, the energy generation in the Sun was still unknown. Various hypotheses like the Sun contracting to emit heat was put forward. English astronomer Joseph Norman Lockyer (1868) discovered helium by observing bright lines in the solar spectrum. French scientist Janson and Madras Observatory director Pogson also claimed to have discovered helium. Lockyer found that certain wavelengths present in the spectrum did not have a similar wavelength of any known element on the Earth. He proposed that this element was seen only in the Sun and named it helium. Thus, helium was discovered on the Sun 30 years before it was found on Earth. The scientific theories with models and hypotheses continued with the solar observations in later years. Kirchhoff's laws for radiation and Doppler shift in Fraunhofer lines at the solar limb are notable milestones in the history of solar studies.

The twentieth century was the time of discovery and understanding of the atomic structure that paved way for the development of quantum physics. Theories were developed to explain the observed Fraunhofer lines. The continuous solar spectrum was explained by Planck, and further by Einstein in 1905 by approximating the photosphere as a black body at a temperature of 5800 K (Figure 1.2). Solar irradiance spectrum above and at the surface can be seen in yellow and red curves respectively. The EUV and X-rays are produced on the lower side of the wavelength. However, they comprise small amounts of the Sun's total output power.

The Sun emits radiation in a wide range of wavelengths. The energy generated in its core is

mainly X-rays. Processes like internal absorption convert these high-energy photons into lower-energy photons by the time they reach the Sun's surface. Hence, the photosphere also emits gamma rays, ultraviolet, visible light, infrared, and radio waves.

Astronomers gradually worked towards understanding the energy generation in the Sun through nuclear fusion. It should be noted that the only direct evidence of the proposed nuclear processes in the core is the presence of neutrinos along with these radiations. Infrared telescopes were in use by the 1960s. So observations in wavelengths beyond the visible spectrum were being explored. Balloon experiments and observations through rockets from high altitudes above the Earth enabled studies without atmospheric interference.

Solrad 1 (1960), launched by the United States was the first spacecraft that was dedicated to solar studies. At the same time, NASA started off with the Pioneer series of satellites for observing the Sun which made immense progress over that decade.

Skylab was launched by NASA in 1973 and marked America's first experimental space station. This mission aimed at proving that working in space for longer periods was possible The mission expanded our knowledge of solar astronomy, especially in EUV. NASA launched its next mission Solar Maxima Mission to study the γ-rays, UV, and X-rays emitted during solar flares.

The SOlar and Heliospheric Observatory (SOHO) is the most extensive solar mission developed by ESA and NASA which was launched in 1995. It studies the solar interior, atmosphere and solar wind through twelve different payloads. The spacecraft still continues to operate. Voyagers 1 and 2 were later launched and aimed to discover the composition of the solar wind now traveling beyond the heliosphere. Table 1.1 list some of the major solar missions that have contributed immensely to our understanding of the Sun.

Helioseismology developed as a new field to study the solar interior. It considers the p-mode oscillations. Our present-day understanding of the solar interior is mostly based on helioseismic studies. In the last few decades, the role of solar observations has moved into new areas. The Sun is the only spatially resolvable star and solar observations give valuable inputs to modern-day astronomy.

1.3 Sun as a Star

The Sun is an ordinary star just like the 100 billion stars in the Milky Way. It was formed 4.5 billion years ago taking its shape from a molecular cloud composed of hydrogen and helium. A shock wave emitted by a nearby supernova energized this molecular cloud. As this molecular cloud started to compress, some of its gas collapsed due to gravitational pull. During this process, it began to rotate and heat up with increasing pressure. Gradually, the gas is heated up to a temperature high enough to begin nuclear fusion. The Sun was thus formed and the other parts of this molecular cloud cooled into a disc around the Sun and became the planets, asteroids, comets, and other bodies in our solar system.

Table 1.1: Major solar missions

No.	Spacecraft	Agency	Period	Topic of interest
1.	Pioneer series	NASA	1960—1969	Magnetic field, solar flare etc,.
2.	Skylab	NASA	1974—1979	Sun, comet, stellar and space physics.
3.	Helios A and B	NASA	1974—1985	Solar wind, magnetic and electric fields etc,.
4.	SMM	NASA	1980—1989	Sunspot cycle, sun-grazing comets.
5.	Yohkoh	JAXA	1991—2001	X-ray and spectroscopy of flares, magnetic reconnection.
6.	Ulysses	NASA, ESA	1995—2008	Solar poles' observations.
7.	SOHO	ESA, NASA	1996—2020	Sun's core, corona, solar wind etc,.
8.	TRACE	NASA	1998 to 2010	Solar atmosphere.
9.	Hinode	JAXA, NASA, PPARC	2006 onwards	Solar corona
10.	SDO	NASA	2010 onwards	Solar magnetic field structure, EUV emissions etc,.
11.	IRIS	NASA	2013 onwards	Lower solar atmosphere.
12.	Solar Orbiter	ESA	2020 onwards	Solar wind, polar regions etc,.
13.	PSP	NASA	2021 onwards	Solar coronal mysteries.
14.	Aditya-L1	ISRO	Will be launched soon	Solar atmosphere.

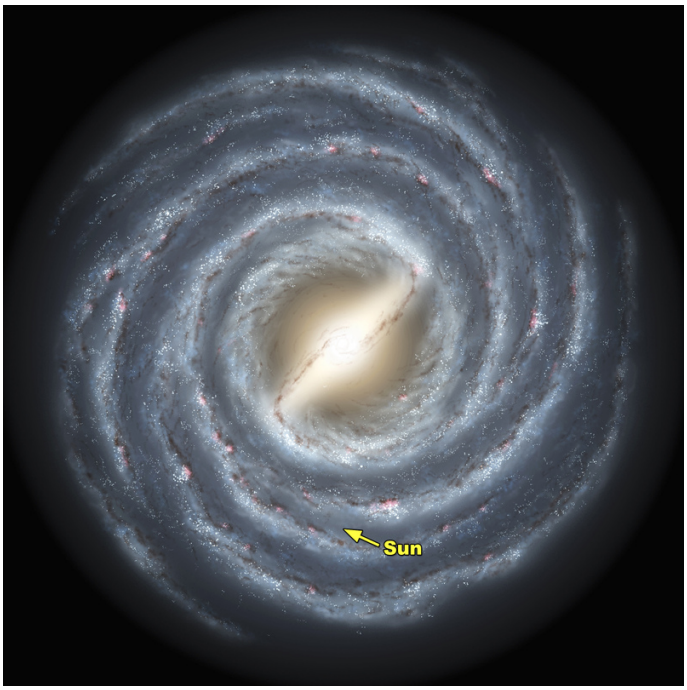

Figure 1.3: Figure showing the position of the Sun in our galaxy, the Milky Way.

The Sun is at a distance of about 150 Mkm from the Earth. This distance is known as the astronomical unit (AU) and is used as a standard measure of distance in astronomy. In other words, an AU is the time it takes for a photon to travel from the Sun to the Earth and this time is about eight minutes and 19 seconds. The radius of the Sun is about 7×10^5 km, which is about 109 times the size of the Earth's radius. The Sun contributes to about 99.8 % of all of the mass in the entire solar system!

The solar composition is a combination of gases in the form of plasma, which is a state of matter with most of the particles in an ionized state. About 75 % of the Sun is hydrogen which keeps constantly fusing to create helium through nuclear fusion (section 1.8). Helium constitutes the remaining portion of the Sun's composition. A small percentage, 1.69 % of the Sun's mass is composed of other gases and metals like iron, nickel, oxygen, silicon, sulfur, magnesium, carbon, neon, calcium, and chromium.

So, the Sun is not a solid mass and it does not have any identifiable boundaries between its layers. The Sun is permeated by a huge network of the magnetic field. The Sun rotates counterclockwise and takes around 25—35 days to complete one rotation. The Sun orbits around the centre of the Milky Way clockwise. This orbit is about 24,000—26,000 light-years away from the galactic centre. The Sun takes about 225—250 million years to complete one orbit around the galactic centre! The position of the Sun in the Milky Way can be seen in Figure 1.3.

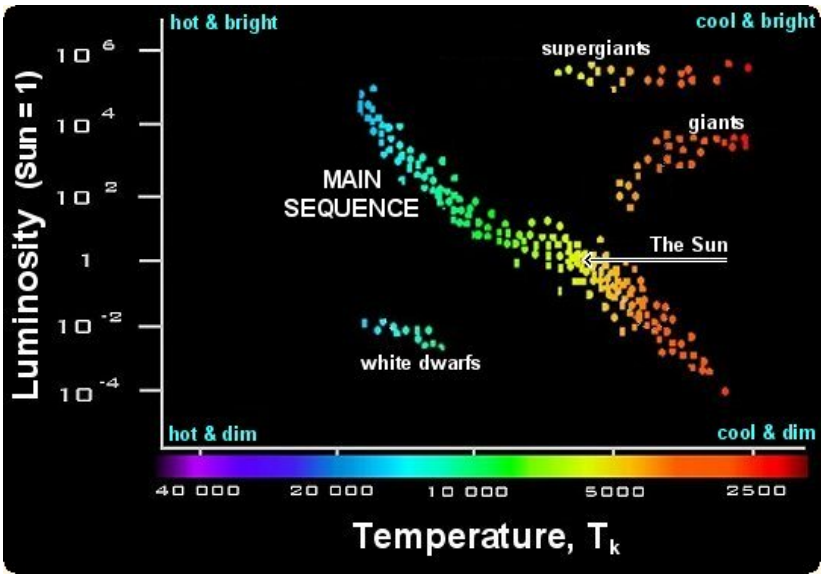

Figure 1.4: The Hertzsprung–Russell diagram. The Sun is in the main sequence.

1.3.1 Future of the Sun

The Sun cannot go on forever. Nuclear fusion will stop once the Sun runs out of hydrogen. Every second, the Sun loses around 620 million metric tons of hydrogen generating helium. Currently, its core is about 74 % hydrogen. Over the next five billion years, the Sun will burn up most of its hydrogen, and helium will become its major source of fuel. During this period, the Sun will go from "yellow dwarf" to "red giant". When most of the hydrogen in the core ceases, the core will contract and heat up. This will increase the amount of nuclear fusion. The outer layers of the Sun will start expanding to about 200 times its current radius at this stage. When the Sun expands, it will spread its energy over a large surface area leading to an overall cooling effect on itself which makes the Sun appear reddish. In this phase, the Sun's core reaches 100 MK which is sufficient for carbon and other heavier elements' formation through nuclear fusion. This would cause an intense solar wind which will throw off the outer layers. The red giant phase would deplete by then. The Sun would be left with a carbon core now and it becomes a white dwarf. The Sun cannot generate or emit energy any further.

The Hertzsprung-Russell diagram which is considered one of the basic tools in studying stellar evolution, plots the temperature of stars against their luminosity. Depending on the initial mass, every star goes through specific evolutionary stages which are governed by its internal structure. This decides how it produces energy. Each of these stages corresponds to a change in the temperature and hence luminosity of the star. The position of the Sun which is currently in the main sequence is shown in the HR diagram in Figure 1.4.

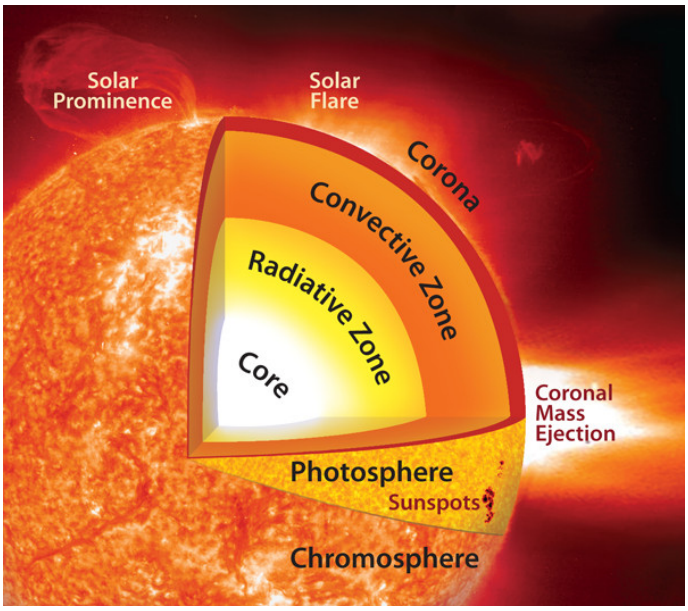

Figure 1.5: Structure of the Sun.

1.4 Structure of the Sun

The solar structure is made up of the interior, surface and outer atmosphere. The details can be seen in Figure 1.5. Each of these layers has its own characteristics when it comes to temperature, functioning and the features that appear on them.

1.4.1 Solar Interior

The solar interior is separated into three different regions described as below.

Core: The core extends to about 0.25 $R_\odot$. The temperature here exceeds 15 MK and is the only region where nuclear fusion takes place. Hydrogen atoms collide and fuse to create helium atoms. There are two types of fusion reactions that occur, namely the proton-proton chain reaction and the carbon-nitrogen-oxygen chain reaction (section 1.8). These processes emit enormous amounts of energy. During these two reactions, two types of particles are released: photons and neutrinos. These particles carry and emit the light, heat, and energy from the Sun.

The radiative zone: The radiative zone of the Sun starts at about 0.25 $R_\odot$ and extends to about 0.7 $R_\odot$. In this region, heat generated at the core cools dramatically and the temperature falls to around 7-2 MK. The energy transfer in this region is by the process of thermal radiation. During this process, photons released in the core travel a short distance and are then absorbed by a nearby ion, released by that ion, and later absorbed again by another.

Tachocline: There exists a transition zone between the radiative zone and the convective zone which is called the tachocline. This region is created as a result of the Sun's differential rotation. Differential rotation happens when different parts of an object rotate at different velocities. The Sun's equator happens to rotate much faster than its poles. Also, the rotation rate of the Sun

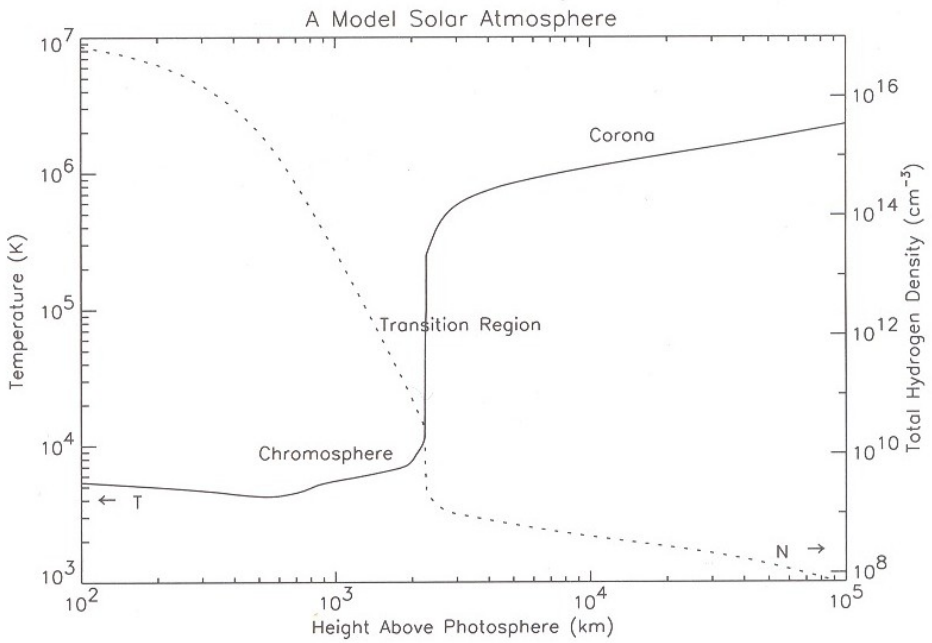

Figure 1.6: Variation of temperature and density with height above the photosphere.

changes rapidly in the tachocline.

Convective Zone: At around 0.7 $R_\odot$, the convective zone begins. In this region, the Sun's temperature is not hot enough to transfer energy by thermal radiation. Instead, it transfers heat by convection through thermal columns. When these gases reach the top of the convection zone, they cool down further and plunge back.

1.4.2 Solar Surface

Photosphere: The photosphere is the visible surface of the Sun. The photons generated in the core can finally escape into the space after a million-year journey. The temperature of the photosphere is around 5,800 K. The layer is much cooler than the Sun's core and in fact cooler than all other layers. Of course, there is variation in temperature from place to place in the photosphere or even other layers for that matter, as the Sun is not a uniform body.

The photosphere is bright yellow and visible. Its thickness is about 500 km. Telescopes with high-resolution power can differentiate the tops of the thermal columns which appear as granules across the photosphere. Every granule has a bright centre which is the hot gas rising through a thermal column. The edges of the granules are made of cooler gas descending back down. Hence these edges appear darker. The size of a granule is about 1,000 km and its lifetime is about 8—20 minutes. There are also supergranules of the size of about 30,000 km which last for up to a day.

1.4.3 Solar Atmosphere

The solar atmosphere is the hottest region of the Sun after its core. It is made up of the chromosphere, transition region and the corona. The solar atmosphere is less dense and hence it is obscured by the brightness of the photosphere.

Chromosphere: This region appears pinkish-red during solar eclipses. Hence the name chromosphere (derived from the Greek word for colour, chroma). This layer is about 2,000 km thick. At the bottom of the chromosphere, where it meets the photosphere, the Sun is at its coolest, at about 4,400 K. This low temperature gives the chromosphere its pink colour. The temperature in the chromosphere increases with altitude and reaches 25,000 K at the outer edge of the region.

Transition Region: The solar transition region is a small layer that separates the chromosphere from the corona. Below the transition region, the layers of the Sun are controlled mainly by the gas pressure. The plasma beta, which is the ratio of gas pressure to the magnetic pressure, is < 1 in this region. The temperature increases to almost 1 MK. Figure 1.6 shows this drastic increase in the temperature.

Corona: The corona is the outermost region of the solar atmosphere. It extends to millions of kilometres above the photosphere and gradually transforms into the solar wind that flows outward through our solar system. The material in the corona is extremely hot and tenuous. Figure 1.6 also shows the fall of density in the solar atmosphere. The average temperature in the corona is 2 MK with the temperature going up to 10 MK in certain regions. During a total solar eclipse, the wispy corona can be seen briefly when the moon blocks out the solar surface (Figure 1.7). A special instrument called a coronagraph allows astronomers to view the corona at other times.

There are three main components of coronal light which are distinguished on the basis of the mechanisms that produce the coronal light. They are the K (Kontinuierlich), F (Fraunhofer) and E (Emission) corona.

K-corona: This displays a continuous emission spectrum and is strongly ionized. This corona extends between $1.03\ R_\odot < R < 2.5\ R_\odot$. This arises when the photospheric light is scattered by the electrons of the coronal gas.

F-corona: This corona stretches upto $R > 2.5\ R_\odot$. This light arises due to the scattering of the photospheric light by the dust particles in the ecliptic plane. This shows dark absorption lines that Fraunhofer had observed in the on-disc spectrum. The dust particles have their own velocities which result in the Doppler shifts of these dark absorption lines.

E-corona: The E-corona represents the light from ions in the coronal plasma that absorbs light from the photosphere and re-emits them through specific electronic transitions. This gives rise to the emission spectrum. This is the only true light of the corona. Each ion emits a unique pattern of spectral lines, which can be used to find the composition, temperature of a particular ion species, velocities of the structures and the density. With suitable instruments, they can even be used to measure the strength of the magnetic field through which they move. The E-corona extends about 700,000 km above the photosphere.

Figure 1.7: Solar corona captured during the total solar eclipse of the 21 August 2017 at Wyoming, USA.

1.5 Important Solar Features

The Sun has numerous features many of which some are specific to particular layers and some are interconnected through the layers. An understanding of these features not only gives us an insight into these layers but also contributes to the functioning of the Sun.

1.5.1 Sunspots

Sunspots are features specific to the photosphere. They are dark and can be as big as a planet. Their darkness is due to their low temperatures compared to the hotter surrounding regions. A large sunspot can have a central temperature of the order of 4,000 K. This is much lower than the 5,800 K surface temperature of the photosphere. Their darkness is only in contrast to the bright surroundings of the Sun. Sunspots have two regions, the central dark umbra and the outer lighter penumbra (Figure 1.8). Just like the Sun, other stars also have spots. Larger starspots and magnetic cycles have been found on a few other stars.

Sunspots arise due to disturbances in the solar magnetic fields which rise up to the photosphere from the lower layers. The powerful magnetic fields around these areas produce active regions on the Sun. These regions frequently release magnetic disturbances in the form of solar flares and coronal mass ejections which are known to have serious impacts on the Earth's atmosphere. Space weather forecasters track these features in order to predict solar outbursts.

1.5.2 Solar Prominences

Solar prominences are bright plasma loops that are anchored into the photosphere. They are curved and twisted in structure due to the underlying magnetic flux ropes. A prominence is known to erupt

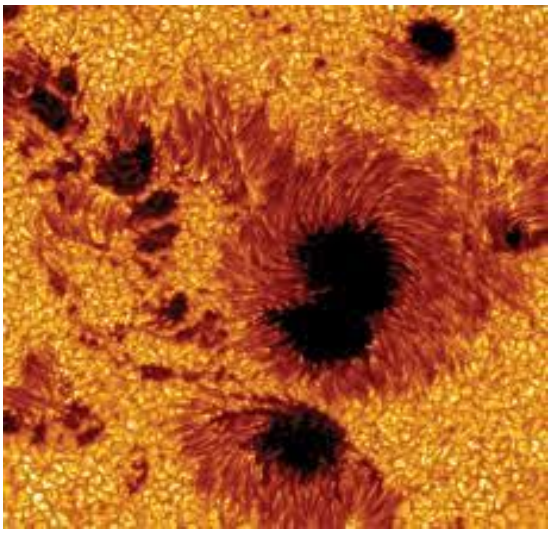

Figure 1.8: Sunspots with umbra and penumbra seen in an active region. Image credit: NASA.

when the structure becomes unstable due to magnetic instability. They burst far into the corona and further expand into the interplanetary space with speeds of hundreds of kms^{-1}. These structures have sizes of hundreds of thousands of kilometres. Their lifetime lasts anywhere between days to months. Prominences are cooler in temperature compared to the corona. Hence, they appear as dark filaments against the bright photospheric backdrop.

1.5.3 Active Regions

Active regions, as the name suggests are highly active (magnetically) areas on the Sun. They are formed by the solar dynamo, located deep in the solar interior and are seen as magnetic flux loops in the shape of ω. Active regions emit radiations in various wavelengths and hence their appearance depends greatly on the imaging wavelength and the observational angle. When an active region is observed against the dark sky at the limb (edge of the Sun), the magnetic field of an active region can be traced by glowing arches of gas confined within coronal loops (Figure 1.9). When it is projected against the solar disk, its appearance is much different. When we observe it in H_α wavelength with a low telescopic resolution, we can see bright solar chromospheric plages (Figure 1.10). At higher resolution, the relatively cool chromospheric loops of the active region can also be seen. In X-rays wavelengths, the hotter coronal loops of the active region can be seen.

1.5.4 Quiet Sun

The quiet Sun are regions on the solar surface that are devoid of sunspots and active regions. Earlier it was thought that these regions are non-magnetic as one could observe only the photospheric granulations in the continuum images. However, images taken in polarized light showed a magnetic network with small-scale flux concentrations. Quiet Sun fields are intimately connected to supergranulation patterns.

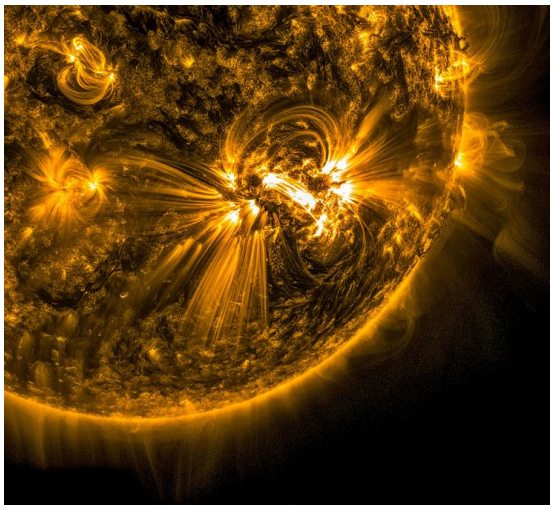

Figure 1.9: Coronal loops coming out of the active region AR2192.

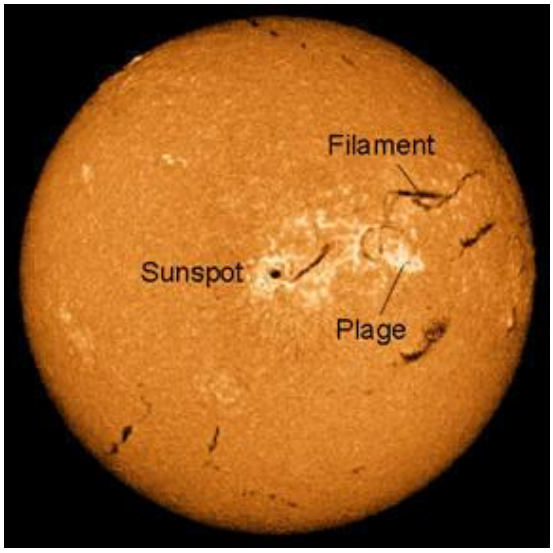

Figure 1.10: A bright sunspot with a nearby plage and filament.

1.5.5 Solar Flares

Solar flares are an important eruptive characteristic feature of the solar corona. They are huge explosions from the Sun. They are found to be sudden and intense outbursts that brighten up the surrounding. They typically last for several minutes. Flares result due to the entanglement of intense magnetic fields on the Sun. The simplest way to understand these explosions is to think of them as a rubber band that snaps when twisted way too much. Likewise, the tangled magnetic fields release energy when they snap after intense twisting. Solar flares are found to emit in various wavelengths, like X-rays, ultraviolet, visible light, and radio waves. Although solar flares are visible in white light, they are often noticed to emit more in X-ray and ultraviolet. Coronal mass ejections, which are much more intense and explosive events are often associated with solar flares. As sunspot and active region activities are higher during solar maxima, one can expect more flares during solar maxima.

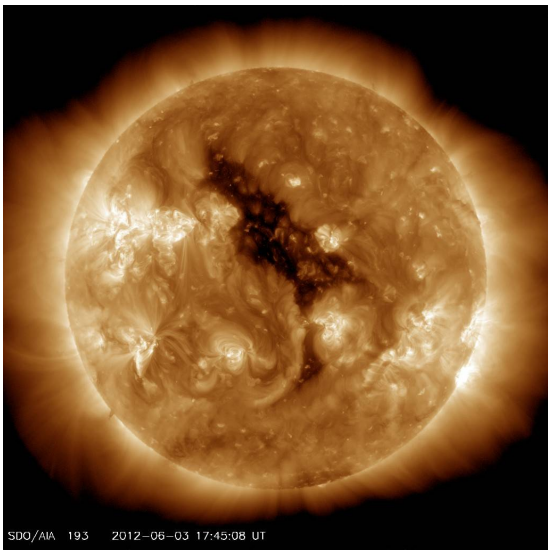

Figure 1.11: A coronal hole captured by SDO.

1.5.6 Spicules

Spicules are jets of dense gas ejected from the solar chromosphere. They are found to occur at the edges of the chromospheric network at regions with strong magnetic fields. These jets can extend up to 10,000 km before falling back to the Sun. These features are learnt to contribute to the coronal heating phenomena and the solar wind by feeding material into the corona.

Observations have shown that about 1,00,000 spicules are active on the Sun's surface at any given time. They are understood to arise from the lower chromospheric regions with speeds of the order of 20 kms^{-1} throwing material to a height of several thousand kilometres which disperse and collapse within 10—15 min.

1.5.7 Coronal Holes

Coronal holes (Figure 1.11) are regions that are relatively cooler with less dense plasma formed in the solar corona. Here the Sun's magnetic field extends into interplanetary space as open fields. Open fields associated with coronal holes aid the solar wind to escape thereby decreasing the coronal temperature and density. Although these structures can develop at any time and location on the corona, the coronal holes at the solar poles are most stable during the solar minima.

The bright areas in the coronal holes are made of hot and dense gas captured by the magnetic fields. The dark regions where the magnetic field escapes into the interplanetary space make these regions appear like holes. They are mostly observed in UV.

When a coronal hole is positioned on the Earth-facing side of the solar disk, the hot gases flow towards the Earth. When these gases with charged particles interact with the Earth's magnetic field, they give rise to geomagnetic disturbances on the Earth resulting in enhanced auroral activity.

1.5.8 Coronal Streamers

Coronal or helmet streamers are elongated cusp-like structures that appear in the solar corona. They are often visible in white-light coronagraphs during solar eclipses. They are closed magnetic loops that lie in between regions of opposite magnetic polarity on the photosphere. The high-speed solar wind elongates these loops to have pointed tips which can extend more than 1 $R_\odot$ into the corona. It is observed that during solar minima, these streamers are found closer to the heliographic equator and during solar maxima, they are found to be more symmetrically distributed around the Sun.

1.5.9 Solar Wind

The solar wind is a stream of extremely hot, charged particles thrown out from the outer atmosphere of the Sun. This is one of the mechanisms through which the Sun loses its mass and so far, at the given rate, the Sun has only lost about 0.01 % of its total mass due to solar wind. The solar wind blows out in all directions. It also has charged particles which can get released into the Earth's magnetic field, particularly at the poles. This interaction causes auroras at the northern and southern poles. Solar wind can also cause solar storms which are hazardous when they interfere with satellites (section 1.6).

The solar wind fills the heliosphere like a massive bubble of charged particles that encompasses the solar system. Its speed eventually slows down near the edge of the heliosphere, a theoretical boundary called the heliopause. This boundary separates our solar system from the interstellar medium. The solar wind travels billions of kilometres before ceasing at the heliopause.

1.5.10 Coronal Mass Ejections

A Coronal Mass Ejection (CME) (Figure 1.12) is a massive explosive outburst of the solar wind plasma from the solar corona. These outbursts carry billions of tons of material into space at speeds of the order of hundreds of kilometres per second. A CME contains particle radiation and magnetic fields. Like any other eruptive event, these blasts originate in magnetically active regions. CMEs are often found to appear along with solar flares giving rise to solar storms. The exact relationship between flares and CMEs needs a better understanding. Some studies have shown flares to trigger CMEs, but sometimes CMEs are observed without any flares. More CMEs are formed during solar maxima.

1.6 Impacts of Flares, CMEs and Solar Wind on the Earth

The Sun releases enormous amounts of particles and radiations through various eruptive events. The high energy particles and radiation are dangerous to life. Even though the surface of the Earth is protected to some extent, solar flares and CMEs still affect the Earth's magnetic field and atmosphere.

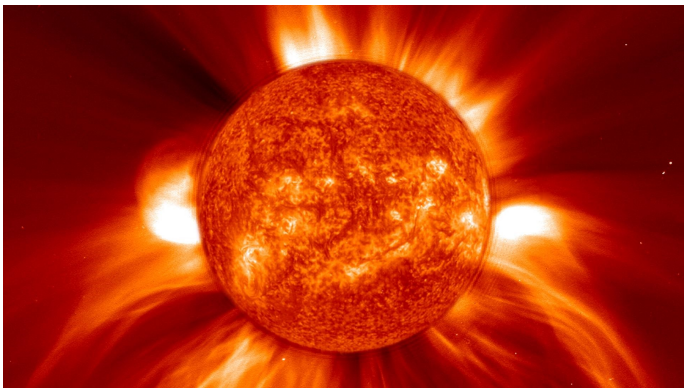

Figure 1.12: A coronal mass ejection captured by the SOHO.

The emissions that are primarily made of high-energy protons and X-rays are indeed dangerous. The following are some of the major hazards posed by flares, CMEs and solar wind on the Earth.

- Flares and CMEs are effective despite the Earth's magnetosphere and can cause geomagnetic storms.
- CMEs drive shock waves which can continuously produce energetic particles as they propagate through the interplanetary space.
- The energetic ultraviolet radiation heats the Earth's outer atmosphere, causing it to expand. This process increases the drag on the Earth-orbiting satellites resulting in the reduction of their lifetimes in their orbits.
- The intense radio emissions from flares and CMEs can degrade satellite communications.
- Can cause temporary loss of electrical power.
- Astronauts in space are also exposed to cumulative radiation which can be dangerous.
- The damage to satellites and power grids can be very expensive and disruptive.
- Geomagnetic storms are more disruptive now than in the past due to our greater dependence on technology.

1.7 Solar Activity

1.7.1 Sunspot Cycle

Sunspots are not just mere features that appear and fade away like other one-time explosive events. These features keep on appearing, changing their size and numbers in a cyclical manner. The length of this cycle is roughly eleven years on average. This cyclical variation in sunspot counts was discovered

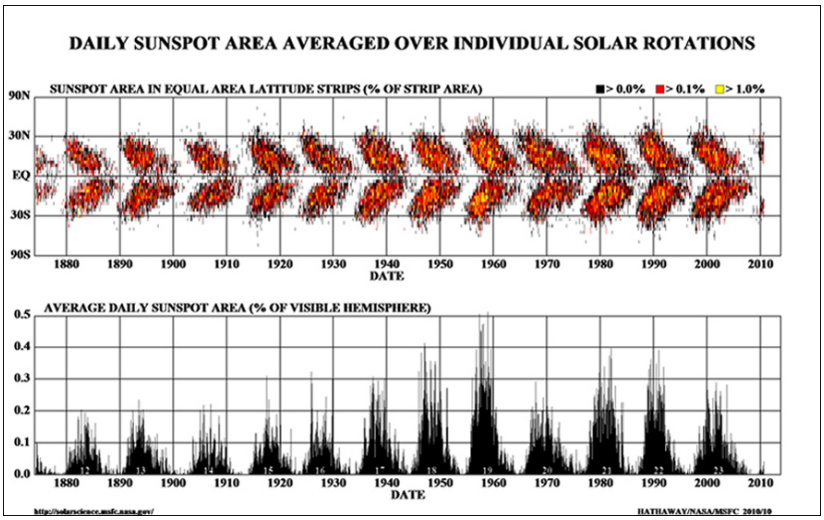

Figure 1.13: Top: Butterfly diagram. It shows the movement of sunspots from higher latitudes to lower latitudes over a period of time. Bottom: It shows the corresponding solar cycles.

in 1843 by the German amateur astronomer Samuel Heinrich Schwabe and is known as the sunspot cycle. We are currently in the sunspot cycle 25 which started around May 2020.

Detailed observations of sunspots are available for centuries and it shows that sunspots do not appear randomly at random places. They are found to appear in between $\pm 35^\circ$ solar latitude. They have a magnetic polarity associated with them and each of them has an opposite polarity corresponding to them in the opposite hemisphere (Hale's polarity). Sunspots in the higher latitudes migrate towards the equator as the cycle progresses. Around $\pm 20^\circ$ solar latitude, they reach the solar maxima. By the time they reach the equator, they are back to minima and during this time, new sunspots begin to form at the higher latitudes and the cycle repeats. It is found that the polarity of the sunspots changes every 11-year cycle. Besides this, the sunspots are tilted at an angle that increases with the latitude (Joy's law). Figure 1.13 known as the butterfly diagram highlights the number and positions of the sunspots for sunspots observations since May 1874. The differential rotation of the Sun was indeed observed due to the presence of sunspots.

Sunspots indicate disturbances in the solar magnetic field which can generate eruptive events. The Sun is active when the sunspot counts are high. So sunspots are basically the root cause of the bigger eruptive events observed in the solar atmosphere. Sunspot numbers are available since the 1700s much before solar activities were observed. Hence, these records serve as a valuable indicator of solar activity for long term. These records also indicate periods of unusually low sunspot counts during 1645—1715 when only a few sunspots or none were noted. This period is called the Maunder minimum and it corresponds to an extremely cold period (little ice age) in Europe. The origin and cyclic behaviour of stellar magnetic fields are topics of great interest.

1.7.2 Solar Dynamo

The Sun is a huge magnet having a very strong magnetic field. This magnetic field is generated in the tachocline region. The radiative zone has a uniform rotation and the convective zone has a differential rotation. A sharp change occurs in this transition region that results in a large shear. Magnetic flux tubes can become buoyant and rise through the convection zone. They become evident in the photosphere in the active regions leading to the formation of sunspots. One can see this in the form of a leading sunspot and the other sunspots or groups of sunspots with opposite magnetic polarity follow this. The differential rotation on the solar surface twists the surface magnetic field. This process rises up to the poles through meridional circulation and re-orients the toroidal component of the magnetic field. The toroidal component which is initially oriented in the east-west direction during the solar maximum now re-orients into a poloidal field and connects the North and South pole magnetic fields during the solar minimum. This orientation and re-orientation of the magnetic fields can be seen in Figure 1.14. This process actually changes the direction of the magnetic field of the Sun every 11 years and is called the solar dynamo. So, the initial magnetic configuration is attained after 22 years roughly and this cycle is known as the solar magnetic cycle. During the maximum of the solar cycle, there is a peak in solar activity which can be inferred from the higher number of sunspots and the occurrence of larger eruptive events like flares and CMEs.

1.8 Energy Production in the Sun

The Sun emits an energy of 4×10^{26} Js^{-1}. Its mass 2×10^{30} kg corresponds to 2×10^{-4} Jkg^{-1}s. With this rate of energy generation, the Sun is burning for 4×10^{9} yrs. Chemical reactions or gravitational energy cannot generate this huge energy. Hence, nuclear energy is the only possible source. The energy release in the conversion of hydrogen to helium will be,

$$\begin{aligned} E &= 4M_H - M_{He} \\ &= 4 \times 1.007825 - 4.002603 \\ &= 0.028697 \text{ u} \\ &= 26.73 \text{ MeV} \\ &= 4.28 \times 10^{-12} \text{ J}. \end{aligned}$$

In this fashion, 1 kg of hydrogen which contains about 6×10^{26} protons can generate 2.4×10^{15} J kg^{-1} amount of energy at the rate of 2×10^{-4} J kg^{-1}s for 10^{12} yrs. Hence, a series of nuclear reactions fusing four hydrogen nuclei to produce one helium nucleus could be adequate. This idea was proposed by R. Atkinson and F. Houtermans in 1928 and was proven much later.

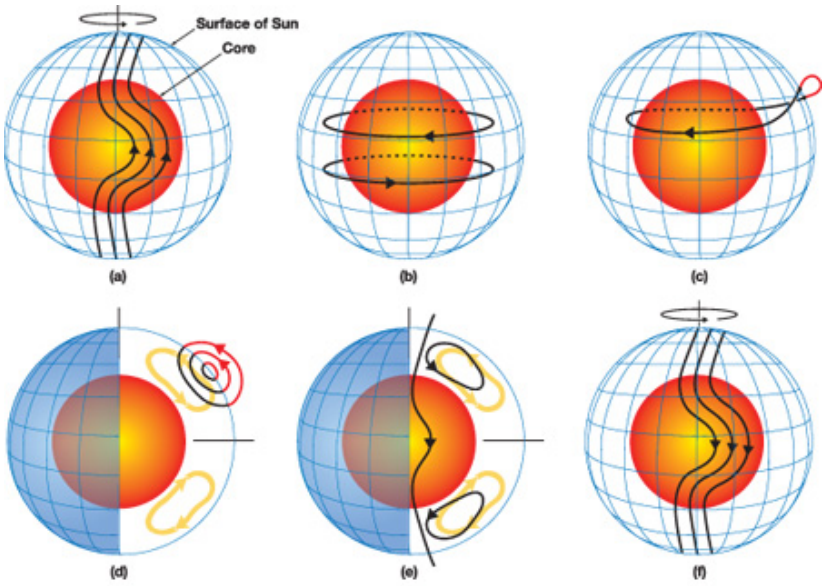

Figure 1.14: Illustration showing how magnetic fields are recycled to produce sunspots within the solar convection zone (the top 30 % of the solar interior, shown in white, surrounding the radiative core, in orange). As the sun rotates faster at the equator than the poles, the north-south (poloidal) magnetic field (a) gets twisted into an east-west (toroidal) field (b) Regions of enhanced toroidal field become buoyant and rise to the surface. These field lines get twisted in the process due to the rotation of the Sun and emerge as sunspots on the photosphere (c. upper right). Panels (d) and (e) show the solar dynamo, the meridional circulation of the plasma (shown in yellow) carries the surface magnetic flux toward the poles. This process reverses the direction of the polar field which eventually moves back toward the equator. The new sunspots that are formed now from the poloidal field (f), will have opposite polarity to those in (a). Figure courtesy: M. Dikpati.

1.8.1 p-p Chain

For an average-sized star like the Sun, this type of nuclear reaction satisfactorily explains its energy generation and can be seen in the following steps.

The p-p chain is as follows:

$$^1H_1 +^1 H_1 \longrightarrow^2 H_1 + e^+ + \nu \tag{1.1}$$

$$^2H_1 +^1 H_1 \longrightarrow^3 He_2 + \gamma \tag{1.2}$$

$$^3He_2 +^3 He_2 \longrightarrow^4 He_2 + 2^1H_1 \tag{1.3}$$

Proton–proton fusion can occur only if the kinetic energy of the hydrogen atoms is sufficient enough to overcome their mutual electrostatic repulsion. The deuteron-producing events are rare. Diprotons are the much more common result of the proton–proton chain. However, these diprotons almost immediately decay back into two protons. Hence the conversion of hydrogen to helium happens to be slow. The complete conversion of hydrogen into helium is calculated to take more

than ten billion years.

The proton–proton chain is a decaying series of reactions. The product of one reaction provides the material for the next reaction. The neutrinos produced during this process escape and an energy of 24.3 MeV is generated with the generation of each helium nucleus. This process depletes the protons gradually and builds up the helium concentration. The mean time for one p-p reaction is quite long.

1.8.2 C-N-O Cycle

The CNO cycle, suggested by theoretical models dominates in stars with masses greater than 1.3 $M_\odot$. Stars bigger than the Sun require different cycles to explain their energy production with the formation of elements heavier than helium. This cycle is alternatively known as Bethe–Weizsäcker cycle, named after Hans Albrecht Bethe and Carl Friedrich von Weizsäcker who proposed it in 1939.

Unlike the p-p chain, which consumes all its constituents, the CNO cycle is a catalytic cycle. Here, four protons fuse using carbon, nitrogen, and oxygen isotopes as catalysts, and each of these is consumed in steps of the CNO cycle but re-generated in a later step. The end product is one stable helium nucleus, two positrons, and two electron neutrinos as can be seen in the following equations.

$$4^1H_1 + 2e^- \longrightarrow 4^1H_1 + 2e^- \tag{1.4}$$

$$\longrightarrow {}^4He_2 + 2\nu + 7\gamma + 26.7 \text{ MeV} \tag{1.5}$$

The positrons that are generated will instantly annihilate with the electrons by releasing energy in the form of gamma rays. The neutrinos escape by carrying away some energy. One nucleus generated here goes on to become carbon, nitrogen, and oxygen isotopes through a number of transformations in an endless loop.

The fusion of four protons to produce one He^4 nucleus should not destroy the C^{12} atom during the cycle as it acts as a catalyst. Some energy is carried away by the neutrinos that escape. For stars with masses of the range 0.4—2.5 $M_\odot$, the main part of the energy production is due to the C-N-O cycle rather than the p-p cycle. For less massive stars, the situation is reversed. According to the astronomical data, stars of 0.4 or lower $M_\odot$, form the bulk of the stellar population in our galaxy. So C-N-O cycle mostly occurs in very bright stars and majority of the stars drive their energy from the p-p cycle.

1.8.3 Radiation Output

The Sun which appears yellowish-white infers that it contains all the colours in the visible spectrum. The majority of the electromagnetic radiation from the Sun we receive is invisible to us. The most high-frequency waves emitted by the Sun are γ-rays, X-rays, and UV rays. The harmful UV rays are almost completely absorbed by the ozone layer. Ultraviolet C ranges from 100 to 280 nm. These

are radiations at a higher frequency. Due to the absorption by the atmosphere, very little of these reaches the Earth's surface. Ultraviolet B ranges from 280 to 315 nm. It is greatly absorbed by the Earth's atmosphere and aids in photochemical reactions leading to the production of the ozone layer. Ultraviolet A spans from 315 to 400 nm. This band also categorises to be harmful to humans.

IR rays that are emitted are at a much lower frequency band. It should be noted that most of the heat we receive is from IR.

1.9 Some Important Problems in Coronal Physics

1.9.1 Coronal Heating

Kepler was the first astronomer with a scientific approach who mentioned the appearance of the corona. Observations of the solar corona were made by Halley during the solar eclipse of 1715. But Bailey's report caught scientific attention in 1842. In the later years, Grotrian attributed the coronal red line Fe X in 1939 and Edlen identified 19 of the 27 known coronal emission lines as forbidden transitions in 1942.

The rise in the temperature above the photosphere and in the solar atmosphere can be seen in Figure 1.6. This figure also explains the drop in the density across these layers. The solar coronal density is of the order of 10^8 cm^{-3}, which is much lower than the photospheric density (10^{15} cm^{-3}). The existence of the corona was known through solar eclipses long before its physical details came to light in the 1940s. Since then, many studies have been dedicated to explaining it.

Also, according to the second law of thermodynamics, a body at a lower temperature cannot heat another body to a higher temperature. Hence, it requires complex mechanisms for the corona to attain a million-degree temperature.

Since 1970 onwards, with the launch of numerous high-altitude and space-based instruments, the solar coronal details came to be known. The structure, various features, the role of the magnetic field in defining these features, the mass and energy flow in the chromosphere and corona, and the source regions of solar wind all were important revelations. It is not just that the corona is heated to a high temperature, but at the same time, the corona loses a lot of energy through various processes. This actually facilitates in balancing the dynamic corona to some extent. The various energy losses are described by Withbroe and Noyes 1977 which is given in Table 1.2.

To explain the coronal heating mechanisms, one must identify the correct energy source. The mechanical motions that occur below the photosphere seem to play an important role. The coronal heating models are generally classified into two groups.

- **Alternating Current (AC) heating:** If the magnetic field changes in the coronal loops are faster than the Alfvén wave dissipation time, the process is referred to as AC heating.
- **Direct Current (DC) heating:** If the magnetic field changes in the coronal loops are slower than the Alfvén wave dissipation time, the process is referred to as DC heating.

Table 1.2: Coronal energy loss

Parameter	Quiet Sun	Coronal hole	Active region
Coronal temperature (K, at r $\approx$ 1.1 $R_\odot$)	1.1–1.6 $\times 10^6$	10^6	2.5 $\times 10^6$
Coronal energy losses (erg cm^{-2} sec^{-1})			
Conduction flux F_c	2×10^5	6×10^4	10^5–10^7
Radiative flux F_r	10^5	10^4	5×10^6
Solar wind flux F_w	$\lesssim 5 \times 10^4$	7×10^5	$< 10^5$
Total corona loss $F_c + F_r + F_w$	3×10^5	8×10^5	10^7
Solar wind mass loss (g cm^{-2} sec^{-1})	$\lesssim 2 \times 10^{-11}$	2×10^{-10}	$< 4 \times 10^{-11}$

AC heating: In AC heating models, energy is provided by the dissipation of waves in the corona. In general, turbulent convective motions on the solar surface generate three different types of waves propagating upwards in the solar atmosphere. These waves are:

1. **Alfvén waves:** Alfvèn waves are the oscillations of the magnetic field in the plasma. The motion of the ions and the perturbation of the magnetic field are transverse to the direction of propagation. Fast and slow magneto-acoustic waves can also travel across the magnetic field.

2. **Fast magneto-acoustic waves:** The fast magneto-acoustic wave is driven by a combination of the pressure from the magnetic field and the internal pressure of the plasma itself, with both these acting in phase. A fast wave can propagate in any direction in the plasma.

3. **Slow magneto-acoustic waves:** The slow magneto-acoustic wave is also driven by magnetic and internal pressure. But in this case, they act out of phase. The slow wave propagates most of its energy only along the magnetic field lines and struggles to propagate perpendicular to the magnetic field.

DC heating: The foot-points of the coronal magnetic fields are constantly shuffled by the photospheric convective motions which have random walk characteristics. The high electrical conductivity of the corona causes the magnetic field lines to freeze into the plasma. The magnetic field lines then get twisted leading to the current sheets. This leads to reconnection, thereby releasing the magnetic energy and heating the corona.

Impulsive nanoflare heating is considered as the third source of coronal heating by some physicists. Magnetic connection occurs when the opposite polarities come together and the magnetic energy is converted into heat and kinetic energy. This process produces events such as nanoflares, similar to flares and CMEs. These low-energy flares are more prevalent than larger flares in the corona contributing to the coronal heating.

1.9.2 Acceleration of the Solar Wind

Eugene Parker was the first person to propose the existence of solar wind (Parker 1958). According to him, solar wind is a consequence of a million-degree solar corona. As the temperature of the corona is so high, the Sun's gravity cannot hold it back. The solar wind streams off the solar atmosphere at speeds of about 400 km s^{-1} in all directions. However, the details about how and where the coronal gases are accelerated to high velocities are not understood.

The composition of the solar wind depends on the region from which it originates, that is the solar atmosphere which is made up of low-density plasma. It mainly comprises of protons, electrons and alpha particles with some small percentage of heavy ions of C, N, O, Ne, Mg, Si, S, and Fe. As it traverses through the interplanetary plasma, it picks up materials from space as well. The solar wind is not uniform and is always directed away from the Sun. There are two kinds of solar wind. The fast solar wind with speeds around 800 km s^{-1} is found to originate from the solar coronal holes. Slow solar wind with a speed of the order of 400 km s^{-1} arises from closed field regions. These high and low-speed winds interact with the Earth's magnetic field to produce geomagnetic storms.

The Ulysses spacecraft has passed over the Sun's north and south poles in its course of completing two orbits through the solar system. It played an important role in solar wind studies by measuring its speeds and composition in different regions. It also provided magnetic field measurements. The Advanced Composition Explorer (ACE) satellite that was launched in August 1997 also shed more light on the solar wind. It is placed at the L1 Lagrangian point between the Earth and the Sun. The L1 point is one of the five Lagrangian points in space where the gravitational attraction of the Sun and the Earth are equal and opposite. L1 is located about 1.5 Mkm from the Earth in the direction of the Sun. India's first solar mission, Aditya L1 to be launched to the L1 point in mid-2023 is another spacecraft dedicated to solar atmospheric studies. It has eight instruments onboard whose science objectives include photospheric and chromospheric imaging, solar wind and particle analysis, magnetic field topology, physics of coronal heating, dynamics and origin of CMEs, to name a few.

1.10 Eclipses

An eclipse is an astronomical phenomenon that occurs when one astronomical body moves into the shadow of another astronomical body. When the moon orbits the Earth, it can sometimes come between the Sun and the Earth, blocking the sunlight from reaching the Earth. This causes an eclipse of the Sun (Figure 1.15). The shadow casted by the moon on the Earth will have two regions, the umbra and the penumbra. The umbra is the dark centre of the moon's shadow. The moon's shadow gets smaller as it reaches the Earth. The penumbra is the outer lighter region. It gets larger as the Moon's shadow reaches the Earth. The three different types of eclipses are explained below.

Total solar eclipse: The visible surface of the Sun is completely blocked by the moon in this case. The sky becomes very dark during the totality. For a total eclipse to occur, the Sun, moon and Earth must be aligned in a straight line. The people who see this will be at the centre of the

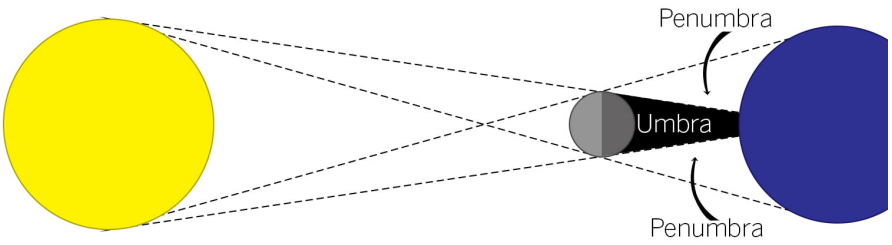

Figure 1.15: Geometry of a typical solar eclipse

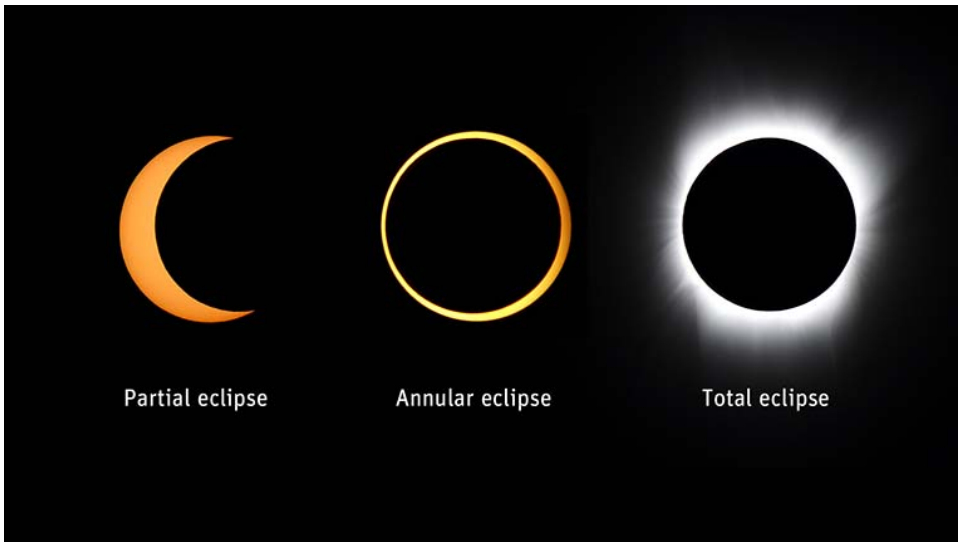

Figure 1.16: From left to right, this image shows a partial solar eclipse, annular solar eclipse, and total solar eclipse. A hybrid eclipse switches between a total and an annular eclipse.

moon's shadow on the Earth. Interestingly, for the given distances between the Sun, Earth, and the moon, the size of the moon is the same as the size of the photosphere as seen from the Earth. This is the reason for total solar eclipses to occur.

Partial solar eclipse: This happens when the Sun, moon and Earth are not exactly aligned. The photosphere is partially blocked by the moon leaving behind some part of the bright photosphere still visible.

Annular solar eclipse: An annular eclipse occurs when the moon is at the farthest distance from the Earth because of which it appears smaller. The moon blocks the Sun, leaving a circular ring of the larger photospheric disk.

Figures for all three types of eclipses can be seen in Figure 1.16. Solar eclipses happen every 18 months somewhere on Earth. Unlike lunar eclipses, solar eclipses last only for a few minutes.

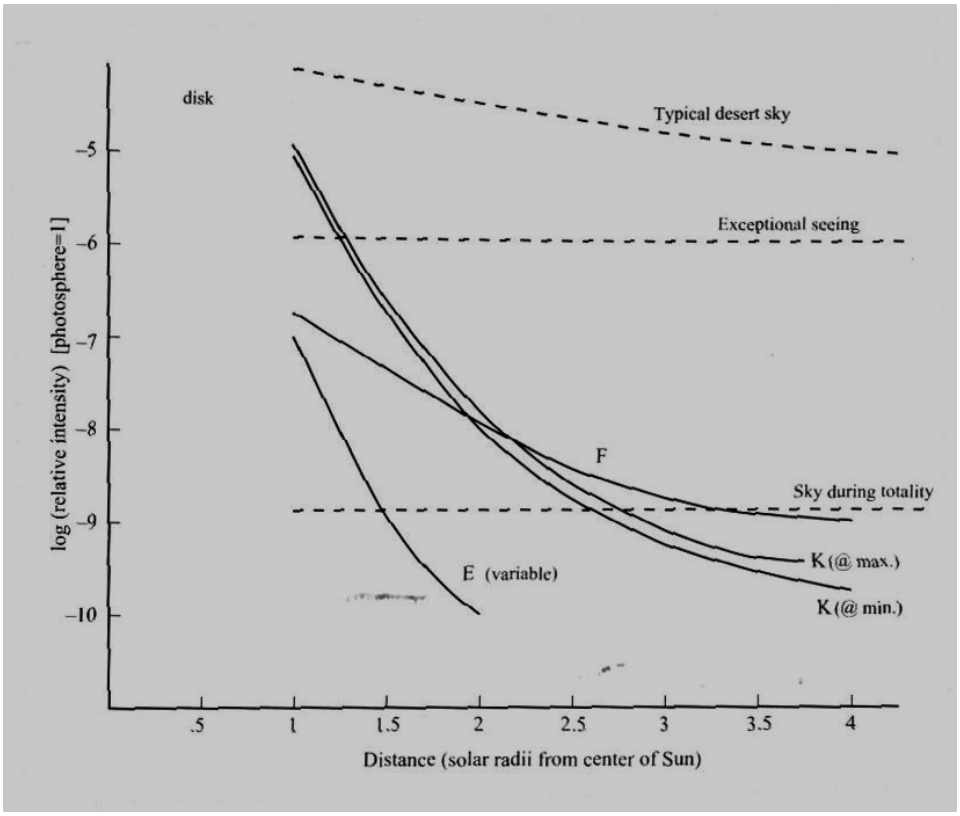

Figure 1.17: Brightness variation in the main components of the solar corona as a function of radial distance.

1.10.1 Eclipses for Studying the Solar Corona

The solar corona is extremely dim to be seen in normal daylight. The photospheric light is so bright and intense that one cannot see the corona normally. The coronal brightness is so low that even a typical desert sky brightness is way too high (Figure 1.17). So, the only way to see the corona is by blocking out the photosphere. During total solar eclipses, the corona is visible. This is the apt time for physicists to study the solar atmosphere.

The difficulty of observing the faint corona and the great advantage of a total solar eclipse where the background intensity is greatly reduced is a well-defined situation for ground-based coronal studies. The emission lines cover only about $1/1000^{th}$ of the wavelength range. So, a given line is 1000 times more intense per Å than the continuum. Thus, by using narrow-band filters during totality, one can effectively discriminate the line emission against the continuum. It may be noted that the maximum duration of a total solar eclipse is only about 7 minutes.

However, one cannot always wait for natural eclipses to happen to study the solar corona. It does not make much sense in waiting and carrying heavy instruments to some part of the world for observations of only a few minutes. One needs sufficient observational time to study long-term processes such as coronal waves. So the alternative way is to create artificial eclipses. A coronagraph just does that.

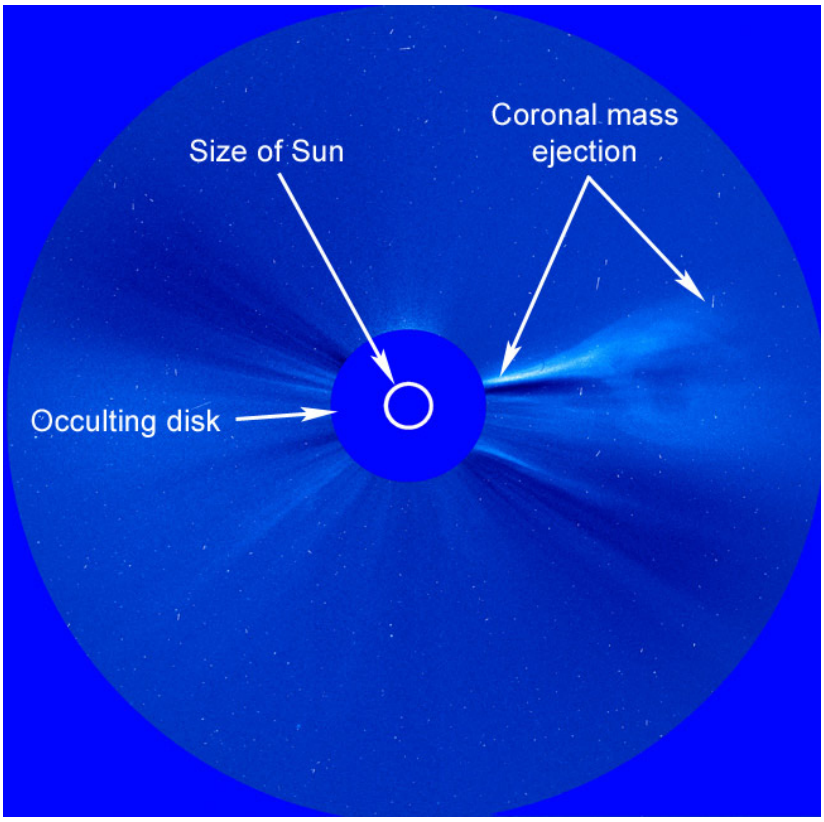

Figure 1.18: Image of STEREO occulting the Sun. A CME can be seen ejected against the dark space background.

1.10.2 Coronagraphs

Coronagraphs are instruments that block out the photospheric light and enable us to observe the solar atmosphere through artificial eclipses. These instruments can be ground-based or space-based. In modern days with so much of advancements in science and technology, almost all space-based solar missions are built with coronagraphs, especially the ones meant for solar atmospheric studies. Ground-based telescopes are also incorporating this feature. This also enables us to observe the Sun constantly from various positions and angles. However, this does not mean that we need not observe the Sun during natural total solar eclipses. There are still some lower regions of the Sun's atmosphere that are only visible during total solar eclipses. The disk of a coronagraph must block out the somewhat larger part of the corona to avoid stray light due to diffraction.

Figure 1.18 shows STEREO, one of the popular coronagraphs in recent times, blocking the photospheric disc, due to which the wispy corona is clearly visible. It also shows a CME being blown out. The occulting coronagraph disc also shows the size of the Sun which explains how the lower corona is blocked out by the coronagraph. SOHO, STEREO, GOES, Hinode, WIND, YOKHOH are some of the main coronagraphs to name a few.

1.11 Motivation

The transition region and the solar corona are widely explored for their several intriguing features. The dynamics of the flows and mass motions, the existence of multiple component line profiles, line shifts, non-thermal velocities, intensity variations in different regions, and solar cycle variations of physical parameters are a few topics that are actively studied. The heating of the coronal plasma to millions of degrees, the acceleration of the solar wind, and the reasons behind the dynamic solar atmosphere are not fully explained. The physical connection between the mass motions in the solar atmosphere and the coronal heating and possibly the solar wind needs to be probed in more detail. This may give a better understanding of the coronal dynamics.

Some of the major findings that led us to our work are:

- The multi-component nature of the coronal line profiles.
- Asymmetries have been generally reported in the spectral lines from the transition region and the solar corona. Redshifts are generally seen in the transition region and blueshifts in the coronal region.
- Dominant blueshifts in coronal lines are reported recently and these are interpreted in terms of nascent solar wind flow or type-II spicules.
- The inter-dependency of line profile parameters is observed, especially the line width, Doppler velocity and centroid.
- The coronal line profiles are known to have non-thermal line widths in addition to the thermal widths.
- There has been a difference in the results regarding the variation of the non-thermal velocity and line width with height.
- Smaller mass motions driven from chromospheric regions can contribute to the hot plasma in the corona. However, their role in coronal heating is being debated.
- Large outflows in the boundaries of the active regions have been discovered in recent years.

Based on the above findings, we would like to further examine the two important and interconnected problems in astronomy, namely the solar coronal heating and acceleration of the solar wind. We would also like to study the solar cycle variations of physical parameters. We used Fabry-Perot interferometric observations during 2001 June 21 total solar eclipse and Hinode/EIS observations. We obtained emission line profiles in the Fe XIV 5303 Å (coronal green line) from the eclipse observations and Fe XII 195.12 Å (EUV) from Hinode. The line profiles are the little rosetta stones of the corona. They give a lot of information about the source. The specific aims of the thesis are the following:

- To study the solar corona at two different levels. The formation temperature of Fe XIV 5303 Å is 1.8 MK and that of Fe XII 195.12 Å is 1.25 MK.
- To study the variation of line profile parameters like intensity, line width, non-thermal width, Doppler velocity, asymmetry and line centroid. The differences in the active region, quiet region and coronal hole are examined. The radial variations are also studied. This may give insights into coronal beating and solar wind acceleration.
- To study the nature of multiple components. Detailed examination to see the number of components, redshifts, blueshifts and asymmetry. This may give clues on coronal heating.
- The study the inter-dependence of line profile parameters and its variation with the coronal magnetic activity. A positive correlation between Doppler velocity and line width gives hints about heating sources.
- To examine the dependence of line profile parameters on solar cycle. This gives clues on coronal heating as well as solar irradiance.
- To simulate emission line profiles and compare them with the observations.

Chapter 2

Coronal Spectroscopy & Emission Line Profile Simulations

2.1 Coronal Spectroscopy

Spectroscopy is a scientific tool used to get the spectra of an object. It was through spectroscopy, Fraunhofer lines were discovered in the solar spectrum. The composition of the Sun and other stars are also discovered using this method as each element carries its unique feature like a fingerprint. Important information about distant astronomical objects is also obtained by studying their spectra. This explains the need for high-end telescopes that can collect more photons from distant objects. Light is split into its component wavelengths in this process. Imaging using different types of cameras is a major part of spectroscopy. An overview of various spectrometers is given in the following section.

2.1.1 Spectroscopic Instruments

Spectroscopic instruments are meant for imaging the dispersed light into its component wavelengths and thereby providing information about the source object. Spectrometers record the spectra without imaging them. In spectrographs, the spectra are recorded on a CCD detector and are saved onto a computer in required formats for further processing and analysis. They cover different ranges of wavelengths and offer different spectral resolutions for observing an astronomical object or an event. The higher the spectral resolution, the stronger the dispersion of the light, and the smaller the details of the spectrum that can be detected. Some spectrographs can produce high-resolution spectra while others obtain spectra of many objects at the same time and a few can even take spectra over their whole field of view. There are various types of spectrometers and a basic understanding of them is relevant to our study.

Prism Spectrometers

Prisms make use of the fact that the refractive index of all materials changes with wavelength. Light is refracted differently by different refractive indices. Prisms need not be triangular, but it is the simplest shape with the fewest surfaces that produces dispersion.

Grating Spectrometers

Grating spectrometers make use of the diffraction of light from a regularly spaced, ruled surface. They disperse the light by a combination of diffraction and interference. Gratings include ruled gratings, holographic gratings and replica gratings made from mold of gratings that have been ruled.

Interferometers

In interferometers, two or more sources of light are merged to create an interference pattern, which can be measured and analyzed. The spectral resolution is primarily determined by the maximum path difference attained during the interferogram measurement. Both interfering wavefronts in the interferometer are driven to cover a large path difference for achieving a high spectral resolution.

In all spectrometers, the luminosity is inversely proportional to its resolving power (Jacquinot 1954, 1960) and is given by,

$$L \times R = constant$$

where the luminosity or the etendue of the spectrometer is

$$L = \epsilon A \Omega.$$

Here ϵ is the transmission factor, A the effective area of the spectrometer and Ω is the solid angle subtended by the slit or the entrance aperture of the collimator.

The following relation holds only when the source fills the acceptance angle of the spectrometer. The large gain in the $L \times R$ for an interferometer is due to its large acceptance angle for a given resolving power. This advantage is known as the Jaquinot advantage which is given by the following relation,

$$(L \times R)_{FP} \approx 30 \text{ to } 100 (L \times R)_{grating} \approx 300 \text{ to } 1500 (L \times R)_{prism}$$

There are many different types of interferometers like Michelson-Morley, Fourier transform, Fabry-Perot etc. Fabry-Perot interferometers have been used in astronomy since the development of high-reflective dielectric coatings. It is a powerful combination of high resolution and superior light-gathering capability. It makes an ideal instrument for observing extended astrophysical objects like the solar corona, emission nebulae, planetary nebulae, etc.

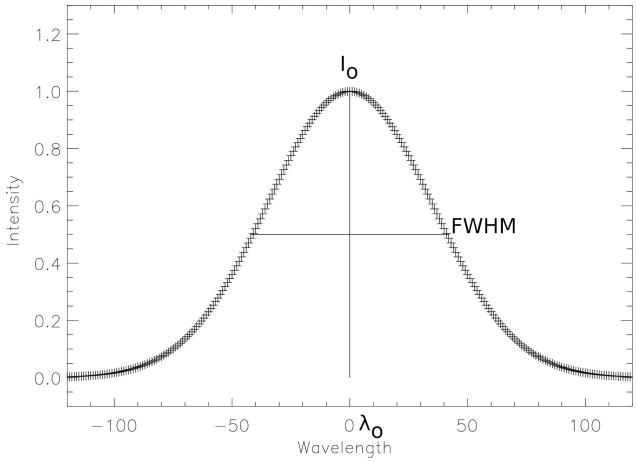

Figure 2.1: An ideal line profile showing the readily available parameters peak intensity, rest wavelength and the full-width half maxima (FWHM).

2.1.2 Line Profile

The study of coronal emission line profiles tells us about the physical and dynamic state of coronal structures like the intensity, Doppler velocity, line width, asymmetry, temperature, density, turbulence and mass motions.

The spectral line which is formed during atomic transitions is not as narrow as they appear. They have a finite width. It has a measurable value which depends on many factors. A graph of intensity versus wavelength (or frequency) is called a line profile (Figure 2.1). The line profiles are ideally Gaussian functions. However, practically, there are a lot of factors that add to the broadening of these line profiles. They are mentioned below:

- **Collisional Broadening**

  The phenomenon is accountable for the broadening of spectral lines due to the collisions between the excited atoms which can become predominant in the high-density gas plasma. In this case, the spectral line profile is not a Gaussian, but a Lorentzian which is characterized by a narrower spike and longer wings.

- **External Fields Broadening**

  Magnetic or electric fields cause the Zeeman effect or the Stark effect with the splitting of the spectral lines. The final result causes the broadening of spectral lines.

- **Intrinsic Broadening**

  The intrinsic or natural broadening is due to the uncertainty in the energy levels. According to Heisenberg's uncertainty relation,

$$\Delta E \Delta t \approx \hbar,$$

the frequency of the photon emitted has an intrinsic uncertainty given by:

$$\Delta \nu \approx \Delta E/h \approx 1/2\pi\Delta t.$$

The value of this uncertainty is very low and is absolutely negligible.

- **Thermal/Doppler Broadening**

  This broadening is due to the Doppler effect that occurs when the radiating atoms have a movement relative to the observer. The random movement of the atoms is directly related to the temperature, which is why this broadening mechanism is also called thermal broadening. As we know from the Maxwell-Boltzmann statistics, the speed of gas atoms follows a Gaussian profile and the mean energy is of the order of kT, where k is the Boltzmann constant and T is the temperature. Mathematically, it can be shown that the spectral line broadening profile is also Gaussian, with a value given by,

$$\frac{\Delta\lambda_D}{\lambda_0} = 2\sqrt{2\ln 2\frac{kT}{mc^2}}$$

  This equation shows that broadening increases with temperature and is higher for lighter atoms.

- **Microturbulence/Non-thermal Broadening**

  There are many small cells of gas moving in random directions with a Maxwellian velocity distribution in a source. The size of the turbulent cells is very small compared with the optical depth. So, when we look through a stellar atmosphere, we see many cells of gas whose distribution of velocity components is Gaussian and this constitutes the microturbulence broadening. Microturbulence is generally present in coronal line profiles. The estimated non-thermal motion in the corona typically ranges from 10—30 kms^{-1}. This is often comparable to the thermal widths themselves.

  In addition to this, the presence of discrete moving components such as coronal loops may also produce a significant deviation of the line profile from the Gaussian nature. Both thermal and non-thermal broadening result in a Gaussian profile. So, in a Gaussian spectrum, it is difficult to separate the thermal broadening and microturbulence. But, in principle, it is possible to distinguish the two and determine separately the kinetic temperature and the microturbulent speed.

- **Instrumental Broadening**

  A spectral line is also affected by instrumental broadening. Almost any type of spectrograph will broaden a line. The broadening produced by a prism is inversely proportional to the size of

the prism, and the broadening produced by a grating is inversely proportional to the number of grooves on the grating. If the spectrum is recorded digitally, it is still further broadened by the point spread function. The instrumental broadening can be determined in a laboratory by measuring the instrumental profile of an intrinsically narrow line. Later, when the instrument is used to examine a broadened line, the observed profile is the convolution of the true profile and the instrumental profile.

So, depending on these broadening mechanisms, a line profile might either be a single component or multiple components overlapping. This can be determined by fitting a Gaussian profile to it. In case of the existence of multiple components, two or sometimes three Gaussian curves are fitted. The science of what gives rise to multiple components explains a lot about the physical features of the source. The physical parameters available from a line profile are its intensity, line width, Doppler velocity, asymmetry, centroid etc. One can further deduct its temperature, density, mass motions etc. For an emission line, we can measure the spectral line profile relative to zero intensity, while for an absorption line, we can measure the spectral line profile relative to the continuum level.

2.2 Emission Line Profile Simulations

In the previous section, we found that the values of the line profile parameters of the individual components affect the resultant line profile. Hence, it is important to learn the influences of these parameters. We have simulated a line profile considering a stationary main component and a varying subsidiary component. We changed the intensity, velocity and line width of the subsidiary component and obtained the resultant component in all cases. This shows us how the input parameters of the two components affect the resultant profile.

We define Doppler velocity as the velocity corresponding to the wavelength of the peak intensity. Centroid velocity is the velocity corresponding to the wavelength point that divides the area of the line profile into two equal halves (Dadashi, Teriaca, and Solanki 2011). When the line profile is an ideal Gaussian, the two quantities are the same, but when there is an asymmetry in the line profile, they tend to be different. This is shown through a simple simulation. A line profile is created by adding a stationary main component (intensity = 1 unit, velocity = 0 km s^{-1}, width = 35 mÅ) and a moving subsidiary component (intensity = 0.3 unit, velocity = 30 km s^{-1}, width = 35 mÅ). To make the profile look more realistic, we have added 2.5 % random noise. The line profile is now fitted with a Gaussian, and then we obtained the Doppler velocity and centroid velocity.

The results are shown in Figure 2.2 and Table 2.1. It can be seen that the Doppler velocity and centroid velocity are different. In the analysis, the centroid is expressed in km s^{-1} so that its comparison with the Doppler velocity is easier. Figure 2.2 gives an estimate of the error as well. The maximum error obtained from the simulation is 0.23 km s^{-1} in the Doppler velocity and 0.76 km s^{-1} in the centroid. However, a more realistic calculation considering the instrumental parameters gives the error as 1.6 km s^{-1} (Dere et al. 2007).

Table 2.1: Table showing the values of Intensity (Arbitrary Units), Velocity (km s^{-1}), and Width (mÅ) for the Simulated Main and the Subsidiary Components with the Values of Velocity, Centroid (mÅ), and Width for the Fitted Curve.

No.	**Component**						**Fitted Gaussian**		
	Main			**Sub**			Vel (km s^{-1})	Cen (km s^{-1})	Wid (mÅ)
	Int	Vel (km s^{-1})	Wid (mÅ)	Int	Vel (km s^{-1})	Wid (mÅ)			
1	1.0	0.0	35	0.3	0.0	35	0.002±0.12	0.0±0.00	35.01±0.18
2	1.0	0.0	35	0.3	10.0	35	2.26±0.11	2.21±0.76	35.59±0.19
3	1.0	0.0	35	0.3	20.0	35	4.26±0.13	4.60±0.06	37.31±0.21
4	1.0	0.0	35	0.3	30.0	35	5.77±0.14	6.15±0.00	39.93±0.22
5	1.0	0.0	35	0.3	40.0	35	6.67±0.17	7.65±0.20	43.10±0.26
6	1.0	0.0	35	0.3	50.0	35	6.83±0.19	7.84±0.46	45.76±0.32
7	1.0	0.0	35	0.3	60.0	35	6.12±0.23	8.66±0.74	47.08±0.42

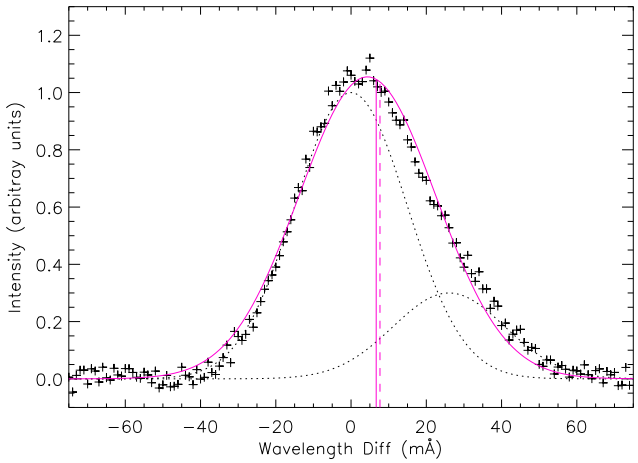

Figure 2.2: Simulation showing a line profile with a stationary main component and a moving subsidiary component with 2.5% random noise fitted with a Gaussian. The vertical lines show the corresponding Doppler velocity (solid) and centroid (dashed). Details are given in Table 2.1.

2.2.1 Simulations of Doppler Velocity Variations

The calculations explained in the above section are repeated by changing the velocity of the secondary component in the range 0 – 60 km s^{-1} with an interval of 10 km s^{-1}. The values of the intensity and line width are kept constant. In each case, the simulation was run 1000 times. The main result of the simulations is shown in Figure 2.3. The behaviour of line width versus Doppler velocity/centroid of the resultant line profile shows that the Doppler velocities and centroid velocities are not the same, especially when the velocities are large. It can be seen that the variation is not linear but shows some non-linear nature. It can also be seen that the estimated velocities and centroids in the single Gaussian fit are much smaller than the actual values. The estimated velocity decreases when the

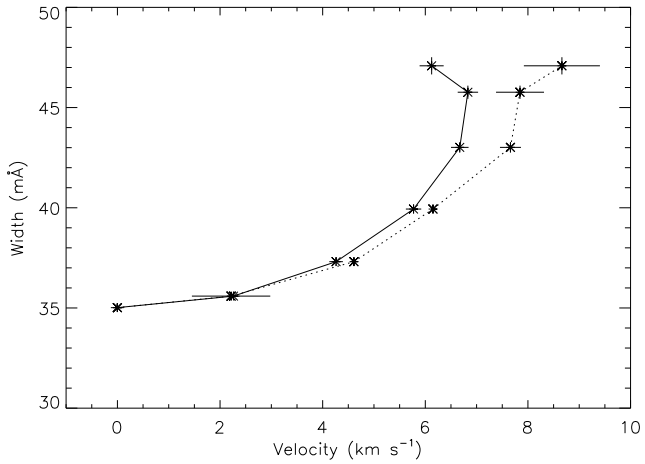

Figure 2.3: Plot showing the variation of the line width with Doppler velocity (solid)/centroid (dotted). Details are given in Table 2.1.

velocity of the secondary component is 60 km s^{-1}. The values of these simulations are mentioned in Table 2.1. These results will be compared with actual observations in the later chapters.

2.2.2 Simulations of Line Width Variations

Here, we have considered the same main component (intensity = 1 unit, velocity = 0 km s^{-1}, width = 35 mÅ) and a subsidiary component with varying line width (intensity = 0.3 unit, velocity = 30 km s^{-1}, width = 20 – 50 mÅ). We have varied the line width of the subsidiary component in units of 5 mÅ. With have simulated the resultant line profile with these parameters and examined how the Doppler velocity varies from the centroid velocity. The variation of these two parameters with line width can be seen in Figure 2.4. The Doppler velocity starts decreasing at higher values of the given width and the centroid velocity becomes almost constant. It can be seen that the nature of variation of these two parameters is similar to what is seen in the case of Figure 2.3. The intensity, velocity, centroid and width values of the main, subsidiary and resultant components can be seen in Table 2.2.

2.2.3 Simulations of Intensity Variations

In this case, we have considered the same main component (intensity = 1 unit, velocity = 0 km s^{-1}, width = 35 mÅ) and a varying subsidiary component (velocity = 30 km s^{-1}, width = 35 mÅ). The intensity of the subsidiary component is varied from 0.1 - 0.7 units in units of 0.1. We have simulated a line profile to check how the Doppler velocity varies from the centroid velocity in this case. The variation of these two velocities with line width can be seen in Figure 2.5. The nature of variation of these two parameters is found to be quite different from the previous cases. Both the Doppler velocity and the centroid velocity are found to have close values due to which their curves almost

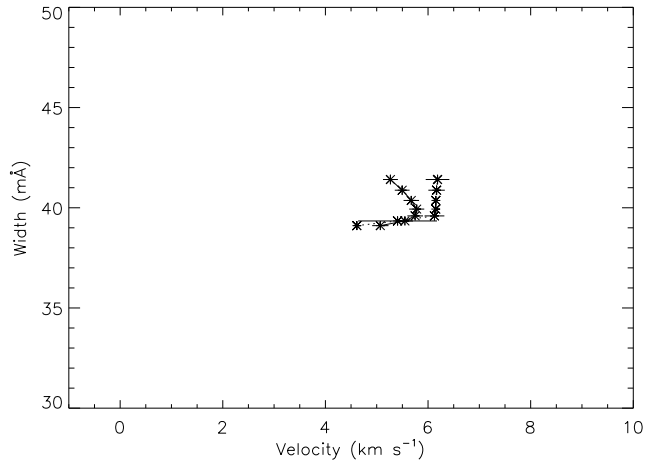

Figure 2.4: Plot showing the variation of the line width with Doppler velocity (solid)/centroid (dotted) when the line width of the subsidiary component is varied gradually. Details are given in Table 2.2.

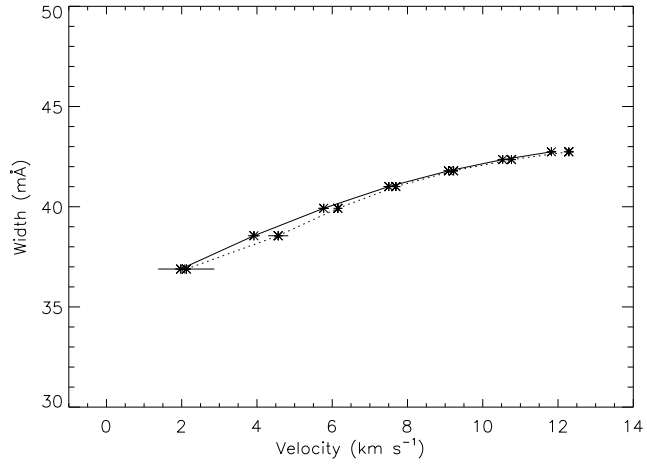

Figure 2.5: Plot showing the variation of the line width with Doppler velocity (solid)/centroid (dotted) when the intensity of the subsidiary component is varied gradually. Details are given in Table 2.3.

overlap. This indicates that as the intensity of the subsidiary component increases, the resultant line profile tends towards an ideal Gaussian. The details of the simulations are tabulated in Table 2.3.

2.3 Conclusions

A line profile is simulated by combining a stationary main component and a varying subsidiary component. The intensity, velocity and line width of the subsidiary component are varied and the resultant profile is examined. It is found that the input parameters of the two components affect the resultant profile. The estimated velocities and centroids in the single Gaussian fit are much smaller than that of the subsidiary component. The resultant line profile is found to be more

Table 2.2: Table showing the values of line width (Arbitrary Units), Velocity (km s^{-1}), and Width (mÅ) for the Simulated Main and the Subsidiary Components with the Values of Velocity, Centroid (mÅ), and Width for the Fitted Curve.

No.	**Component**						**Fitted Gaussian**		
	Main			**Sub**			Vel (km s^{-1})	Cen (km s^{-1})	Wid (mÅ)
	Int	Vel (km s^{-1})	Wid (mÅ)	Int	Vel (km s^{-1})	Wid (mÅ)			
1	1.0	0.0	35	0.3	30.0	20	5.07±0.15	4.61±0.06	39.10±0.22
2	1.0	0.0	35	0.3	30.0	25	5.54±0.15	5.40±0.76	39.34±0.22
3	1.0	0.0	35	0.3	30.0	30	5.74±0.15	6.12±0.19	39.59±0.22
4	1.0	0.0	35	0.3	30.0	35	5.77±0.14	6.15±0.00	39.93±0.22
5	1.0	0.0	35	0.3	30.0	40	5.67±0.15	6.15±0.04	40.36±0.23
6	1.0	0.0	35	0.3	30.0	45	5.49±0.14	6.16±0.16	40.87±0.24
7	1.0	0.0	35	0.3	30.0	50	5.26±0.14	6.18±0.23	41.40±0.24

Table 2.3: Table showing the values of intensity (Arbitrary Units), Velocity (km s^{-1}), and Width (mÅ) for the Simulated Main and the Subsidiary Components with the Values of Velocity, Centroid (mÅ), and Width for the Fitted Curve.

No.	**Component**						**Fitted Gaussian**		
	Main			**Sub**			Vel (km s^{-1})	Cen (km s^{-1})	Wid (mÅ)
	Int	Vel (km s^{-1})	Wid (mÅ)	Int	Vel (km s^{-1})	Wid (mÅ)			
1	1.0	0.0	35	0.1	30.0	35	1.97±0.15	2.12±0.74	36.89±0.23
2	1.0	0.0	35	0.2	30.0	35	3.91±0.15	4.56±0.26	38.55±0.23
3	1.0	0.0	35	0.3	30.0	35	5.77±0.14	6.15±0.00	39.92±0.22
4	1.0	0.0	35	0.4	30.0	35	7.50±0.14	7.69±0.06	41.00±0.21
5	1.0	0.0	35	0.5	30.0	35	9.08±0.13	9.22±0.00	41.78±0.21
6	1.0	0.0	35	0.6	30.0	35	10.52±0.13	10.76±0.00	42.35±0.19
7	1.0	0.0	35	0.7	30.0	35	11.82±0.12	12.28±0.13	42.73±0.17

sensitive to the variations of velocity and line width than the intensity of the subsidiary component. In the case of velocity variations, the behaviour of line width with Doppler velocity shows that the resultant velocity starts decreasing at higher values, while the centroid continues to increase. In the case of line width variations, the results are similar with the velocity decreasing, but the centroid tends to become constant. In the case of intensity variations, the result is peculiar with the velocity and centroid being almost similar. The simulations carried out here are a sample of how the parameters of the subsidiary component can affect the resultant component. There can be more realistic situations where the parameters of the two components are simultaneously varied. There can also be a possibility of the presence of a third component which is intended to be attended to in the future.

Chapter 3

Fabry-Perot Interferometric Studies of the Solar Corona in 5303 Å

3.1 Introduction

This chapter[1] deals with the solar coronal studies from the data obtained from the ground-based Fabry-Perot interferometric observations in the coronal green line Fe XIV 5303 Å. The instrument design and observations were carried out by the Physical Research Laboratory team during the total solar eclipse of 21 June 2001 in Lusaka, Zambia. The details of the analysis and results are described in Maya Prabhakar, Raju, and Chandrasekhar 2019.

The method of chemical analysis of incandescent gases by means of spectroscopy came into practice during the second half of the 19^{th} century. This technique was further extended to analyze the solar atmosphere as well as to explore the source object's thermal, chemical and kinematic details. The trend of carrying the spectroscopes during eclipse expeditions was gradually setting in. There are reports that show the flash spectrum being observed during the 1868 eclipse in India. The first report on the hot solar atmosphere comes from the 1869 eclipse observation of the 5303 Å coronal green line by Young and Harkness. It was gradually understood that solar eclipses mask the dominating high-intensity photospheric light, which makes the solar corona visible. From the 1870 eclipse, Young found that most of the emission lines in the flash spectrum correspond to the dark absorption lines. A major study of the flash spectrum was made by Donald H. Menzel and W.W Campbell during the 1898 eclipse. Later on, studies also showed how it is the E corona that holds the information on the actual coronal light. This shows how the studies of the solar atmosphere started with ground-based instruments.

Fabry-Perot (FP)interferometers have been widely used in astronomy, especially since the development of high-reflectivity dielectric coatings and the introduction of optically contacted etalons. It is known to have a large luminosity-resolution product. This makes it an ideal instrument for

[1]This chapter presents the work published in Maya Prabhakar, K.P Raju & T. Chandrasekhar, 2019, Solar Physics, Volume 294, 26

observing relatively isolated emission lines from an extended source like the solar corona. As we know, the structure of the inner corona is more evident in the light of the emission lines than in the continuum. Hence, in addition to the photographic techniques, it is a valuable tool for probing the corona with good spatial and spectral resolution.

Several attempts were made to use FP interferometers during eclipses. The first successful attempt comes from Jarrett and von Klüber 1961 who made eclipse observations from the Tokelau Islands of the South Pacific. The solar corona was observed using a FP interferometer in the coronal green and lines. They obtained good interference fringes up to 1.8 $R_{\odot}$. Many line profiles and halfwidths, corrected for instrumental broadening, were determined for both the coronal lines. Coronal temperatures were derived from both of them. The mean temperature for the green line was found to be about 3.2 MK and for the red line, it was 3.5 MK, with an error of about 10 %. The first successful eclipse coronal line observations by a FP etalon gave an impetus to the coronal research. The E-coronal interferograms in Fe XIV 5303 Å and Fe X 6374 Å have acquired a commendable practice today. The so-called image spectrum (interferogram) gives an instant picture of intensity, line width and velocity fields.

In later years, a photographic FP interferometer was used to measure the width and wavelength of the Fe XIV λ5303 line in the solar corona during the 7 March 1970 eclipse in Mexico. Eclipse interferograms of the solar corona of 1972 and 1981 (Scatliff 1973; Stellmacher, Koutchmy, and Lebecq 1986), indicated that coronal conditions are relatively quiet, but not homogeneous. Coronal spectra during the total solar eclipse of 16 February 1980, were obtained in Fe X λ6374 were obtained by using a multi-slit spectrograph by Singh, Saxena, and Bappu 1982. Eclipse data on the large-scale velocity field of the coronal green line were obtained by Kim 1994 by using a FP interferometer. We have analyzed the FP interferograms obtained during the total solar eclipse of 21 June 2001.

In the following sections, we explain the choice of the coronal green line, FP instrumentation, and observational details of the 21 June 2001 eclipse followed by the results and discussions from our work.

3.2 The Coronal Green Line

The coronal green line Fe XIV 5303 Å arises out of a forbidden (magnetic dipole) transition in the ground state of Fe XIV ion. The various line parameters can be seen in the following Table 3.1. The formation temperature of this line is 1.8 MK (Jordan 1969), which is very close to the inner coronal temperature (2 MK). Hence, it is the most preferred line to study the coronal features.

3.3 Fabry-Perot Interferometer

The FP etalon essentially consists of two optically flat fused silica plates held accurately parallel to one another at a fixed distance. The facing surfaces of the plates are so flat that it is better

Table 3.1: Coronal Green Line characteristics

No.	Parameters	Values
1.	Rest wavelength	5302.86 Å
2.	Ion	Fe XIV
3.	Transition	^{3} P ; ^{2} P $_{3/2}$ - ^{2} P $_{1/2}$
4.	Spontaneous transition probability	60 s^{-1}
5.	Excitation potential	2.4 eV
6.	Ionization potential	355 eV
7.	Temperature at which the line intensity reaches a maximum value	1.86 MK
8.	Optical depth in the line (van de Hulst 1953)	10^{-4}

Table 3.2: FP Etalon parameters

No.	Parameters	Values
1.	Plate diameter	50.8 mm
2.	Working aperture	40 mm
3.	Plate flatness	$\lambda/100$
4.	Quoted air spacing	300 μm
5.	Spectral range of reflection coating	4500 —5500 Å
6.	Reflectivity at 5000 Å	90($\pm$1) %
7.	Reflectivity R at λ5303 Å	(87$\pm$1) % Å

than $1/100^{th}$ of the wavelength of operation and are coated with metal or dielectric films of high reflectivity (usually $\approx$ 90%). A light ray incident at a particular angle on the plates undergoes multiple reflections inside the etalon. Successively reflected rays emerge parallel with a constant path difference. A camera lens can bring all these rays to focus at a point in the focal plane.

The transmission of light through these plates is governed by Airy's function which is given by,

$$A(\lambda) = I_0(\lambda)\left(\frac{T}{1-R}\right)^2\left[1+\frac{4R}{(1-R)^2}\sin^2(\frac{2\pi\mu t\cos\theta}{\lambda})\right]^{-1} \tag{3.1}$$

where T is the transmission coefficient, R is the reflectivity of the mirrors, θ is the angle of incidence, μ is the refractive index of the medium between the plates in the etalon (Bates 1977; Thorne and Spectrophysics 1974).

The peak of transmission occurs when

$$2\mu t\cos\theta = n\lambda \tag{3.2}$$

where n is the order number. A few important parameters of the etalon are given in the following Table 3.2.

Some of the important terms which characterize an FP are explained below.

1. Free spectral Range (FSR) is the spacing between the adjacent transmission peaks : $\Delta\lambda = \frac{\lambda^2}{2\mu t}$

2. Full Width at Half Maximum (FWHM) or halfwidth of the Airy profile, also called the resolution limit: $\delta\lambda = \frac{\Delta\lambda}{N_R}$

3.Reflective Finesse : $N_R = \frac{\pi\sqrt{R}}{1-R}$

4. Peak Transmission of the Airy profile : $A_{max} = \frac{T^2}{(1-R)^2}$

5. Reflective contrast of the FP fringe : $C = \frac{I_{max}}{I_{min}} = \left(\frac{1+R}{1-R}\right)^2$

where I_{max} and I_{min} refer to the maximum and minimum intensity of the fringe respectively.

In actual practice, there may be various broadening factors in addition to Airy's function, which could reduce the contrast of the fringe (Atherton et al. 1981; Desai 1984; Hernandez 1966). In Airy's broadening, contributions to the instrumental profile also come from the following factors:

1. Microscopic flatness - imperfections of the plates

2. Spherical defects of the etalon plates

3. Finite aperture

while 1) is a Gaussian, 2) and 3) are rectangular broadening functions. The convolution of individual broadening functions to form the instrumental function has been treated in detail by Chabbal 1953, Robert Chabbal 1959, Turgeon and Shepherd 1962, Ballik 1966 and Hernandez 1966.

The experimental setup is as shown in Figure 3.1. The coronal light falls on the mirror M which is further directed towards a convex lens. This converged light passes through a filter F and then through aperture A. This light further passes through another lens L1 where it becomes parallel. This beam of light passes through the FP etalon E. The emerging beam of parallel light is once again converged in L2 which is finally obtained on the CCD screen.

This FP interferometer used is the one used in Chandrasekhar et al. 1984. However, during the 21 June 2001 eclipse, a CCD was used as the detector.

3.4 Observations

On 21 June 2001, a total eclipse of the Sun was visible from within a narrow corridor which traversed the southern hemisphere. The path of the Moon's umbral shadow began in the South Atlantic and crossed southern Africa, and Madagascar and ended at sunset in the Indian Ocean. A partial eclipse was seen within the much broader path of the Moon's penumbral shadow, which included eastern

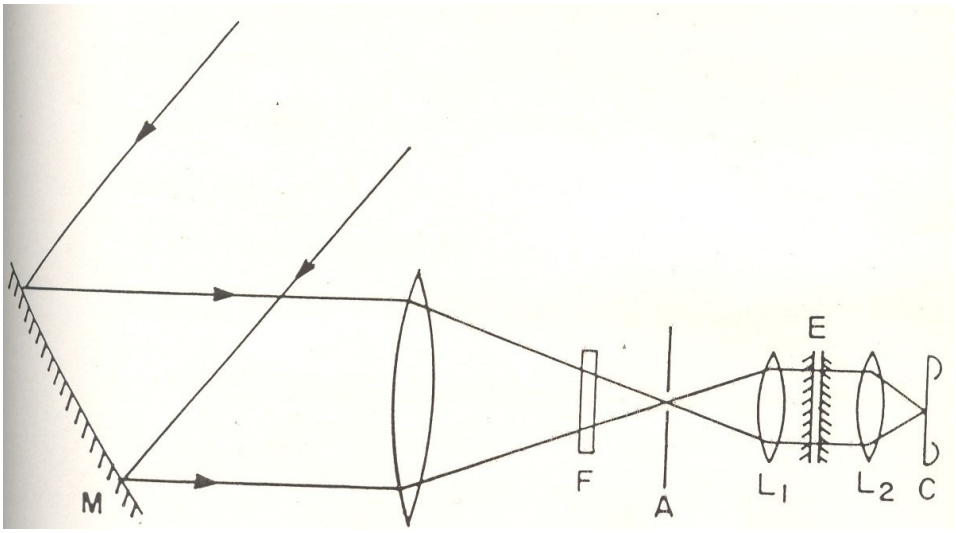

Figure 3.1: Schematic diagram of the Fabry-Perot instrumental setup used whose description can be found in Table 3.3.

Table 3.3: Instrumental features of the Fabry-Perot interferometer used for our study.

Features	Values
Free spectral range	4.75 Å
Instrumental width	0.2 Å
Spectral resolution	26,000
CCD configuration	1024 x 1024
Pixel size	24 μm
Pixel resolution	3.8 arcsec

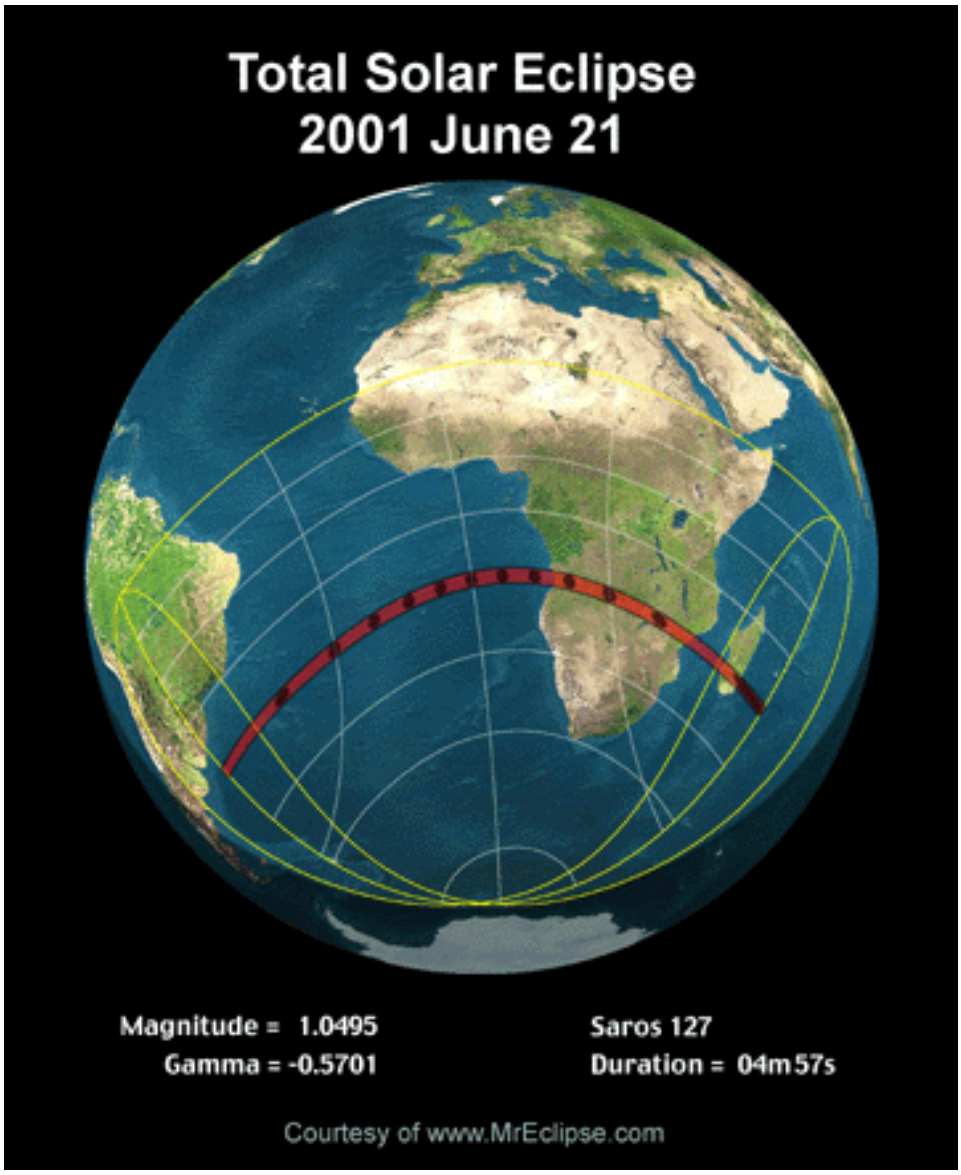

Figure 3.2: Picture showing the path traversed by the total solar eclipse of June 21, 2001 (Courtesy: NASA).

South America and most of Africa (excluding North Africa). The path traversed by this eclipse can be seen in Figure 3.2.

The observations were carried out from Lusaka, Zambia. The totality here lasted for about 3 min 37 sec. The Sun was at 31° elevation above the northwest horizon.

During the span of the totality, 14 interferograms were obtained. Part of the data obtained during this particular eclipse was used by Raju, Chandrasekhar, and Ashok 2011b and M. Prabhakar, Raju, and Chandrasekhar 2013.

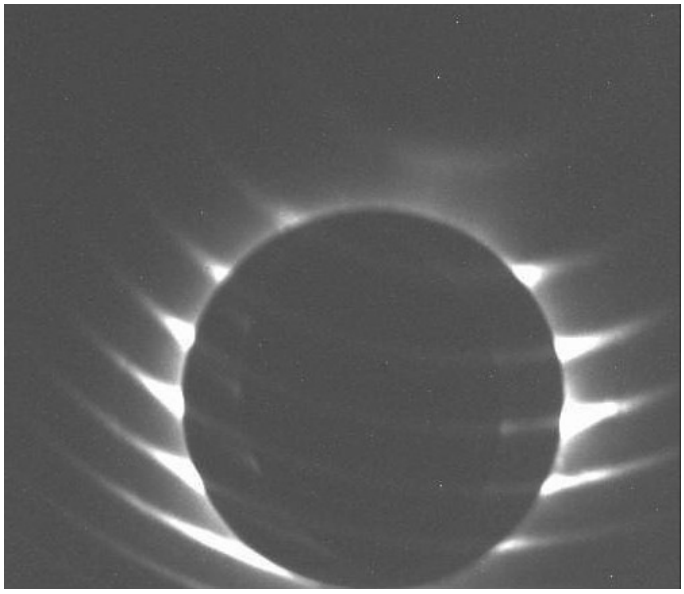

Figure 3.3: A typical Pabry-Perot interferogram analyzed.

3.5 Data Analysis

The interferograms were calibrated according to the standard procedure. For this, the dark and the biased image are subtracted from the raw image and then divided by the flat image. A typical calibrated interferogram can be seen in Figure 3.3. We can see the silhouette of the moon eclipsing the Sun. The white rings are the interference rings formed from the coronal light that gets exposed when the photosphere is eclipsed. This is the source of light that has to be studied to analyze the solar corona.

The line profiles have been extracted in the angular range of 240°. The original plan of the experiment was to get a time sequence of Fabry-Perot interferograms of the solar corona during the total solar eclipse. The aim was to study the temporal changes in the physical properties of the solar corona. But due to a minor tracking error that happened during the observation, it was later noticed that the interferograms are not co-spatial. Hence, we could not study the temporal variations. However, this enabled us to study the corona at more spatial locations than was originally planned.

In a Fabry-Perot interferogram, the region between two adjacent fringe minima constitutes a line profile. Hence the spatial resolution in an imaging Fabry-Perot interferometer is generally low. It is about 0.2 $R_\odot$ in the present observation. The tracking error in the observation will shift an interferogram with respect to the previous one, leading to the formation of a new fringe pattern in the gap. This will give line profiles from new locations albeit with some boxcar averaging of the nearby spatial points. Hence the angular coverage remains the same (240°) as in a single interferogram, but we get more line profiles from the intermediate regions. All the spatial locations of the line profiles obtained are plotted on an Extreme ultraviolet Imaging Telescope (EIT) image of the Sun obtained during the same time as that of the eclipse, which can be seen in Figure 3.4.

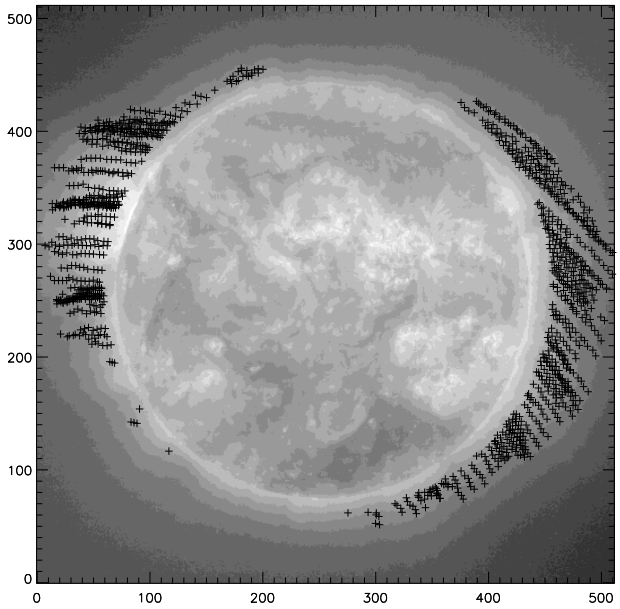

Figure 3.4: EIT image of the Sun on 21 June 2001 at time 13:48:13 showing the spatial locations of all the line profiles analyzed.

The analysis procedure involves the following steps:

- Locating the fringe centre position in the interferogram
- Radial scans from the fringe centre
- Positional identification of the corona
- Wavelength calibration
- Continuum subtraction
- Gaussian fitting to the line profile which gives intensity, line width and Doppler velocity
- Finding the centroid (a measure of asymmetry)

The analysis is done by first locating the fringe centre position in the interferograms. Then the radial scans from the fringe centre were made to obtain the line profiles. The wavelength is calibrated as in Raju, Desai, et al. 1993.

Wavelength conversion of the x-axis in the interferograms easily follows from the constructive interference condition in FP etalon.

$$2\mu t cos\theta = n\lambda \tag{3.3}$$

By differentiating,

$$-2\mu t sin\theta \Delta\theta = n\Delta\lambda \tag{3.4}$$

$$-tan\theta = \frac{\Delta\lambda}{\lambda} \tag{3.5}$$

For small θ, we have, tan $\theta \approx \theta \approx \frac{R}{F}$ and hence,

$$\Delta\lambda = -\frac{\lambda R}{F^2}\Delta R \tag{3.6}$$

The minus sign indicates that R and λ are in the opposite sense.

Thus, the wavelength is obtained in terms of the known factors R and F. Further, in order to reduce the noise, a 2×2 pixel averaging was done at the outset. It was also noticed that the line profiles close to the limb were slightly contaminated by the scattered light in some interferograms. Therefore we have considered only those line profiles beyond 1.1 $R_\odot$. Single Gaussian curves are fitted to all the line profiles and the parameters are obtained. We have selected only those line profiles whose signal-to-noise ratio is $\geq$15 in order to get good Gaussian fits. A set of line profiles fitted with Gaussian curves is shown in Figure 3.5. The estimated errors in the fitting are about 5% in intensity, 2 km s^{-1} in velocity and 0.03 Å in width.

From the data, we first obtain the intensity, Doppler velocity, halfwidth, centroid and asymmetry at different points in the corona. The centroid is defined as the wavelength point that divides the area of the line profile into two (Raju, Chandrasekhar, and Ashok 2011b). To calculate the asymmetry, strips of equal width (0.5 Å) at equal distances (0.1 Å) from the peak wavelength are considered in the red (R) and blue (B) regions. The asymmetry is then calculated using the relation (R-B)/(R+B). Interactive Data Language (IDL) is used for computation purposes.

3.6 Results and Discussions

We obtained 1295 line profiles in all by removing the noisy profiles. We examined the nature of shifts of all these line profiles and the results can be seen in Table 3.4. We found that 59 % of them are blueshifted, 7 % are redshifted and 34 % are single components. Single components are those which fall in the asymmetry range of -0.08—0.08 Å corresponding to the Doppler velocity range of -2—2 km s^{-1}. It is interesting to see that the percentages of the single components, blueshifts and redshifts are different from what is observed in Raju, Chandrasekhar, and Ashok 2011b and M. Prabhakar, Raju, and Chandrasekhar 2013. These works considered close to 300 line profiles. In this work, the improved statistics give better reliability (a factor of about 2) to our results as compared to the above-mentioned works.

This work is primarily focused on the variations of the Doppler velocity, halfwidth, centroid, asymmetry, and their interrelationships. The gross properties of a large number of line profiles fitted with a single Gaussian were obtained. By examining the interrelationships between the quantities,

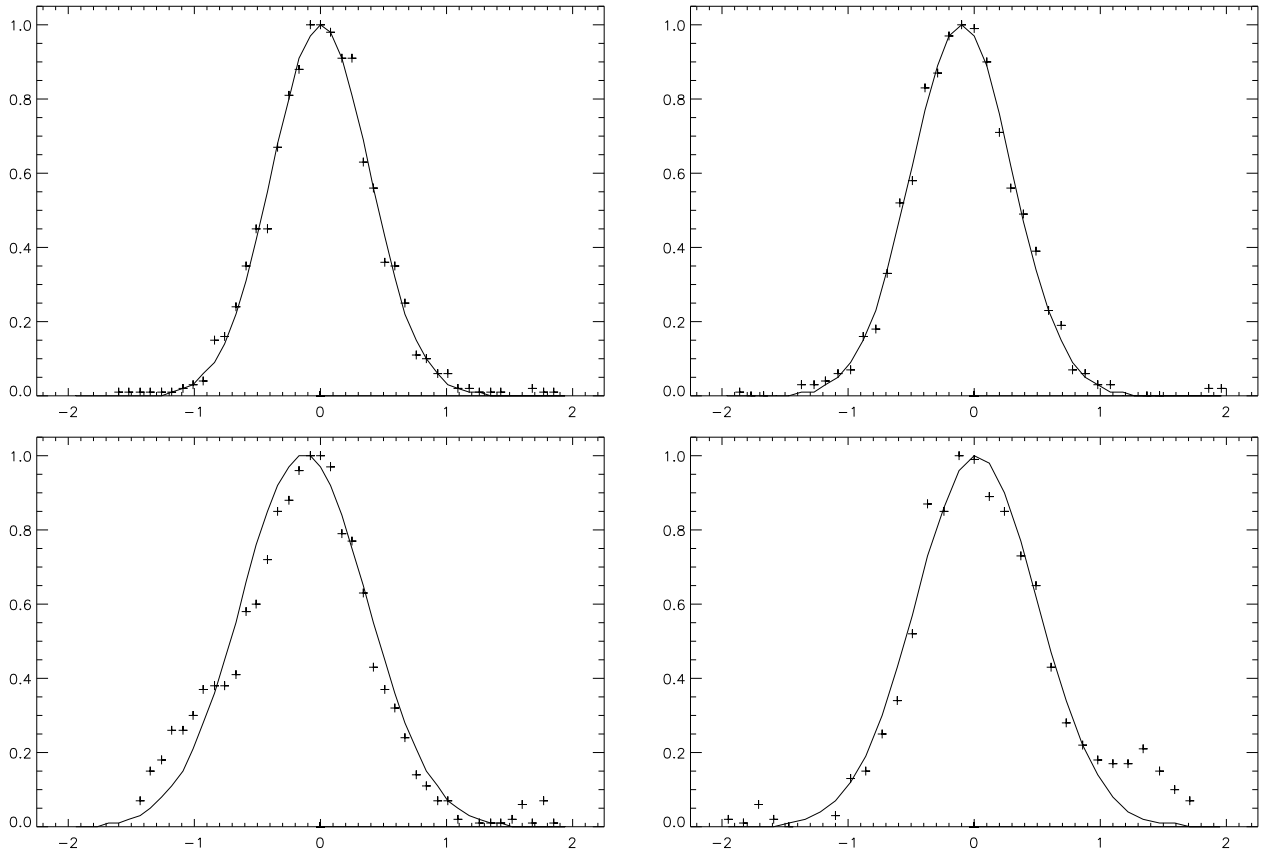

Figure 3.5: Example of line profiles fitted with Gaussian curves. The upper two line profiles represent single components profiles and the lower two represent blueshifted (left) and redshifted (right) line profiles.

Table 3.4: Table showing the number of line profiles observed in different ranges of asymmetry.

Type	Asymmetry range (Å)	Number of profiles	Total
Single	-0.08 to 0.08	439	34%
Blueshifts	-0.08 to -0.2	428	
	-0.2 to -0.3	237	
	-0.3 to -0.6	96	59%
Redshifts	0.08 to 0.2	76	
	0.2 to 0.3	19	7%

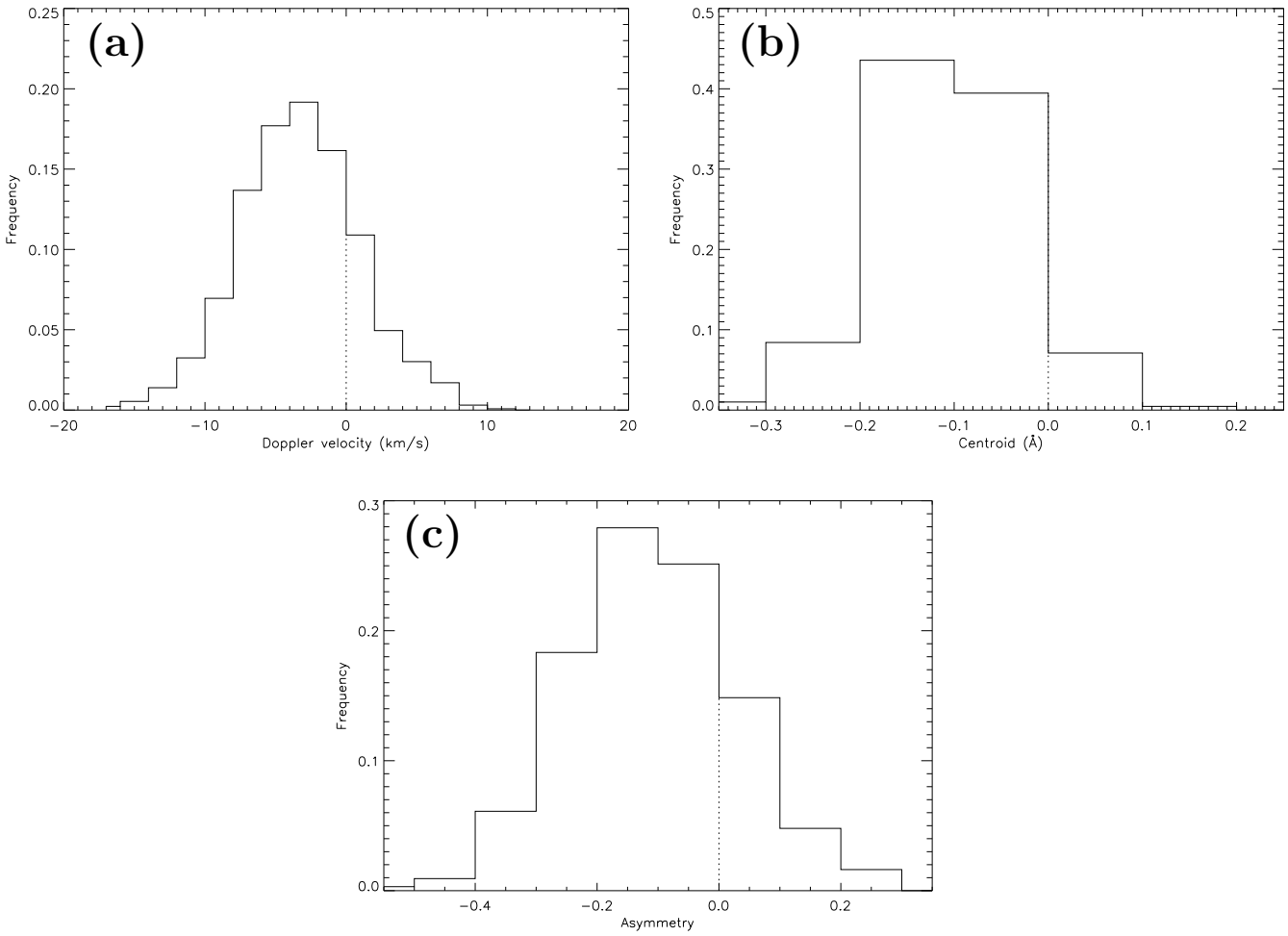

Figure 3.6: Normalized histograms of (a) Doppler velocity, (b) Centroid, and (c) Asymmetry.

we expect to get information on the nature of the multicomponents without actually going for the complex multiple Gaussian fitting. In Raju, Chandrasekhar, and Ashok 2011b, line profiles were obtained from a single interferogram and the nature of the secondary component, obtained by subtracting the red wing from the blue, was studied in detail. In M. Prabhakar, Raju, and Chandrasekhar 2013, the study is primarily on the asymmetry of the multiple components.

It can be seen that the line profiles with the greatest asymmetry are found in the blue wing (96 line profiles). Thus, our results agree well with the works by Raju, Desai, et al. 1993, Raju 1999, Dadashi, Teriaca, and Solanki 2011, Chae, Yun, and A. I. Poland 1998a and Peter and Judge 1999 regarding the presence of the multicomponents and dominance of the blueshifts, but the percentage is found to be on the higher side. The redshifts are seen to be very less with just a 7 % contribution.

The normalized histograms of Doppler velocity, centroid and asymmetry of the line profiles can be seen in Figure 3.6. It can be seen that all of them show the domination of the blueshifts which does not agree with S. W. McIntosh et al. 2012, which reports a weak emission component in the blue wing that contributes a very less percentage of the emission line profiles. The multi-components with blueshifts are found to have a maximum Doppler velocity of -18 km s^{-1} and those with redshifts

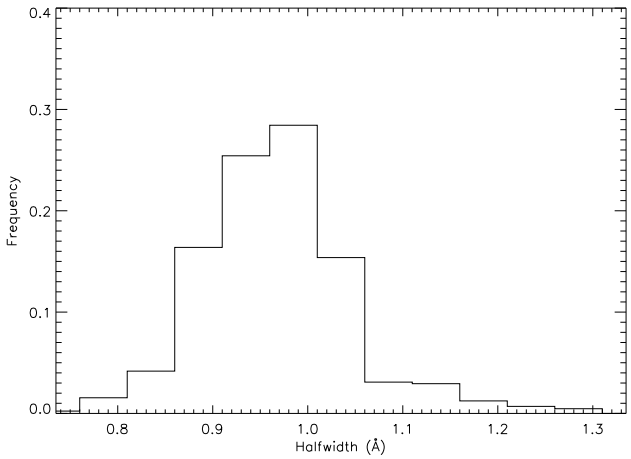

Figure 3.7: Normalized histogram of halfwidth of the line profiles.

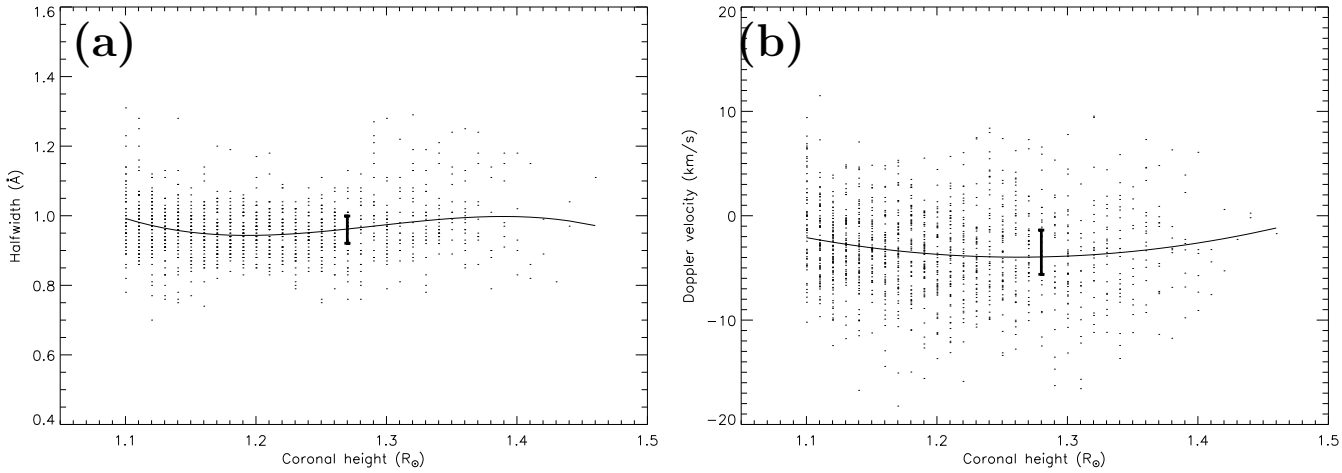

Figure 3.8: (a) Variation of the halfwidth and (b) Doppler velocity with height above the limb. The solid line shows the best-fit polynomial. The error bar indicates the standard error in the fittings.

Table 3.5: Table showing values of R, R^2 and standard errors for the plots in Figures in 5 and 6 for linear, quadratic and cubic fittings.

Figure	Linear			Quadratic			Cubic		
	R	R^2	Std er	R	R^2	Std er	R	R^2	Std er
Figure 8a	0.05	0.0025	0.07	0.18	0.031	0.078	0.21	0.044	0.078
Figure 8b	-0.08	0.0068	4.26	0.14	0.018	4.23	0.14	0.021	4.23
Figure 9a	0.03	0.0008	0.079	0.23	0.051	0.077	0.22	0.048	0.077
Figure 9b	0.02	0.0004	0.079	0.21	0.045	0.078	0.21	0.045	0.078
Figure 9c	0.12	0.015	0.079	0.12	0.014	0.079	0.12	0.015	0.079

are found to have a maximum Doppler velocity of 11 km s^{-1}. It is to be noted that these values are from the composite line profiles and when the Gaussian decomposition is performed, velocities of the secondary components are much larger (Raju, Chandrasekhar, and Ashok 2011b).

The normalized histogram of the halfwidth can be seen in Figure 3.7. It can be seen that the halfwidth fall in the range 0.7-1.3 Å and peak at 0.96 Å. This would correspond to a temperature of 3.8 MK. Considering the non-thermal broadening that could add to the line width, and the line formation temperature as 2 MK, we find that the non-thermal velocity is close to 22 km s^{-1} (Raju, Chandrasekhar, and Ashok 2011b) from the following relation:

$$\frac{2kT_0}{M} = \frac{2kT_D}{M} + v_t^2$$

where k is the Boltzmann constant, T_0 is the observed line width temperature, M is the mass of the emitting ion, T_D is the line width Doppler temperature and v_t is the non-thermal velocity characterizing microturbulence.

Further, we studied the variation of the halfwidth and Doppler velocity of the line profiles with respect to their heights from the solar centre. In Figure 3.8a, we have plotted halfwidth against the coronal height. We have tried linear, quadratic and cubic polynomial fits and a detailed statistical analysis was performed. The details are given in Table 3.5. The different columns in the table give the values of correlation coefficient (R), coefficient of determination (R^2), and the standard error in the fittings. It can be seen from the table that the best fit is obtained from the cubic polynomial fit where the value of R=0.21 and R^2=4.4%. The best-fit polynomial and the standard error are plotted in the figure. It can be seen that the total variation is comparable to the standard error in the fitting and hence the trend is insignificant.

This result is unlike what is observed in Mierla et al. 2008, which states that the width remains almost constant or increases up to a height of 1.3 $R_\odot$. It is also different from what is seen in Prasad, Singh, and Banerjee 2013 and Beck et al. 2016, which report a decrease in the line widths with the

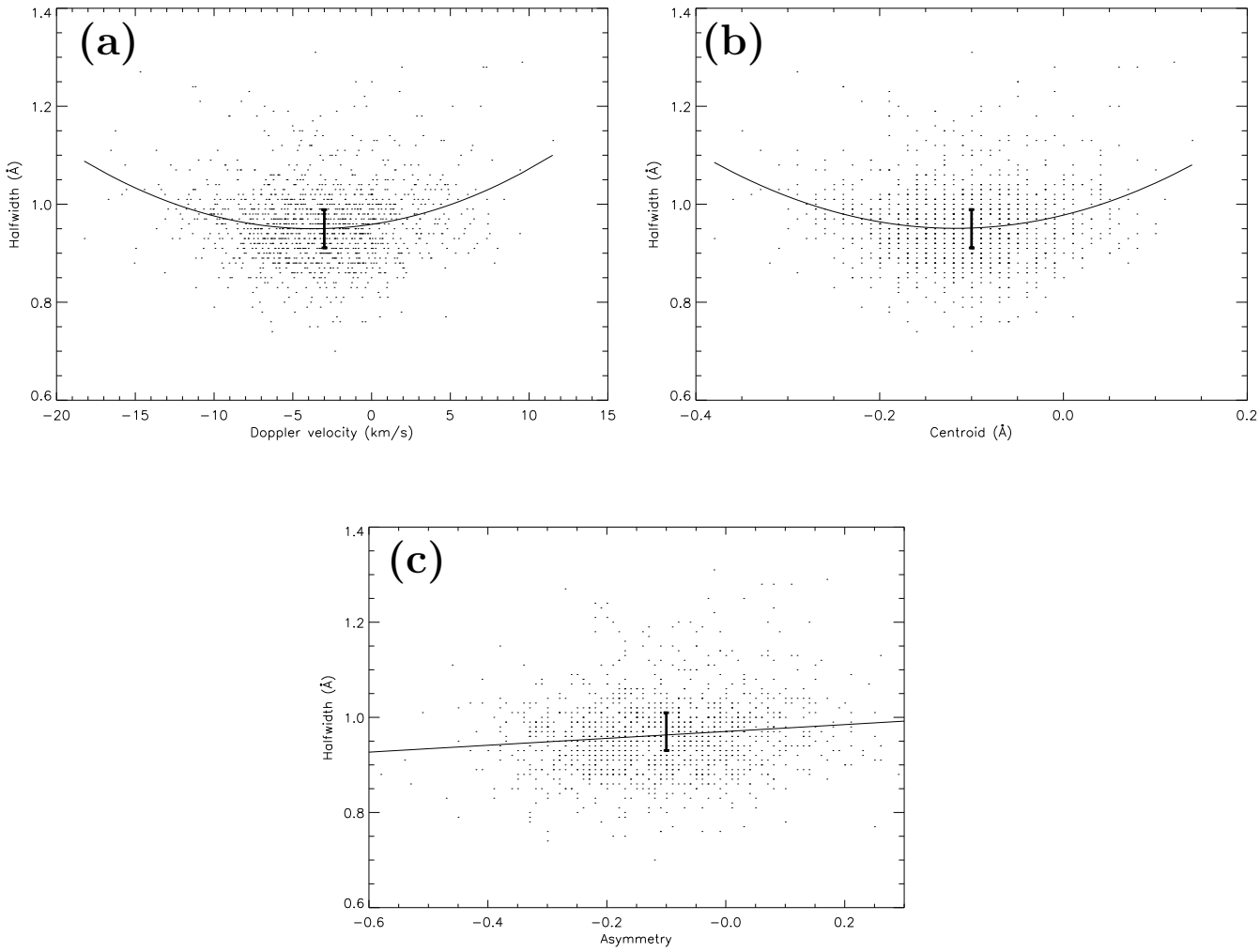

Figure 3.9: (a) Variation of the Doppler velocity (b) Centroid, and (c) Asymmetry of the line profiles with halfwidth. The solid line shows the best fit polynomial. The error bar indicates the standard error in the fittings.

height of the line profiles.

Figure 3.8b shows the variation of the Doppler velocity of the line profiles with coronal height. It can be seen from Table 3.5 that the coefficients R and R^2 do not show much improvement from quadratic to cubic fits. So, a quadratic fit is considered for this plot. Here the total variation is less than the standard error and hence insignificant.

We further studied the variation of halfwidth of the line profiles with Doppler velocity and centroid which are shown in Figure 3.9a and b. From Table 3.5, it is evident that the quadratic fit is better than the linear fit where the coefficients show a marked improvement. There is no marked improvement in the cubic fit. The total variation is almost twice the standard error and hence these fits are retained. The correlation coefficients are 0.23 and 0.21 respectively which means a mild correlation. The R^2 values which give the percentage of explained variation are about 5%. This implies that the relationship between halfwidth and Doppler velocity or centroid is weak. A variation like this is observed in Bryans, P. R. Young, and G. A. Doschek 2010 for the active region AR 10978. Raju,

Chandrasekhar, and Ashok 2011b examined the relationship between halfwidth and Doppler velocity from two cases with a limited number of samples and a positive angle coverage of 20°. They report a weak correlation in one case and a lack of correlation in the other. Therefore, it may be concluded that the weak correlation found between the halfwidth and Doppler velocity or centroid could be real. Peter 2010a reports that the positive correlation between these quantities suggests a flow associated with a heating process.

Variation of the halfwidth with respect to the asymmetry of the line profiles is given in Figure 3.9c. Here the quadratic or cubic fit does not improve the linear fit. The coefficients R, R^2 and standard error remain almost constant in all three cases. The linear trend is comparable to the standard error and is not significant. This is found very different when compared to the variation of Doppler velocity and centroid with the halfwidth.

3.7 Conclusions

We studied various characteristics of the inner solar corona by analyzing the line profiles obtained from the analysis of the Fabry-Perot interferograms. We found that a majority of these line profiles comprise of multicomponents, with a higher contribution from the blueshifts (59 %). This was followed by the single component profiles, which constituted 34 %. The redshifts were found very less with just 7 %. This result, though found to be in agreement with the related works reported earlier, shows a very high percentage of blueshifts. Line profiles showing the greatest asymmetry were found to be blueshifted and they constituted close to 7.5% of the observed line profiles. The multiple component profiles with blueshifts were found to have a maximum Doppler velocity of -18 km s^{-1} and the redshifted multicomponents were found to have a maximum Doppler velocity of 11 km s^{-1}. These values specify the Doppler velocity of the composite profile and the actual values of the Doppler velocity of the components could be much higher. The excess blueshifts could be related to the type-II spicules or the nascent solar wind flow. Further, the variation of halfwidth and Doppler velocity with respect to the coronal height are found to be insignificant. The variation of halfwidth with respect to the Doppler velocity or centroid shows a parabolic trend with a weak correlation. The positive correlation is important as it suggests a flow associated with a heating process. We have compared the results with line profile simulations and there is generally a good agreement except when the Doppler velocities are high.

The basic problem posed by the discovery of the coronal temperature is to find the mechanism responsible for heating its layers by non-thermal energy transport. Many theories like nanoflare heating, type-II spicules, magnetic reconnection, Alfven waves etc, are proposed to cause coronal heating. Our results give inputs to coronal heating and dynamics. The trend between halfwidth and asymmetry is inconclusive and needs to be examined further.

Chapter 4

Studies of the Coronal Active Regions in FeXII λ195.12 using Hinode/EIS

4.1 Introduction

4.1.1 An Overview of Space-based Solar Coronal Studies

In this chapter[1], the line profile studies of the coronal active regions using the Hinode/Extreme ultraviolet Imaging Spectrometer (EIS) data are discussed. This is based on the paper Maya Prabhakar and Raju 2022.

The journey of space astronomy started in 1946 in the United States with W. Von Braun's A4 rocket engines which were made available to scientists. This facilitated the launching of free-flying, high-altitude observatories carrying spectrometers, imagers, coronagraphs or even in-situ instruments that were initially used for the detection of charged particles over a wide energy range. Since then, a lot of progress has been made in solar and stellar observational studies from space. Radio, infrared and optical wavelength ranges are the domain of ground-based observatories. Enormous progress has also been made in this area and new technologies are available to overcome atmospheric problems. Space-based instruments complement other ground-based contributions.

New regimes became available due to observations done from space in varied wavelengths. Numerous EUV and X-ray instruments along with in-situ instruments were used for particle detection (Curdt 2003). This set of highly successful major instruments includes the Orbiting Solar Observatory (OSO), Skylab, Helios 1&2, Solar Maximum Mission, Hinotori, Coronas-I, and the highly successful Yohkoh mission (Antiochos et al. 1997).

The Ulysses (1990-2009) is one of the major solar project that encompasses studies of the heliospheric magnetic field, heliospheric radio and plasma waves, the solar wind plasma, solar and interplanetary energetic particles and cosmic rays (Reames, Richardson, and Wenzel 1992). It also carries radio science instruments to probe the solar corona and instruments to study cosmic dust,

[1]This chapter presents the work published in Maya Prabhakar & K.P Raju, 2022, The Astrophysical Journal, Volume 931, 40

interstellar neutral gas, and gravitational waves. The SOlar and Heliospheric Observatory (SOHO) of European Space Agency (ESA) and NASA is another major project that carries coronal instruments as well as an in-situ package (Domingo, Fleck, and Arthur I Poland 1995).SOHO includes three hioseismology instruments Michelson Doppler Imager (MDI)-Solar Oscillations Investigation (SOI) and Global Oscillations at Low Frequency (GOLF), EUV and Vacuum Ultraviolet (VUV) spectrometers (Coronal Diagnostic Spectrometer (CDS), Solar Ultraviolet Measurement of Emitted Radiation (SUMER)), a EUV full-disk imager (Extreme ultraviolet Imaging Telescope), a magnetic imager (MDI), white-light and VUV coronagraphs (Large Angle Spectroscopic Coronagraph (LASCO), UltraViolet Coronagraph Spectrometer (UVCS)), the Solar Wind Anisotropies (SWAN) hydrogen absorption cell instrument, the VIRGO global-Sun radiometer, and the in-situ particle instruments Charge, Element, and Isotope Analysis System (CELIAS), Comprehensive Suprathermal and Energetic Particle Analyzer (COSTEP) and Energetic and Relativistic Nuclei and Electron experiment (ERNE). SOHO orbits around the first Lagrangian point L1, and, in constant view of the Sun, returns data since 1996 with a short interruption in 1998.

Next was the era of TRACE (1998-2010), a NASA SMEX (SMallEXplorer) mission for high-resolution imaging of the upper solar atmosphere which was launched into an Sun-synchronous polar orbit in April 1998. Further, NASA's Advanced Composition Explorer, ACE, orbiting the first Lagrangian point L1 since 1997, started continuously probing for accelerated particles over a wide energy range, arriving not only from the Sun, but also from interstellar and galactic sources. The Russian Coronas-F is another project in the list with on-board instruments for studies in the UV, X-ray, gamma and radio emission of the active or flaring Sun. The High Energy Spectroscopic Imager, RHESSI, a NASA SMEX mission, is important in the detection of particle acceleration.

Yohkoh (1991-2001) (also known as Solar-A) was a Japanese-led spacecraft from the Institute of Space and Astronautical Science, the former name of Japan's space agency. The Earth-orbiting spacecraft imaged the Sun in X-rays and with spectrometry. Some of its discoveries included showing that solar flares are "magnetic reconnection phenomena" caused by events in the Sun's magnetic field and that the solar corona can change its scale dynamically.

Japan's Hinode satellite (also known as Solar-B) focuses on the solar corona, the extremely hot upper atmosphere of the Sun. The mission aims for "an improved understanding of the mechanisms of solar explosions, which will in turn greatly help us predict how solar events affect Earth,"

As we know, the solar corona is dominated by a variety of structures, such as active regions, coronal loops, bright points, coronal holes, etc. The heating of the coronal plasma to millions of degrees, the acceleration of the solar wind, and the reasons behind the dynamic solar atmosphere are not fully explained. There is a need for understanding the physical connection between the mass motions in the solar atmosphere and the coronal heating and possibly the solar wind. Hence, the nature of mass transport mechanisms in the solar atmosphere plays a key role in addressing this connection. Based on our studies on the solar coronal line profiles from the ground-based eclipse observations, we extend our work to space-based Hinode/EIS data. Here we discuss our work on the coronal active regions' line profile studies.

4.1.2 Major Solar Coronal Line Profile Studies so Far

Many attempts were made to address the above problems by studying the 1) the flows into the upper solar atmosphere from the lower solar atmosphere, 2) the mass motions and their magnetohydrodynamics in the corona, and 3) the possible connection between the convection and the dynamics of atmospheric regions. The line profile analysis is one such tool that gives parameters like the intensity, line width, Doppler velocity, and centroid, which provide information on the physical conditions such as density, temperature, mass motions, etc. Several interesting results were obtained from such analyses.

Firstly, many kinds of shifts were observed in different regions in different lines. Raju, Desai, et al. 1993 reported excess blueshifts in the coronal line profiles. The emission lines observed in the quiet transition regions were reported to be redshifted (Brekke et al. 2000; Peter and Judge 1999). The existence of a highly dynamic corona was established in the late 1990s after the Solar and Heliospheric Observatory (SOHO) and Transition Region And Coronal Explorer (TRACE) observations (Brekke et al. 2000). Further, blueshifts were also reported by Peter and Judge 1999 in three coronal lines. All these observations point to the mass motions present in the coronal heights whose emission lines are Doppler shifted. The asymmetry caused in the spectral lines were correlated with the coronal heating. Smaller mass motions driven from chromospheric regions can contribute to the hot plasma in the corona as well. Nanoflares are the other known sources of hot plasma in the coronal heights. Chromospheric or the type II spicules (Beckers 1968; B. De Pontieu, S. W. McIntosh, et al. 2009), magnetic reconnection (James A. Klimchuk 2006; Parnell and De Moortel 2012), and dissipation of the Alfven waves and magnetoacoustic shocks on magnetic flux concentrations (B. De Pontieu, Hansteen, et al. 2007; Bart De Pontieu, Erdélyi, and James 2004) have been shown to contribute significantly to the coronal heating and/or solar wind acceleration.

In recent years, several authors have reported the blueshifts, and these are interpreted in terms of nascent solar wind flow. Tian, Tu, et al. 2010 observed signatures of nascent solar wind in a polar coronal hole with some significant blueshifts. Similarly, nanoflare heating was linked with solar wind by Patsourakos and J. A. Klimchuk 2006 and type II spicules by B. De Pontieu, S. W. McIntosh, et al. 2009.

Blueshifts were considered to be signatures of slow solar wind sources by Hara et al. 2008 and David H. Brooks, Warren, and Peter R. Young 2011 as well. S. W. McIntosh et al. 2012, who conducted studies using a combination of Hinode/Extreme ultraviolet Imaging Spectrometer (EIS) emission-line spectra and image sequences from the Solar Dynamics Observatory/Atmospheric Imaging Assembly, also report the line profile asymmetry and complexities involved in the coronal emissions at temperatures below $\approx$1 MK. Episodic heating events that are rooted in the chromosphere can play a significant role in filling the Sun's upper atmosphere with hot plasma (B. De Pontieu, S. W. McIntosh, et al. 2009; Scott W. McIntosh, de Pontieu, and Leamon 2010). Tian, Louise Harra, et al. 2021 talk about pervasive upflows which are considered to be linked with the solar wind upflows, and to contribute to the coronal hot plasma.

Further, the coronal lines are known to have nonthermal line widths along with the expected thermal line widths (Chae, Yun, and A. I. Poland 1998b; Delone and Makarova 1969, 1975). Excess line widths of the order of 15 – 20 km s^{-1} were reported by Skylab and Solar Maximum Mission in the coronal forbidden lines. They are explained as indications of wave propagation causing coronal heating (Hollweg 1978; Parker 1988). Variation of these line widths above the limb with height has been reported differently by different instruments. The correlation between the Doppler velocity and the line width suggests that the outflows are composed of multiple components. Correlation between the Doppler velocity and the line width is also seen in coronal green line profiles from active regions (Raju, Chandrasekhar, and Ashok 2011a).

The coronal active regions are the source of many large-scale eruptions, including the coronal mass ejections and the solar flares. These regions are also found to be present around the solar prominences in many cases. Active regions are found to peak during the maxima of the Sunspot cycle. These bright regions appear prominently in X-ray and ultraviolet images of the Sun. Large outflows at the boundaries of the active regions have been discovered from Hinode/EIS observations in recent years (David H. Brooks, Warren, and Peter R. Young 2011; G. A. Doschek et al. 2008; Hara et al. 2008; Sakao et al. 2007). Studies of the fast upflows (≈100 km s^{-1}) in the coronal active regions have shown asymmetry in the hot spectral lines. Tripathi and James A. Klimchuk 2013 state that type II spicules or any such mass motions that cause instant heating and chromospheric evaporation do not contribute dominant plasma any greater than 0.6 MK to cause coronal heating. The series of tests that were carried out by J. A. Klimchuk 2012 to examine the role of plasma from type II spicules in the coronal heating also showed that spicules do not provide high-temperature plasma to the corona but may provide cooler plasma that may get further heated in the coronal altitudes. Recent observations by Macneil et al. 2019, David H. Brooks, Louise Harra, et al. 2021, Yardley, D. H. Brooks, and Baker 2021, and L. Harra et al. 2021 also report flows in the active region boundaries.

So keeping in mind the asymmetry seen in the coronal regions dominated by the blueshifts, their possible connections with the solar coronal heating, and the acceleration with the solar wind, we present our study on the line width variation in various coronal active regions and its possible interdependency with other parameters during the solar cycle. We also report other results found in the course of study of the line profile analysis. The high spatial and spectral resolution of Hinode/EIS (Kosugi et al. 2007) enables us to study the solar corona in great detail. We have studied how the line profiles vary in different active regions for a period of 13 yr from 2006 December to 2019 December. This period covers the last 2 yr of the solar cycle 23 and the solar cycle 24 fully. The aim of this work is to study the coronal active regions using the emission-line profiles. In our earlier work (Maya Prabhakar, Raju, and Chandrasekhar 2019) we found some correlation of the line width with the Doppler velocity and the centroid. This is from the ground-based eclipse observations that lasted for just for 3 minutes and 37 s. Hinode also provides a great opportunity to study the long-term behavior of the corona. So we have used about 13 yr of the data to study the solar cycle variation of line profile parameters.

Figure 4.1: Artist's illustration of the Hinode spacecraft in the Earth orbit with its solar panels completely extended. Courtesy NASA.

In the following sections, we present the instrumentation details of Hinode and EIS followed by observations, data and analysis. Further, we present the results, where we talk about the behaviour of the line profile parameters, their interrelations, and the correlations between the parameters and the solar cycle followed by the discussions. Lastly, we present our conclusions.

4.2 Hinode

The Hinode spacecraft was launched from Uchinoura Space Center in Japan (Kosugi et al. 2008). It was launched on a Japanese M-V rocket out of Kagoshima, Japan, on September 23, 2006. An illustration of this spacecraft can be seen in Figure 4.1. It is led by the Japan Aerospace Exploration Agency or JAXA. It also involves other space agencies like the United States's NASA, the United Kingdom's STFC and Europe's ESA. Hinode was designed to probe into the Sun's magnetic field to better understand the origin of solar disturbances that interfere with satellite communications, electrical power transmission grids and the safety of astronauts traveling beyond Earth's magnetic field.

This is an international mission to study our nearest star, the Sun. Hinode explores the magnetic fields of the Sun in order to improve understanding of what powers the solar atmosphere and drives solar eruptions. There are three instruments onboard Hinode meant for different wavelength studies of the Sun. Hinode's Solar Optical Telescope (SOT) is the first space-borne instrument to measure the strength and direction of the Sun's magnetic field on the Sun's surface, the photosphere. Combined with two other Hinode instruments, the EUV imaging spectrometer, or EIS, and the X-

ray/EUV telescope, or XRT, the mission is designed to understand the causes of eruptions in the solar atmosphere and relate those eruptions to the intense heating of the corona and the mechanisms that drive the constant outflow of solar radiation, the solar wind. NASA's Marshall Space Flight Center managed the development of the spacecraft's all three science instruments.

Hinode follows a Sun-synchronous orbit around Earth at an altitude around 650 km. Its orbit allows Hinode to observe the Sun continuously for nine months at a time. During the summer (in the northern hemisphere), Hinode experiences an "eclipse season" during which the Sun is eclipsed by Earth for a maximum of ten minutes in each 98-minute orbit. Hinode is expected to continue into 2022 after being extended in 2020. Some major results achieved from Hinode instruments collectively can be seen in Team et al. 2019.

4.2.1 Extreme ultraviolet Imaging Spectrometer

The EIS (Culhane et al. 2007) was designed to observe and understand many of the physical processes that occur in the solar corona and upper transition region. Its primary science objectives include understanding coronal heating, the onset of coronal mass ejections and flares, and the origin of the solar wind. The EIS design represents a significant advance in spatial resolution, effective area, and temperature coverage over many previous spectrometers. Here we give a brief overview of the EIS observations.

EIS observations

EIS observes emission lines in the wavelength ranges 170–210 Å and 250–290Å. The range of emission lines available provides density diagnostics, first ionization potential (FIP) effect measurements, Doppler velocities, line widths, and emission measure distributions. Telemetry constraints, however, often limit the number of spectral windows that can be returned during an observation. Line selection details can be seen in Peter R. Young et al. 2007. Information on the high-temperature lines observed in active regions (e.g., Ca XIV —Ca XVII, Fe XVII) and flares (e.g., Fe XXII —Fe XIV) was provided in Watanabe et al. 2007 and Warren, Ugarte-Urra, George A. Doschek, et al. 2008.

EIS has four slit/slot options that allow for different modes of observing: "sit-and-stare" provides excellent time resolution at a single spatial location and, at the other extreme, "rastering" provides detailed scans over large portions of the Sun. Figure 4.2 illustrates an EIS active region raster.

The sensitivity of the EIS instrument to incoming solar radiation depends on a number of factors, including the geometrical area of the optical elements, the reflectivities of the multi-layer coatings, and the quantum efficiency of the detectors. The pre-flight properties of the instrument were described in Lang et al. 2006 and EIS Software Notes. The initial on-orbit performance was described in J. T. Mariska 2013. Subsequent analysis has indicated that there have been wavelength-dependent changes in the calibration over time (Warren, Ugarte-Urra, and Landi 2014).

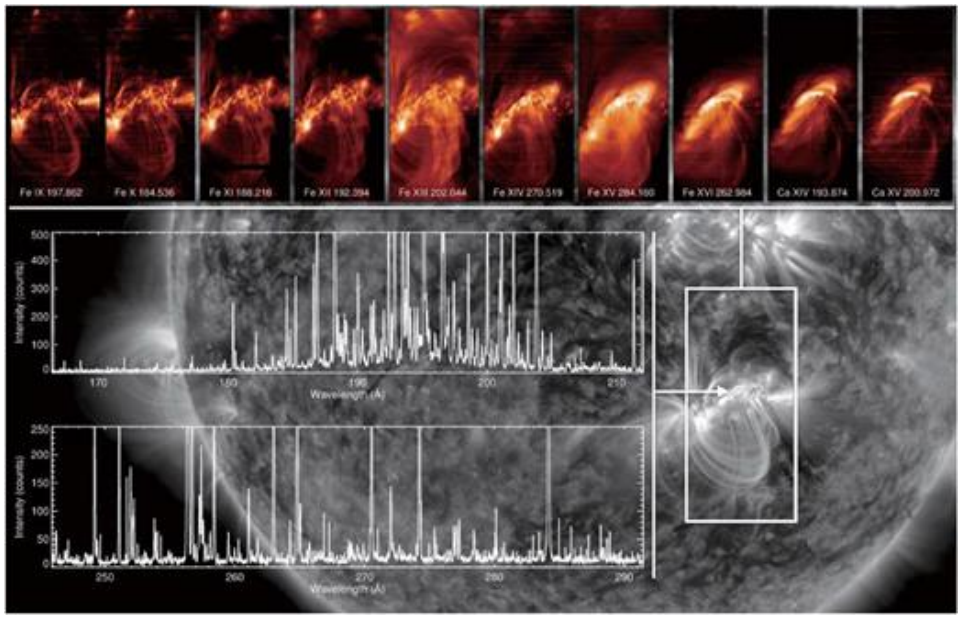

Figure 4.2: Example EIS active region observations. The top panels show scans across the active regions in individual emission lines from Fe IX (logT = 5.9) to Ca XV (logT = 6.65). It shows how the solar corona changes dramatically as a function of temperature. The bottom panels show the full EIS spectral range from a single point in the core of the active region. The background image is from SDO/AIA in 171Å. These observations were taken on 2015 December 29 by Team et al. 2019.

Wavelength calibration

EIS does not have a wavelength calibration lamp. It has no access to photospheric lines that can be used as wavelength calibrators. Therefore, the wavelength calibration requires some assumptions like the average velocity in the data set is zero. These methods have a fundamental uncertainty of about ±5 km s^{-1} (P. R. Young, O'Dwyer, and Mason 2012), but relative wavelength measurements between repeated exposures can be precise to 0.5 km s^{-1} or better (John T. Mariska and Muglach 2010).

The dispersion formulae for the EIS bands are described by quadratic functions. The method was described by Brown et al. 2007 although we note that the parameters in this work have subsequently been updated.

Line width calibration

The instrumental widths of the narrow EIS slits, expressed as the FWHM of a Gaussian function, are returned by the IDL routine EIS_SLIT_WIDTH. The widths vary as a function of the Y-position along the EIS CCDs, with minimum values of 56 and 64 mÅfor the 1′ and 2′ slits near Y-pixel 300, and maximum values of 78 and 83 mÅat the top of the detector. The widths were measured from spectra of Fe XII 193.51 Å obtained above the quiet-Sun limb at the equator. The line was assumed to be broadened only by instrumental and thermal processes. More details can be found in EIS Software Notes.

Spatial resolution

The spatial resolution of EIS was measured pre-flight using EUV emission from a discharge lamp (Korendyke et al. 2006) and characterized as 2″. The on-orbit performance was described in EIS Software Note and indicated that the spatial resolution is approximately 3″. The analysis determined this value from 1) the FWHM of point-like features in selected data sets and 2) comparisons of slit and slot rasters in the 195.119 Å line with simultaneous 193Å narrow-band images from the high-resolution (0.6″) SDO/AIA. A scientific study of the observed cross-field size of coronal loops (David H. Brooks, Warren, and Ugarte-Urra 2012) also found consistent AIA–EIS results with an EIS PSF of 2.5″.

Pointing accuracy

EIS points to a position on the Sun by combining the planned Hinode spacecraft pointing with an internal pointing system that moves the EIS mirror in small steps. How accurately EIS can point to a specified solar location has been evaluated by regularly co-aligning EIS Fe XII 195Å slot spectroheliograms with simultaneous AIA 193 Å images. These observations show that in a yearly cycle, the EIS solar coordinates vary from true solar coordinates in a predictable manner by about 25″ in X and 50″ in Y. These long-term variations have been accounted for in the EIS planning and analysis software. It is possible to determine the location of the EIS slit on the Sun to be better than 5″ in both X and Y. EIS Software Notes provides additional details.

Once EIS has pointed at a fixed position on the Sun, the actual location will fluctuate due to spacecraft pointing variations and thermal fluctuations around the orbit. Only limited analysis has been performed to determine the extent of these changes. Analyses of co-aligned EIS slot images obtained over a one-day period showed regular fluctuations in EIS pointing on orbital time scales and more random variations over several hours. Over an orbit, a fixed EIS slit or slot position on the Sun fluctuates by up to 2″ in X and 4″ in Y. Over a day, a fixed EIS pointing can vary by up to 6″ in X and 10″ in Y. EIS Software Notes provides a preliminary analysis of these pointing variations.

Warm and hot pixels

The CCDs on EIS have performed exceptionally well, with tests demonstrating that they are clean and do not require decontamination. However, the CCDs have developed an increasing number of hot and warm pixels since launch. The hot pixels were caused by radiation damage and appear as pixels with the energy of mean value $> 50\sigma$ of the noise level σ. In addition, there are warm pixels that have mean values between 5σ and 50σ. These have been tracked since launch, and warm and hot pixel maps are provided that allow them to be dealt with within the calibration. However, at the end of 2015, the number of these damaged pixels reached a level close to impacting science, so a bakeout plan was developed and carried out. The first bakeout took place in 2016 February for three days and resulted in a reduction in the hot pixels by 67% and a reduction in the warm pixels by 9%.

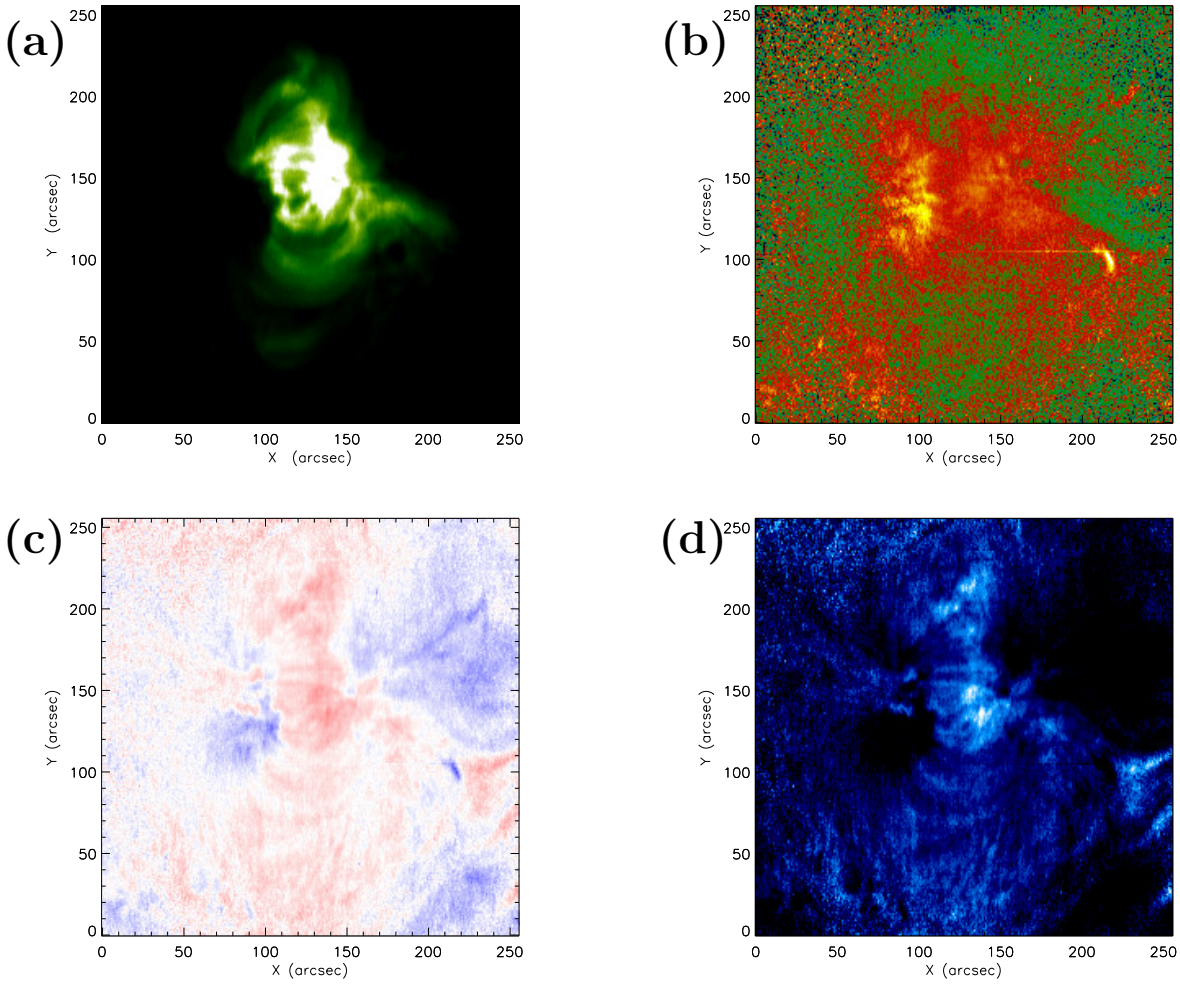

Figure 4.3: Maps of a typical 1″ raster-scanned active region's (a) intensity, (b) line width, (c) Doppler velocity and (d) centroid observed on 2007-10-01T00:19:13Z respectively having solar center coordinates

Since the middle of 2016, a new regime of higher telemetry became available to EIS. Regular observing increased the telemetry allocation from 15% to 23%, and in circumstances where we require more for an additional science mode, this can be requested. This allows users to choose more spectral lines or to use a higher time cadence and larger field-of-view (FOV).

4.3 Data and Analysis

The Hinode mission provides sequential data unaffected by the day and night cycles for studying the progression of particular events. The EIS on board Hinode generates spectra in the wavelength bands centred at 195 and 270 Å having a bandwidth of 40 Å. EIS images the Sun in 1″ and 2″ slits to produce line profiles and uses 40″ and 266″ slits to produce monochromatic images. EIS slits can be used to raster-scan required regions to generate spectroheliograms, as well as in sit-and-stare mode to observe regions for repeated exposures to produce high-cadence images (Culhane et al. 2007).

In our study, we have considered the coronal active region data sets from Hinode/EIS in the EUV line Fe XII λ195.12. It is a strong emission line that ranges between 194.84 and 195.36 Å and is formed at a relatively low temperature of 1.25 MK. One data set is considered for every month starting from 2006 October, when the instrument was launched, until 2019 December. However, we found that for the months of 2006 October and November, the data quality is very poor with **missing pixels**. We obtained good-quality data sets from 2006 December onward. There are no data sets available for 3 months from 2018 February to April, when the EIS instrument turned off unexpectedly; it was turned back on in 2018 May. We have mostly considered the first available raster scan data of active regions in every month. In case of nonavailability of raster scans, a few sit-and-stare data are considered. In total, there are 154 data sets, out of which 5 of them are sit-and-stare images. This include 47 1″ raster scans, 102 2″ raster scans, 4 1″ sit-and-stare data and one 2″ sit-and-stare data.

The data sets are analyzed using EIS routines (**EIS software notes**). The prepping of the data was done using the **eis_prep** routine on IDL. This routine removes the pedestal and dark currents, electron spikes and hot pixels, and calibrates the data generating level 1 FITS files. These level 1 fits data are further fitted with Gaussian curves using the eis_auto_fit routine, which automatically handles the wavelength correction as well. It should be noted that the line width values are also corrected for the instrumental profile. We have fitted the data with a single Gaussian for our study using the above-mentioned routine. (However, it can also be used to fit double-Gaussian curves.) This gives the intensity versus wavelength (line profile) for every point of the data set. The peak intensity, Doppler velocity, half-width, and centroid are extracted from the line profiles. The data are composed of the active regions observed on both the limb and the disk. Figure 4.3 (a), (b), (c), and (d) give an example of the intensity, line width, Doppler velocity, and centroid maps for a typical data set observed on 2007-10-01T00:19:13Z, respectively.

4.4 Results

The parameters obtained from Gaussian fitting have certain interesting features. The line profile simulation that explains the behaviour of the Doppler velocity and the centroid with respect to the line width is shown in Chapter-2. In continuation to this, here we mention the features of the parameters by analyzing their histograms in Section 4.4.1. We found that the line width has a significant correlation with the Doppler velocity and the centroid, which we describe in Section 4.4.2. Lastly, to get an overview of how these parameters behave during a solar cycle, we address these parameters' correlation with the Sunspot number in Section 4.4.3.

4.4.1 Histogram Analysis

We report the behaviour of histograms of the intensity, Doppler velocity, line width, and centroid of all the data sets in this section. Based on the shift in the Doppler velocity and the centroid, we have classified the data into six different cases. For each case, we have provided a typical example of the

histograms. The intensity and the line width histograms are given for the sake of completeness.

Case 1—Doppler velocity and centroid centered at the rest wavelength

In this case, Doppler velocity and centroid are both centered at the rest wavelength. When the shifts are found within the error limits, such data sets are put under this category. The intensity and the line width histograms are skewed toward the higher values. We have observed 38 data sets under this category, which composes of 24.6% of all the data sets analyzed. The one observed on 2007-04-01T06:12:21Z is shown in Figure 4.4.

Case 2—Doppler velocity and centroid both centered in the blue wing

Here, both the Doppler velocity and the centroid histograms are shifted to the blue wing (Figure 4.5). The Doppler velocity ranges between -32 and 0 km s^{-1} and peaks around -14 km s^{-1}. The centroid ranges between -30 and 0 km s^{-1} and peaks around -13 km s^{-1}. The intensity distribution is highly skewed, whereas the width distribution is almost symmetric. We have observed only one data set under this category that is observed on 2017-04-02T02:15:13Z.

Case 3—Doppler velocity and centroid both shifted to the red wing

This is complementary to Case 2, where both the Doppler velocity and the centroid histograms are shifted to the red wing. We have observed only two data sets under this category; of which the one observed on 2008-06-01T09:50:26Z is shown in Figure 4.6. The Doppler velocity ranges between -3 and 18 km s^{-1} with a peak at 6 km s^{-1}. The centroid ranges between -4 and 17.5 km s^{-1} with a peak at 5.5 km s^{-1}. The figure also shows an intensity histogram with multi components and a line width histogram that is skewed toward lower values.

Case 4—Doppler velocity centered at the rest wavelength and centroid shifted to the blue wing

In this case, the Doppler velocity histogram is centered at the rest wavelength, while the centroid is shifted to blue. The example shown in Figure 4.7 shows the histograms for the data set observed on 2018-05-26T13:03:57Z, where the centroid is shifted to the blue wing fully. The Doppler velocity ranges between -18 and 17 km s^{-1} with a peak near the rest wavelength. However, the centroid ranges between -93 and -58 km s^{-1} with a peak near -74 km s^{-1} which is comparatively higher than all other cases, where it ranges between -30 and 0 km s^{-1}. This example shows an extremely blueshifted centroid. We see 71 data sets (46.1 %) under this category. A majority of the data sets analyzed fall under this case. The intensity histogram is skewed toward higher values, and the line width histogram is almost symmetrical.

Case 5—Doppler velocity centered at the rest wavelength and centroid shifted to the red wing

Case 5 is complementary to Case 4 where the Doppler velocity is centered at the rest wavelength, while the centroid is shifted to the red, partially or completely. Figure 4.8 shows a typical example where the velocity histogram is peaked near rest wavelength and the centroid is shifted to red completely. The Doppler velocity ranges between -9.5 and 15.5 km s^{-1}. The centroid ranges between 12 – 37 km s^{-1} and peaks around 22 km s^{-1}. This data set is observed on 2010-12-04T23:57:52Z. The intensity histogram is skewed as usual and has multiple components, and the line width histogram is

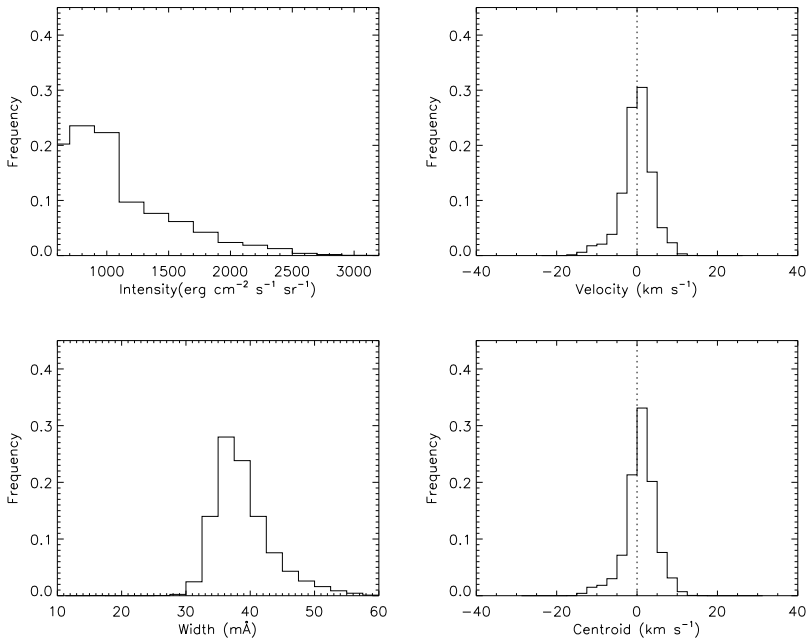

Figure 4.4: **Case 1**: Doppler velocity and centroid centered at rest wavelength. Top panel (left to right): histograms of intensity and Doppler velocity. Bottom panel (left to right): histograms of line width and centroid. The dotted line represents the zero shift.

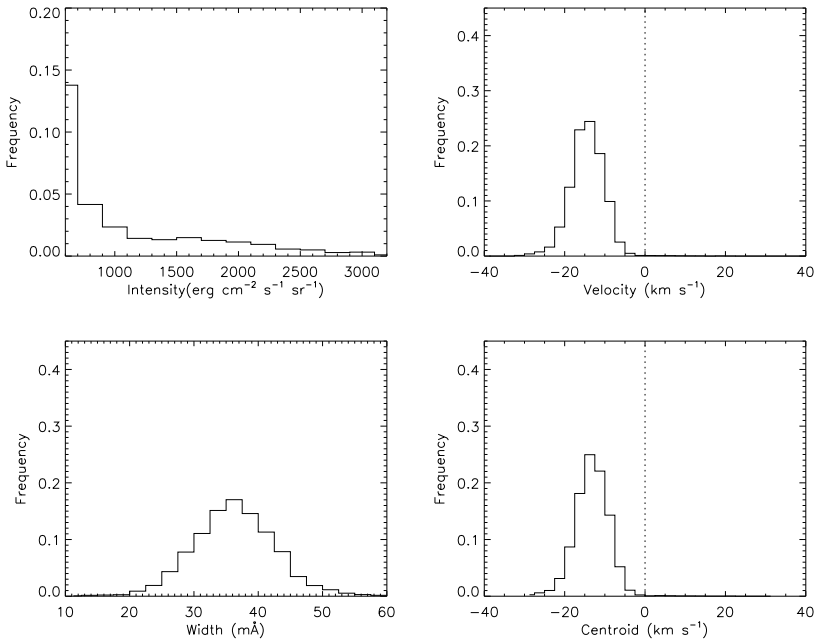

Figure 4.5: **Case 2**: Doppler velocity and centroid both shifted to blue completely. Histograms of intensity, Doppler velocity, line width, and centroid are as in Figure 4.5.

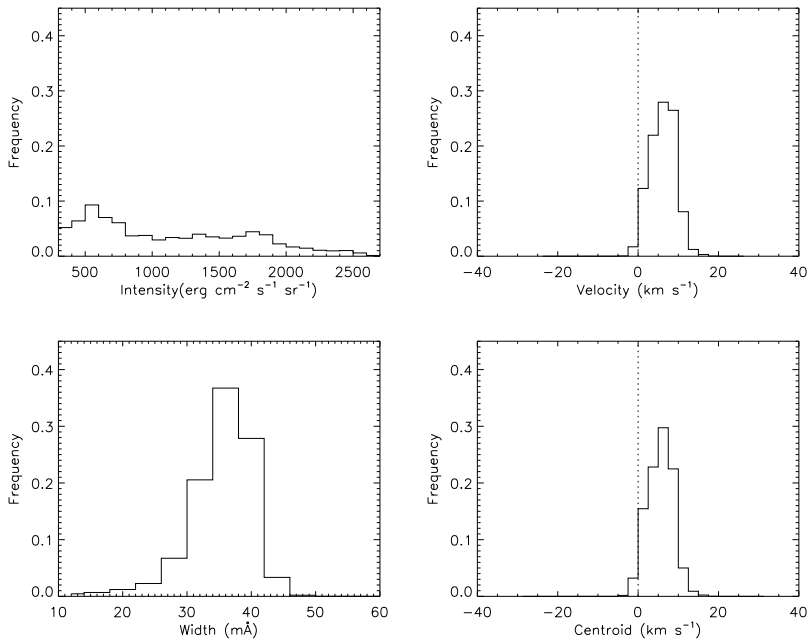

Figure 4.6: **Case 3**: Doppler velocity and centroid both shifted to red mostly. Histograms of intensity, Doppler velocity, line width, and centroid are as in Figure 4.5.

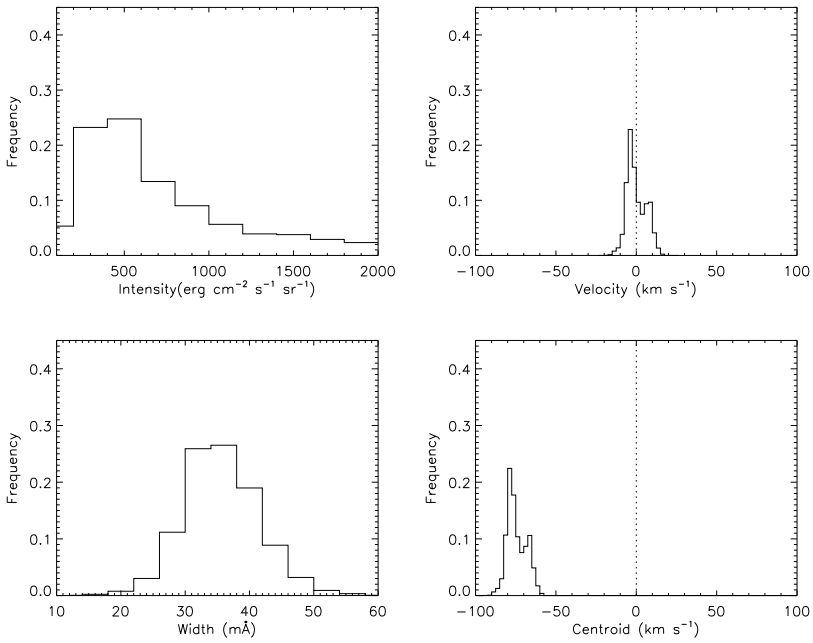

Figure 4.7: **Case 4**: Doppler velocity centered at the rest wavelength and centroid shifted to blue fully. Histograms of intensity, Doppler velocity, line width, and centroid are as in Figure 4.5.

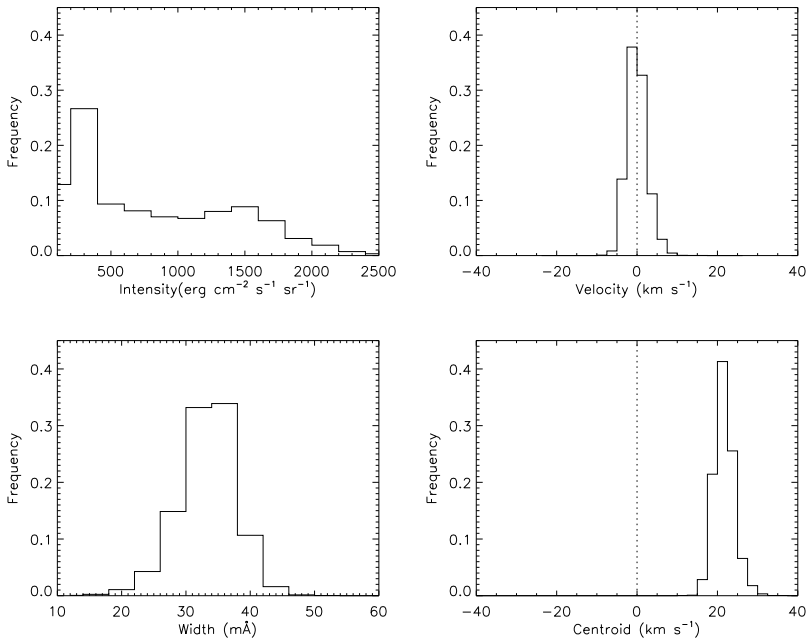

Figure 4.8: **Case 5**: Doppler velocity centered at the rest wavelength while the centroid is shifted to red completely. Histograms of intensity, Doppler velocity, line width, and centroid are as in Figure 4.5.

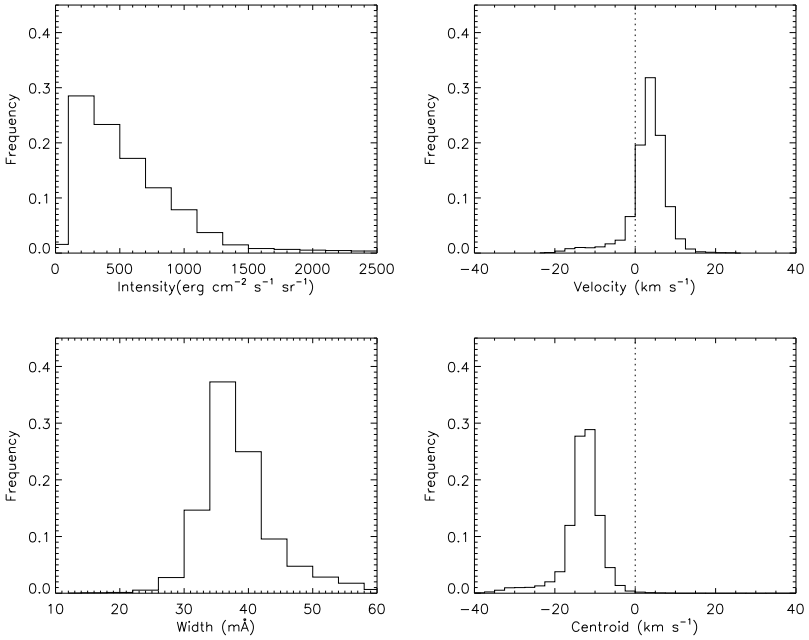

Figure 4.9: **Case 6**: Doppler velocity shifted to red largely, while the centroid is shifted to blue completely. Histograms of intensity, Doppler velocity, line width, and centroid are as in Figure 4.5.

Table 4.1: Table showing number of data sets observed in different cases

Case	Behaviour		No. of Data Sets	Percentage
	Doppler Velocity	Centroid		
1	No shift	No shift	38	24.6
2	Blueshifted	Blueshifted	1	0.64
3	Redshifted	Redshifted	2	1.29
4	No shift	Blueshifted	71	46.1
5	No shift	Redshifted	41	26.62
6	Redshifted	Blueshifted	1	0.64

almost symmetric. This case constitutes the second- largest category of data sets analyzed (26.62%).

Case 6—Doppler velocity shifted to the red wing and centroid shifted to the blue wing

This is the last category in the data sets where we see the shifts in the Doppler velocity and centroid in the opposite directions. The Doppler velocity is shifted to the red, while the centroid is shifted to the blue. We observe only one data set under this category on 2016-01-02T03:25:25Z, which is presented in Figure 4.9. Both the intensity and the line width are skewed here. The Doppler velocity ranges between -25 and 20 km s^{-1} and peaks at 3 km s^{-1}. It is mostly in red, with a small tail in the blue wing. However, the centroid, which peaks at -13 km s^{-1}, is fully in the blue wing ranging between -40 and 0 km s^{-1}.

As we have considered only one data set per month, we could have missed examples of different cases. There is also the possibility of a case complementary to Case 6 where the Doppler velocity is shifted to the blue and the centroid is shifted to the red. The results of the above analysis are summarized in Table 4.1.

Cases of double peaks

In this section, we report the special data sets where we have observed double peaks in the histograms of Doppler velocity and centroid. The data sets reported here fall under the cases mentioned above. However, their uniqueness comes from having two peaks, unlike what is seen in the previous section. The intensity and line width distributions behave as in the above cases. We report three examples here where we see such behaviour.

Figure 4.10 taken from the data set observed on 2017-08-01T01:02:41Z is an example where Doppler velocity and centroid distribution have two peaks, one in the red and one in the blue wing. Hence, this can be considered as a special case of Case 1. It may be noted that no double peaks are observed in intensity or the line width.

Figure 4.11 taken from the data set observed on 2018-06-01T03:29:43Z is a special case of Case 4. Single peaks are observed in intensity and line width histograms. The Doppler velocity and centroid histograms have two peaks. The Doppler velocity ranges between -23 and 21 km s^{-1}, with one peak

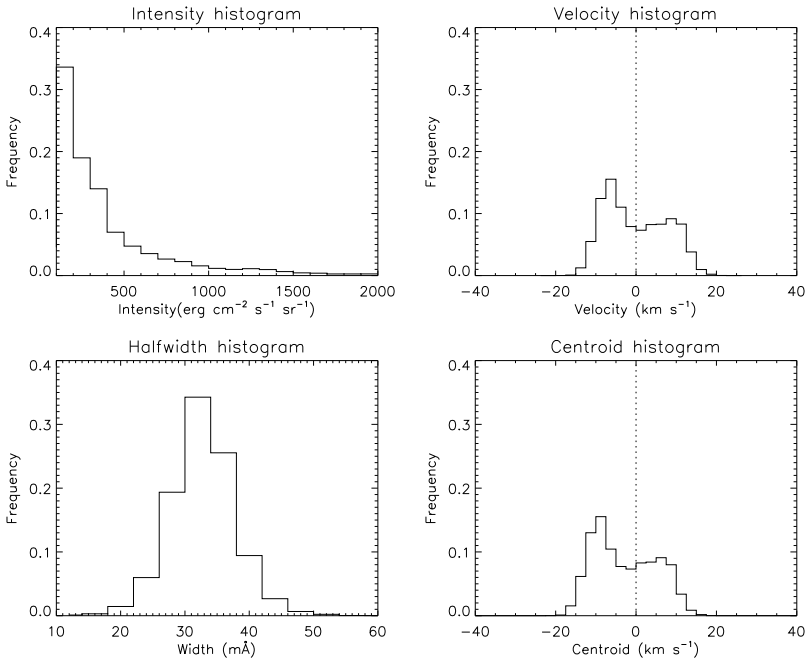

Figure 4.10: Double peaks seen in Doppler velocity and centroid, both centered at the rest wavelength. Histograms of intensity, Doppler velocity, line width, and centroid are as in Figure 4.5.

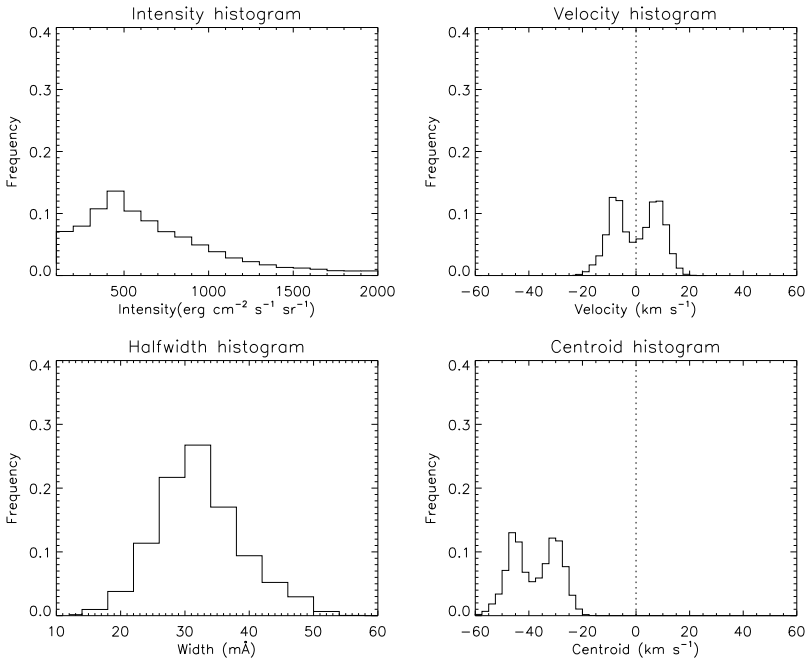

Figure 4.11: Doppler velocity is centered at the rest wavelength with double peaks. The centroid, also having double peaks is blueshifted. Histograms of intensity, Doppler velocity, line width, and centroid are as in Figure 4.5.

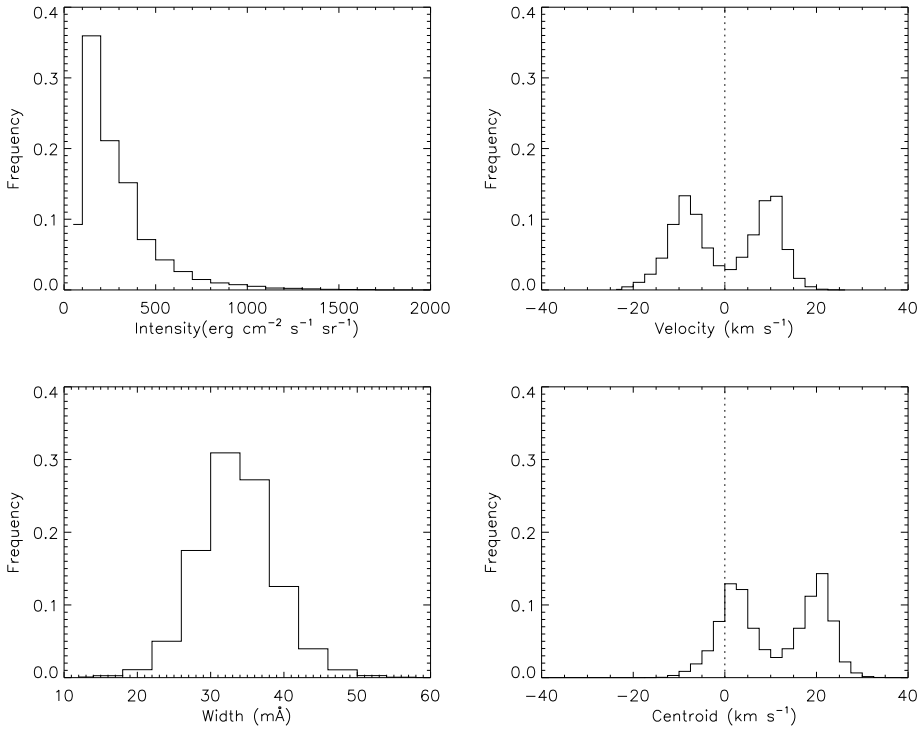

Figure 4.12: Doppler velocity is centered at the rest wavelength with double peaks showing no shift. The centroid, also having double peaks is largely redshifted. Histograms of intensity, Doppler velocity, line width, and centroid are as in Figure 4.5.

in the blue wing and one in the red wing. The centroid ranges between -62 and -16.5 km s^{-1} with an average of -38 km s^{-1} having two peaks in blue.

Figure 4.12 is presented from the data set observed on 2019-07-04T00:05:13Z and it is a special case of Case 5. The Doppler velocity ranges between -26 and 23 km s^{-1} and has two equal peaks, one in the red wing and one in the blue wing. The centroid is shifted mostly to the red, ranging between -15 and 34 km s^{-1}. Again, there are no double peaks in intensity or line width.

4.4.2 Interdependence of the Parameters

Further, we examined the interdependence among the parameters. In particular, we studied how the Doppler velocity and the centroid of each data set vary with its line width. Figure 4.13 (a), (b), (c), and (d) give examples of line width versus Doppler velocity and line width versus centroid distributions of different data sets. We have earlier studied the correlation between these quantities from ground-based eclipse observation of the coronal green line Fe XIV λ5303 and found that a quadratic polynomial gives the best fit (Maya Prabhakar, Raju, and Chandrasekhar 2019). Therefore, we have tried the quadratic polynomial fits here. The details of the fits are shown in Table 4.2. The plot of Doppler velocity/centroid versus line width from simulations shows that the variation follows a polynomial-like behaviour. In the first two cases, the trend is clear and the fitting is good, with the

Table 4.2: Table showing the quadratic correlation coefficients for the examples shown in Figure 4.13

Figure	Observation (UTC)		Quadratic R
	Date	Time	
12(a)	2012-07-05	18:18:27	0.72
12(b)	2011-05-01	09:06:05	0.69
12(c)	2011-11-01	22:58:03	0.67
12(d)	2007-11-01	06:32:06	0.005

value of correlation coefficient R being 0.72 and 0.69, respectively. This shows that the line width increases with the absolute value of Doppler velocity/centroid. In the third case also, similar trends are seen ($R = 0.67$), but there seem to be two different distributions involved. Figure 4.13 (d) shows no correlation between the quantities. In most of the other cases, the trend is similar to those shown in Figure 4.13 (a) and (b), but with a reduced correlation coefficient.

These results can be compared with those from the simulations given in Chapter-2. We found that the interdependence of line profile parameters like line width and Doppler velocity and line width and centroid are non-linear in nature. A comparison of Figure 2.2 with Figure 4.13 show some similarities. Figure 4.13 shows a dependence of width and centroid described by a second-degree polynomial in most of the cases. This would imply the presence of multiple components in the coronal active regions. The dependence of velocity and width also shows a decreasing trend at higher velocities of the order of 60 km s^{-1}. This is not seen in the results which imply that the velocities involved are less than 60 km s^{-1}.

4.4.3 Correlation with the Solar Cycle

Here we examine the dependence of the parameters on the solar cycle. Note that the EIS observational windows are located at different spatial positions over the Sun. Our aim is to find any global dependence of the parameters on the solar cycle. So we correlated the intensity, line width, Doppler velocity, and centroid with the monthly average Sunspot number. The Sunspot number is taken from the Solar Influences Data analysis Center. Since there is a time difference between the two observations, the Sunspot number is interpolated for the EIS observation times. Figure 4.14 (a) shows the temporal variation of intensity and the Sunspot number. The smoothed curve (red) is obtained from a five-point boxcar averaging. We can see that the variations of both the quantities are alike. Figure 4.14 (b) gives the cross-correlation between the two quantities as a function of lag given in years. The cross-correlation coefficient and the probability are given in Table 4.3. The maximum correlation coefficient (R) is 0.49, and the probability of the correlation occurring by chance is close to zero. The maximum correlation occurs at zero lag, and there is also an asymmetry with respect to zero lag that could be due to the difference in the rising and falling phases of the solar cycle. The solar cycle variation of intensity is obvious. Similarly, Figure 4.15 (a) and (b) explain the same for

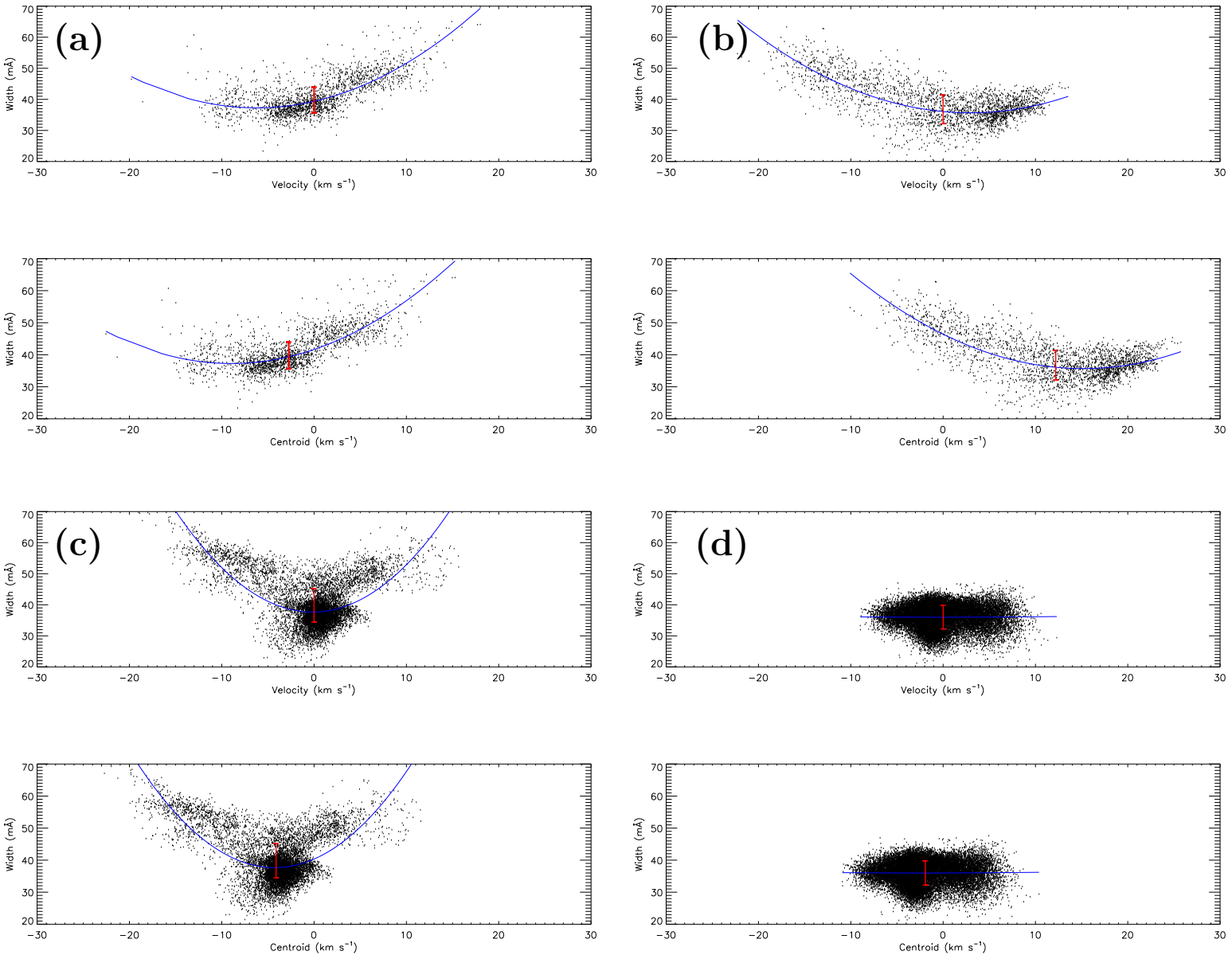

Figure 4.13: (a) Trend increasing in red having R=0.72, (b) trend increasing in blue having R=0.69, (c) symmetric trend having R=0.67 and (d) constant trend having poor R. Top panel in each sub-figure: variation of line width with Doppler velocity. Bottom panel: variation of line width with centroid.

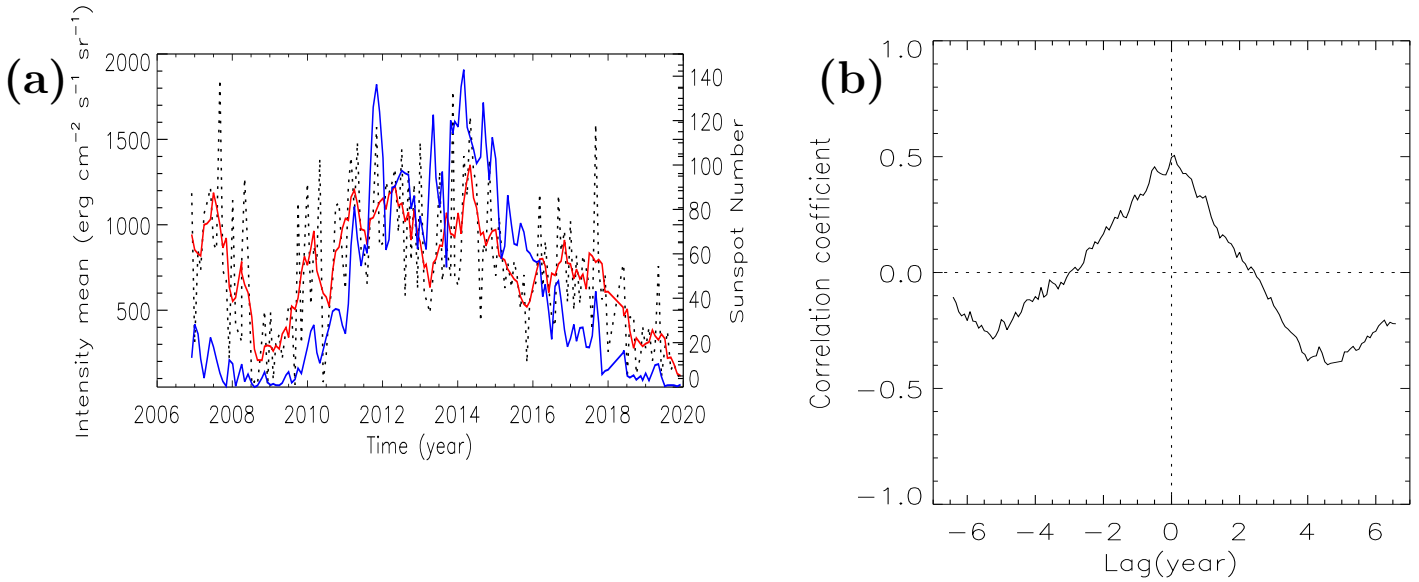

Figure 4.14: (a) Temporal variation of intensity (black) and Sunspot number (blue), with the smoothed curve (red) showing the trend of temporal variation of intensity. (b) Cross-correlation of intensity with the Sunspot number as a function of lag.

Table 4.3: Maximum and Minimum Values of the Cross-correlation Coefficient of Variation of Intensity and Line Width with Sunspot Number with Time as a Function of Lag and the Probability of the Correlations.

Parameter	Figure	R		p
		$R\ max$	$R\ min$	
Intensity	Figure 13(b)	0.49	-0.38	0.0
Line width	Figure 14(b)	0.23	-0.27	0.001

the line width. Here the maximum correlation is -0.27, which occurs at a lag of around -3 yr and the probability of the correlation is 0.001. It can be seen that the line width is weakly dependent on the solar cycle. The correlation is moderately significant because of the large number of observations (Taylor 1982), which may imply that there could be a dependence of line width on solar cycle with some lag.

4.5 Discussions

Studies of the coronal spectra in recent years have revealed that there is a ubiquitous asymmetry present in the coronal spectral line profiles. Several works have reported redshifts and blueshifts in Doppler velocity, especially in the active regions. Chae, Yun, and A. I. Poland 1998b and Peter and Judge 1999 reported blueshifts in the coronal line profiles. Marsch et al. 2008 reported blueshifts

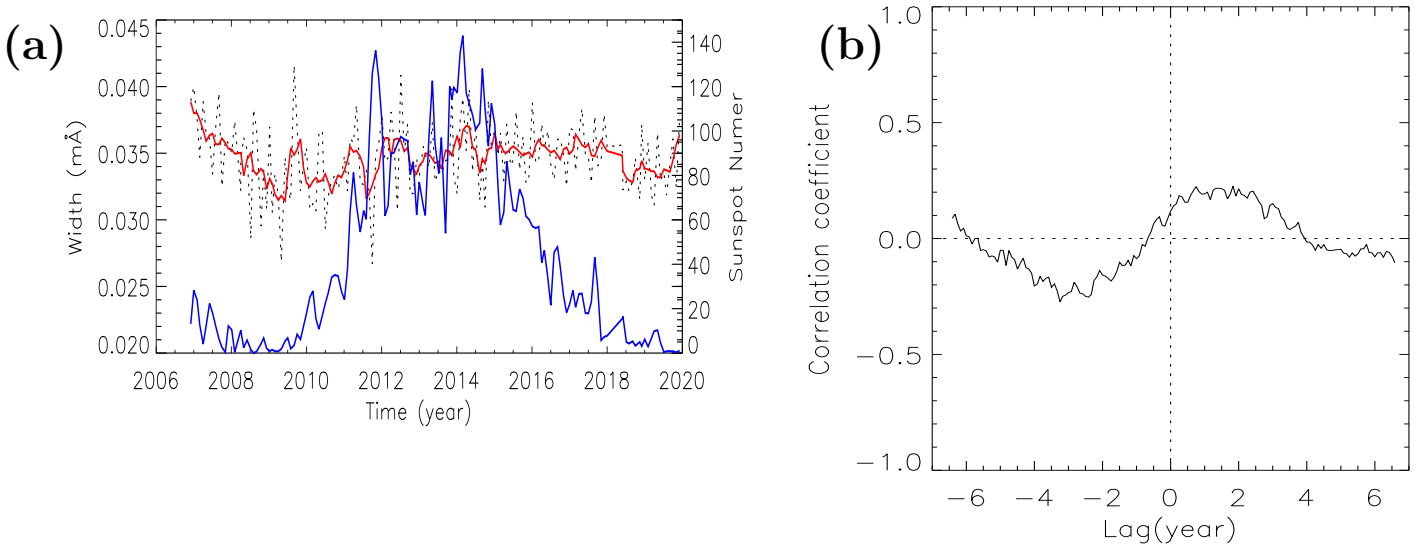

Figure 4.15: (a) Temporal variation of line width (black) and Sunspot number (blue), with the smoothed curve (red) showing the trend of temporal variation of line width. (b) Cross-correlation of line width with the Sunspot number as a function of lag.

in the active region boundaries in the EUV λ195.12 line and connected these blueshifts to the propagating disturbances. More often, the stronger blueshifts are reported in the hotter lines (T≈1-2 MK), which are found to increase as a function of temperature. F. Chen, Ding, and P. F. Chen 2010 reported blueshifts of the order of 20 km s^{-1}. From EIS observations, Tian, Scott W. McIntosh, Pontieu, et al. 2011 observed the main component of the line profiles to be stationary and the secondary component to be blueshifted. Raju, Chandrasekhar, and Ashok 2011a reported multiple components with an excess of blueshifts in the coronal green line profiles.

In Maya Prabhakar, Raju, and Chandrasekhar 2019, these authors have reported 59% blueshifts and only 7% redshifts of the Doppler velocity in the coronal green line profiles. However, in the present study, we see an almost equal distribution of blueshifts and redshifts in the Doppler velocity. We find that the shifts are mostly seen in the centroids. As indicated through the simulation, this could be due to the strong asymmetry in the long profiles. It may also be noted that the formation temperature of Fe XII λ195.12 is 1.25 MK, whereas that of the coronal green line is 2 MK. The results also imply that the Doppler velocity and centroid distributions are quite different.

The double peaks in the Doppler velocity and centroid distribution could be due to the different nature of flows in different parts of the observed active region. In a recent study, Humphries et al. 2020 show redshift at the footpoints and blueshift near the top of the coronal protrusions. Studies by Scott W. McIntosh and Pontieu 2009 and B. De Pontieu, Martinez-Sykora, et al. 2017 suggest that the outflows could be linked to chromospheric jets and spicules, which are heated while propagating into the corona. Solar wind flows are often considered to explain the active region outflows (Sakao et al. 2007). David H. Brooks, Warren, and Peter R. Young 2011, David H. Brooks and Warren 2012, and D. Brooks 2015 showed through EIS observations that the active region outflows contain

slow wind plasma composition. The reported shifts may depend on various factors like the part of the active region they belong to, the phase of the solar cycle, the wavelength of the spectral line, the height of the corona, etc. Further studies are needed to ascertain the causes of the flow.

As mentioned above, the dependence of line width on Doppler velocity/centroid has been reported. Three out of four data sets presented in Section 4.4.2 have very good correlations. We also compared the results with the line profile simulations and we see a good agreement between the two. Raju, Chandrasekhar, and Ashok 2011a found that the correlation between Doppler velocity and line width is significant. Peter 2010b states that a positive correlation between Doppler velocity and line width indicates a heating process driving a flow. Line width broadening is found to be associated with strong blueshifts in general. The enhanced line broadening is reported to lead to the growth of Alfven wave amplitude or inhomogeneity of flow velocities (F. Chen, Ding, and P. F. Chen 2010; Scott W. McIntosh and Pontieu 2009; Tian, Scott W. McIntosh, Wang, et al. 2012).

Lastly, the correlation of the intensity and the line width with the solar cycle is interesting and expected to some extent. Note that our data samples are not restricted to the disk or limb or the umbra or penumbra of the active regions, but are spread globally over the Sun. It is known that the EUV lines show an overall increase in intensity with the solar cycle. The increase in line width implies an increase in temperature and/or the nonthermal velocity with the solar cycle. This may have implications for coronal heating.

4.6 Conclusions

Active regions from different parts of the Sun were analyzed for a period of 13 years using Hinode/EIS data in the Fe XII λ195.12 line. The physical parameters intensity, line width, Doppler velocity, and centroid are obtained from their line profiles. The behaviours of the parameters are studied and compared with the multicomponent line profile simulation. We found that the Doppler velocity and centroid are not always related, but shift relatively in six different ways. Firstly, the Doppler velocity and the centroid distributions were found to be centred around the rest wavelength (Case 1). Both were found to be shifted to blue or red in Cases 2 and 3. Further, we found that the Doppler velocity was centred around the rest wavelength, while the centroid was found to shift to the blue or red partially or completely (Cases 4 and 5). Lastly, we found that the Doppler velocity was shifting to the red, while the centroid was in blue (Case 6). We found a majority of the data falling under Case 4 (46.1 %), followed by Case 5 (26.62 %), and then Case 1 (24.6%). The intensity distribution is skewed in most of the cases. The line width distribution is mostly symmetric but skewed in some cases. The average line width is found to be around 35 mÅ. The Doppler velocity and centroid are found to range between -60 and 60 km s^{-1} in most of the cases. In some extreme cases, the centroid is found to shift up to -100 – 100 km s^{-1}. The line width is found to follow a second-degree polynomial in its distribution with the Doppler velocity and the centroid. This is shown in the simulation as well. It is found that the line width increases with the increasing absolute value of Doppler velocity or

centroid in most cases. Lastly, the intensity and the line width are found to show some dependence on the solar cycle, although there is no such correlation between the Doppler velocity and centroid with the solar cycle. The global dependence of intensity and line width on the solar cycle can have implications for solar irradiance and coronal heating.

Chapter 5

Dynamics of the Coronal Holes in FeXII λ195.12 using Hinode/EIS

5.1 Introduction

Coronal holes are regions of the Sun that are less dense and cooler than the surrounding plasma. They appear as dark areas in the solar corona in EUV and soft X-ray solar images. They are regions of open, unipolar magnetic fields. This open field structure allows the solar wind to escape more readily into space leading to high-speed streams (HSS). When these solar winds are directed towards the Earth, the particles collide with the gases in our atmosphere giving rise to the northern lights. During the solar cycle minimum, it is natural for one to expect fewer auroral lights. Coronal holes ensure that the northern lights still appear regularly even during solar minimum periods.

Waldmeier is the modern discoverer of coronal holes in 1957. They were identified as 3D structures only after the space observations. Skylab's Apollo Telescope Mount's X-ray images from June 1973 revolutionized coronal hole studies.

Coronal holes can develop at any time and location on the Sun but are more common during the solar minimum periods. The more persistent coronal holes can sometimes last through several solar rotations. Coronal holes are most stable at the solar north and south poles, but these can grow and expand to lower solar latitudes. It is also possible for coronal holes to develop in isolation from the polar holes; or for an extension of a polar hole to split off and become an isolated structure. Persistent coronal holes are long-lasting sources of high-speed solar wind streams. As the HSS interacts with the relatively slower ambient solar wind, a compression region forms, known as a co-rotating interaction region (CIR). From the perspective of a fixed observer in interplanetary space, the CIR will be seen to lead the coronal hole HSS. Coronal holes can remain on the surface of the Sun for several rotations which means that they can be used as a predictive tool for geomagnetic activity. Depending on the velocity of the coronal hole HSS, the solar wind generally takes 2—4 four days to reach Earth's atmosphere.

The CIR can result in particle density enhancement. The interplanetary magnetic field (IMF)

strength increases preceding the onset of the coronal hole HSS. As the CH HSS begins to arrive at the Earth, solar wind speed and temperature increase, while particle density begins to decrease. This may result in a severe drag on the satellites, the accuracy of the GPS, disruption in the functioning radars etc. After the passage of the CIR and upon transition into the CH HSS flow, the overall IMF strength will normally begin to slowly weaken. Coronal holes located at or near the solar equator are most likely to cause geomagnetic activity. Space weather forecasters take into account these effects while forecasting the geomagnetic response.

Though the major reason to study the coronal holes is to predict their impacts on the Earth, it also holds enough mystery about its dynamics. Hence, we have extended our work on analyzing the line profiles from Hinode/EIS to the coronal holes line profiles. In continuation of our work on active regions discussed in the previous chapter, we discuss the coronal holes here. Cranmer 2018 sheds more light on the mysteries of the coronal holes and the need for their studies. Earlier, λ5303 Å images from natural or man-made eclipses were the only observations of coronal holes until the space age. However, now that we have various space-based instruments, we can track these structures and map them. Most of the space-borne solar telescopes in EUV and X-ray offer data on the coronal holes and EIS is one among them. In this chapter, we present our preliminary work on the line profile studies of the coronal holes.

5.2 Data

The details of the instrument EIS/Hinode are given in Chapter-4. As in the case of active regions, we consider coronal hole data, one per month starting from October 2006, the launch of Hinode up to the end of 2019 which coincides with the end of solar cycle 24, roughly. Here we considered only 1′ raster scans and in case of non-availability of such data, we included 2′ raster scans. Also, we took only raster scans in the present analysis. Unlike active region data, we found that there was a lot of loss of pixels in the coronal hole data. So, we considered 142 data sets in this span of 13 years. In the following sections, we present the preliminary results we have found.

5.3 Results and Discussions

Histogram analysis

We have obtained the histograms of intensity, Doppler velocity, line width and centroid. In the case of active regions, the analysis of histograms yielded 6 different cases of shifts from the rest wavelength observed in Doppler velocity and centroid with respect to the line width. Here, we have come across 9 different cases which are explained as follows.

Case 1 - Both the Doppler velocity and the centroid centred at the rest wavelength

This case is similar to Case-1 in active regions. We have come across 21 (14.78 %)data sets under this category. These data sets span from 2007 to 2014. A typical example of this category

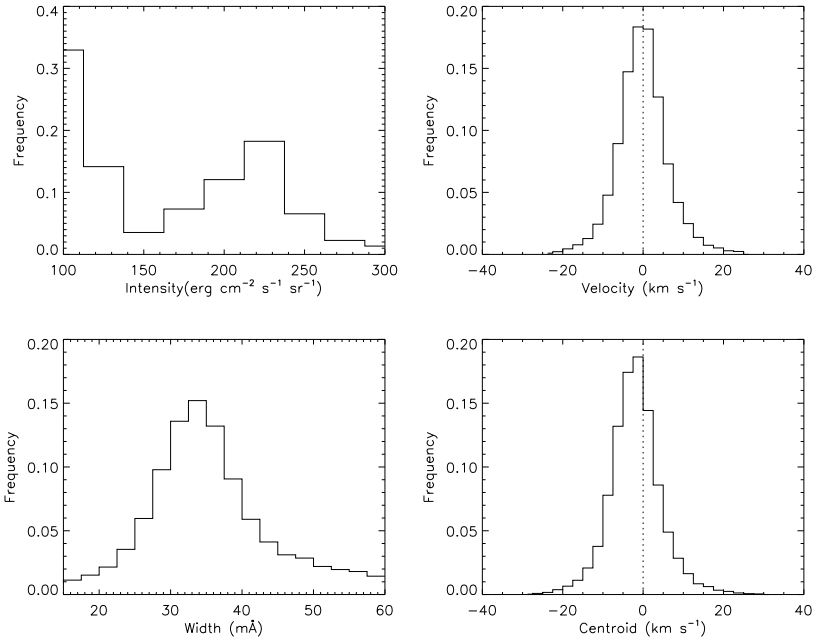

Figure 5.1: **Case 1**: Doppler velocity and centroid both centred at the rest wavelength. Top panel (left to right): Histograms of intensity and Doppler velocity. Bottom panel (left to right): Histograms of line width and centroid. The dotted line represents the zero shift.

can be found in Figure 5.1. This data set was observed on 2007-09-03T10:35:13Z. The intensity histogram shows double peaks and ranges between 100 and 300 erg cm^{-2} s^{-1} sr^{-2}. The line width ranges between 10 and 60 mÅ and peaks at 35 mÅ similar to active region line widths. The Doppler velocity and centroid range between -25 – 25 km s^{-1}.

Case 2 - Both the Doppler velocity and the centroid centred in the blue wing

This case is similar to Case-2 in active regions. In this category, we have found 19 cases (13.38%). An example of this case observed on 2008-10-04T10:51:19Z is shown in Figure 5.2. As in the previous case, the intensity histogram shows double-peak nature and it ranges between 100 and 350 erg cm^{-2} s^{-1} sr^{-2}. The line width histogram is a little skewed towards higher values and ranges between 10 – 60 mÅ peaking at 35 mÅ. The Doppler velocity ranges between -30 – 20 km s^{-1} , peaks around -5 km s^{-1} and the centroid ranges between -35 – 10 km s^{-1} peaking at -20 km s^{-1}.

Case 3 - Both the Doppler velocity and the centroid centred in the red wing

This case is similar to Case-3 in active regions where we see the Doppler velocity and the centroid are centred in red. We see 10 examples of this case from our analysis. An example data set observed on 2019-04-11T10:57:50Z is shown in Figure 5.3. The intensity ranges between 200 – 400 erg cm^{-2} s^{-1} sr^{-2} and is again a case of double-peak. It peaks at 350 erg cm^{-2} s^{-1} sr^{-2}. The line width peaks around 32 mÅ. The Doppler velocity ranges between -10 km s^{-1} and 20 km s^{-1} and peaks at 6 km s^{-1}. The centroid ranges between -5 and 30 km s^{-1} centring at 12 km s^{-1}.

Case 4 - Doppler velocity centred at the rest wavelength and centroid centred in the blue wing

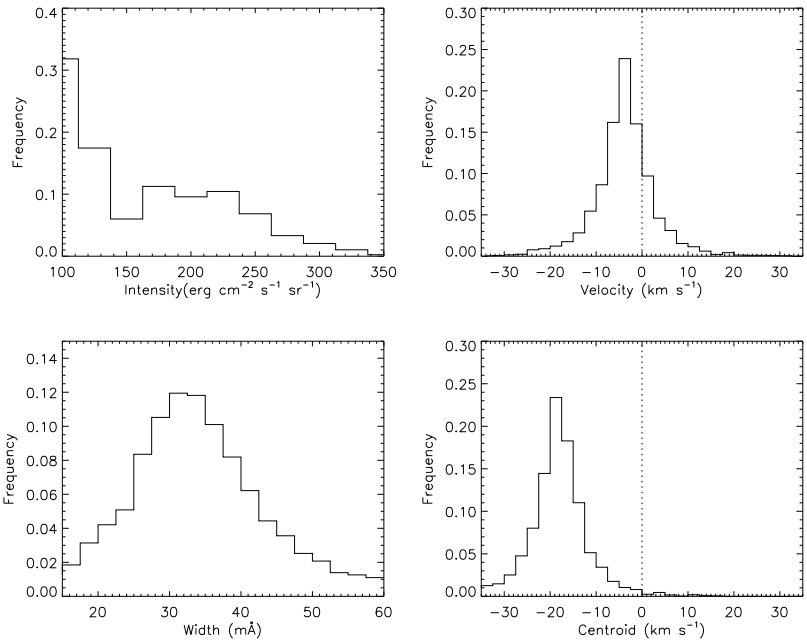

Figure 5.2: **Case 2**: Doppler velocity and centroid centered in the blue. Histograms of intensity, Doppler velocity, line width, and centroid are as in Figure 5.1.

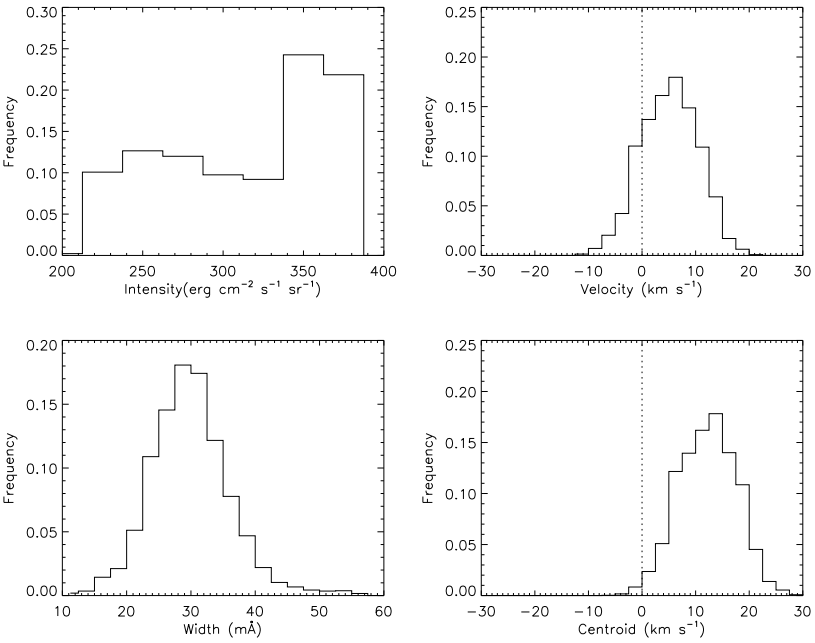

Figure 5.3: **Case 3**: Doppler velocity and centroid centered in the red. Histograms of intensity, Doppler velocity, line width, and centroid are as in Figure 5.1.

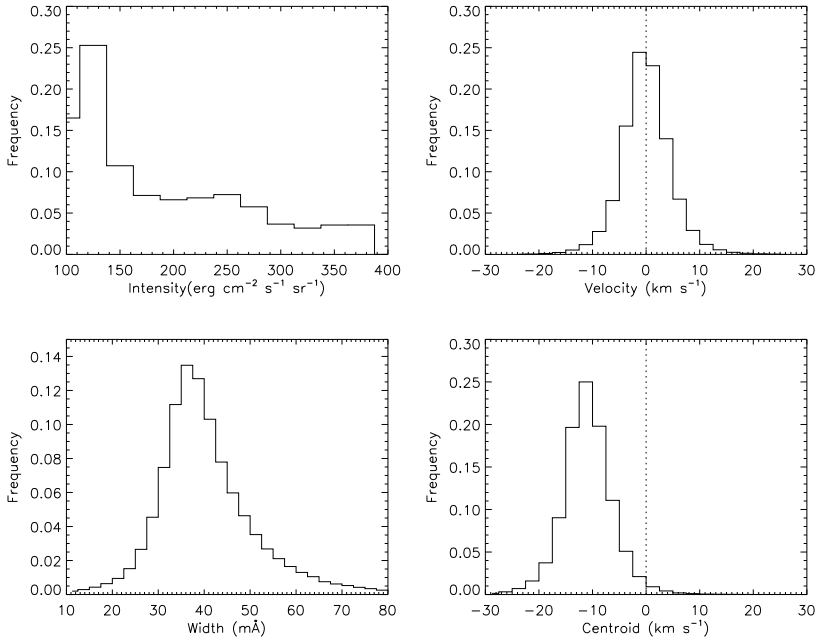

Figure 5.4: **Case 4**: Doppler velocity at the rest wavelength and centroid shifted to blue. Histograms of intensity, Doppler velocity, line width, and centroid are as in Figure 5.1

This case is similar to Case-4 in active regions. We see the maximum number (49) of data sets under this category whose example can be found in Figure 5.4. This was observed on 2012-03-22T10:02:27Z. The intensity ranges between 100 – 400 erg cm^{-2} s^{-1} sr^{-2} and is clearly skewed. The line width that ranges between 10 – 80 km s^{-1} and peaks at 35 km s^{-1}. It also shows a positive skew towards higher values. Doppler velocity ranges between -20 – 20 km s^{-1} and is centered at -1 km s^{-1}. The centroid ranges between -30 – 10 km s^{-1} and is centered at -10 km s^{-1}.

Case 5 - Doppler velocity at rest wavelength and centroid in red

This is similar to Case-5 in active regions. The Doppler velocity is peaked at the rest wavelength and the centroid peak is shifted to red. We observe 18 (12.67 %) data sets under this category. An example observed on 2010-12-03T10:05:27Z is shown in Figure 5.5. The intensity shows double peaks in between 100 – 400 erg cm^{-2} s^{-1} sr^{-2} peaking around 120 erg cm^{-2} s^{-1} sr^{-2} and 275 erg cm^{-2} s^{-1} sr^{-2}. The line width peaks at 36 Å and ranges between 10 – 80 Å. The Doppler velocity is centered at 0 km s^{-1} and ranges between -15 – 15 km s^{-1}. The centroid that ranges between 0 and 30 km s^{-1} peaks at 15 km s^{-1}.

Case 6 - Doppler velocity shifted to red and centroid shifted to blue

Here the Doppler velocity is shifted to red while the centroid is shifted to blue. The intensity has double peaks and ranges between 100 – 400 erg cm^{-2} s^{-1} sr^{-2}. The line width is almost symmetric ranging between 10 – 60 Å and peaking around 34 Å. The Doppler velocity ranges between -10 – 25 km s^{-1} centering around 7 km s^{-1}, while the centroid ranges between -20 – 15 km s^{-1} centering around -7 km s^{-1}. We find 9 cases under this category and an example observed on 2007-11-01T00:37:56Z

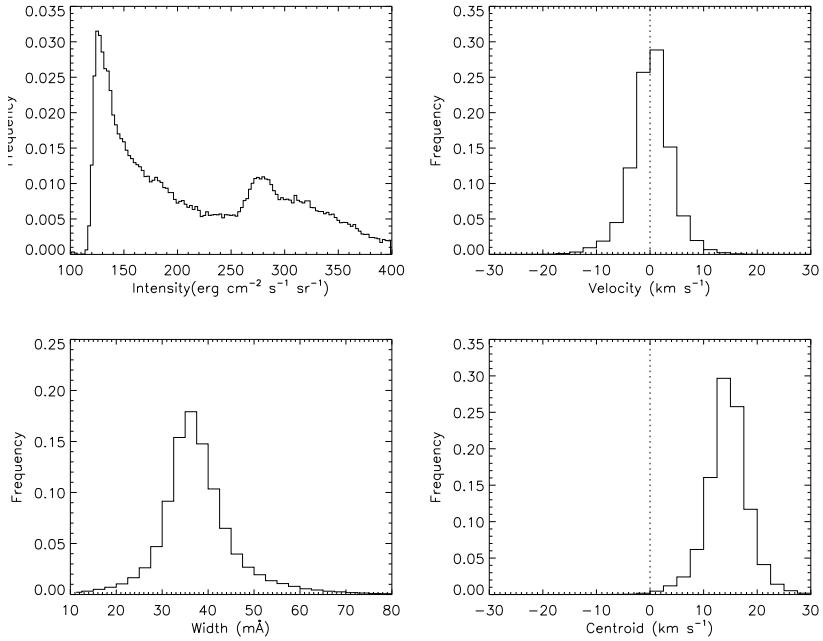

Figure 5.5: **Case 5**: Doppler velocity centred at rest wavelength and centroid shifted to red. Histograms of intensity, Doppler velocity, line width, and centroid are as in Figure 5.1

can be seen in Figure 5.6.

The statistics of all these cases are given in Table 5.1. It may be noted that 34.5 % of the samples belong to Case-4 where the Doppler velocity is peaked at the rest wavelength and the centroid is peaked in the blue. Next comes Case-1 where both velocity and centroid are peaked at the rest wavelength. It can be seen from the table that in Case-2, the velocities and centroids are peaked in blue, and in Case-3, the velocities and centroids are peaked in red. A comparison of Case-2 and 3 shows that it is about 13 % in the former and 7 % in the latter. This shows the dominance of blueshifts over redshifts. In active regions, these two cases are very few. It is found that Case-4 is dominated in active regions which are about 46 %.

Case 7 - Doppler velocity blueshifted and centroid centred at the rest wavelength

This case is complementary to Case-4. The Doppler velocity peaks in the blue and centroid peaks at the rest wavelength. It may be noted that this behaviour is not found in active regions. We have found 7 (4.92 %) examples under this category. A typical example of this case observed on 2008-12-04T18:22:55Z is shown in Figure 5.7. The intensity here ranges between 100 – 125 erg cm^{-2} s^{-1} sr^{-2} peaking at 107 erg cm^{-2} s^{-1} sr^{-2}. The line width that ranges between 10 – 100 mÅ is found to peak at 50 Å which is pretty high than the normally observed 35 Å. Doppler velocity ranges between -60 – 5 km s^{-1} and peaks at -32 km s^{-1}. Centroid ranges between -40 to 40 km s^{-1} peaks around 0 km s^{-1}.

Case 8 - Doppler velocity shifted to red and centroid centred at the rest wavelength

This case is complementary to Case-5. This category was not found in the case of active re-

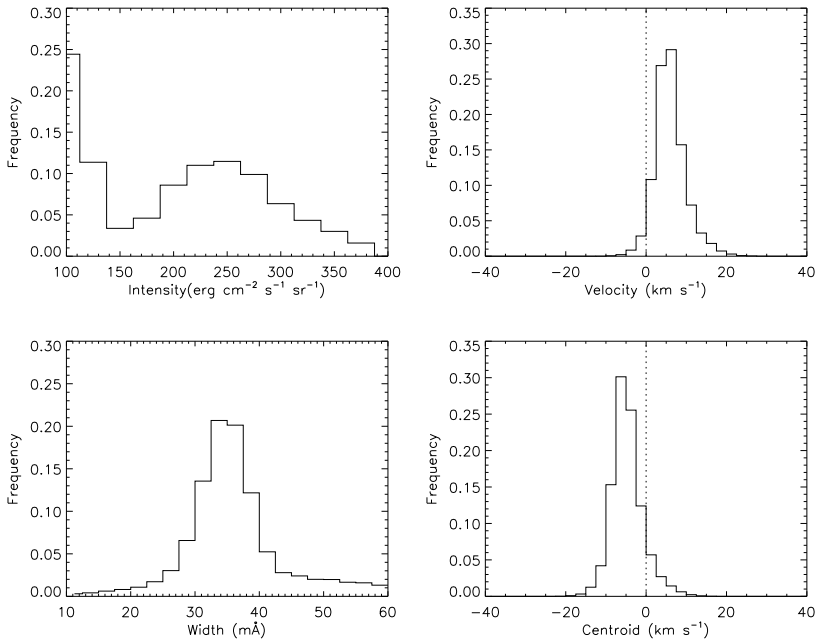

Figure 5.6: **Case 6**: Doppler velocity shifted to red while the centroid is shifted to blue. Histograms of intensity, Doppler velocity, line width, and centroid are as in Figure 5.1

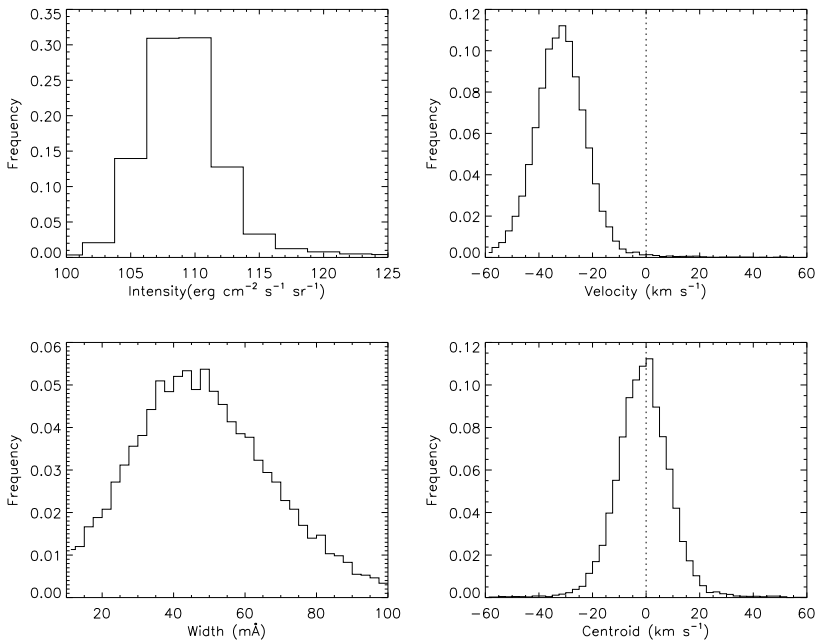

Figure 5.7: **Case 7**: Doppler velocity in blue and centroid centred at the rest wavelength. Histograms of intensity, Doppler velocity, line width, and centroid are as in Figure 5.1

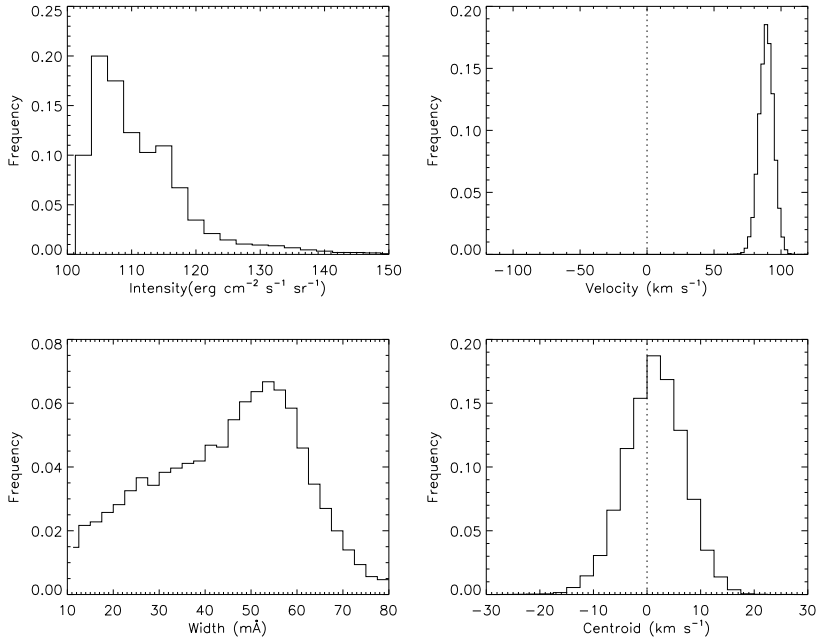

Figure 5.8: **Case 8**: Doppler velocity shifted to red fully while the centroid is centred at rest wavelength. Histograms of intensity, Doppler velocity, line width, and centroid are as in Figure 5.1

gions. We observe only 4 (2.81 %) data sets under this category. An example observed on 2007-04-07T00:22:35Z is shown in Figure 5.8. The intensity ranges between 100 – 150 erg cm^{-2} s^{-1} sr^{-2} and peaks around 105 erg cm^{-2} s^{-1} sr^{-2}. it is positively skewed. The line width peaks at 55 Å and ranges between 10 – 80 Å. It is skewed towards lower values. The Doppler velocity is centered around 85 km s^{-1} and ranges between 50 – 100 km s^{-1}. This shows an extreme shift of the Doppler velocity, while the centroid that ranges between -20 and 20 km s^{-1} peaking at 0 km s^{-1} shows no shift at all.

Case 9 - Doppler velocity shifted to blue and centroid shifted to red

The last two cases form the most interesting categories and are not found in active regions. In Case-9, we see the Doppler velocity shifting to blue, while the centroid shifts to red. A typical example of this case observed on 2019-03-01T09:52:42Z can be seen in Figure 5.9. We observe 5 examples under this category. The intensity here ranges between 100 – 250 erg cm^{-2} s^{-1} sr^{-2} and peaks around 110 erg cm^{-2} s^{-1} sr^{-2}. It is skewed. Th line width ranges between 10 – 60 Å peaking at 32 Å. The Doppler velocity and centroid range between -40 and 40 km s^{-1}. The Doppler velocity is centred around -15 km s^{-1} showing blueshift, while the centroid is centred around 10 km s^{-1} showing redshift.

5.4 Conclusions

Coronal regions spread across the Sun are considered for a span of 13 years starting from October 2006 to December 2019. We have considered 1′ and 2′ raster scan images for every month. We

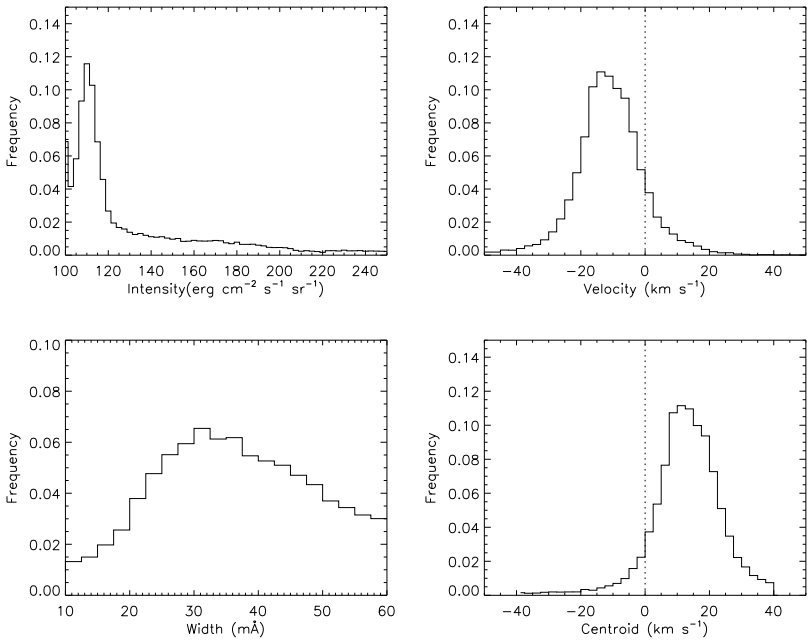

Figure 5.9: **Case 9**: Doppler velocity shifted to blue while the centroid is shifted to red. Histograms of intensity, Doppler velocity, line width, and centroid are as in Figure 5.1

Table 5.1: Table showing the number of data sets observed in different cases

Case	Behavior		No. of Data Sets	Percentage
	Doppler Velocity	Centroid		
1	No shift	No shift	21	14.78
2	Blueshifted	Blueshifted	19	13.38
3	Redhifted	Redshifted	10	7.04
4	No shift	Blueshifted	49	34.5
5	No shift	Redshifted	18	12.67
6	Redshifted	Blueshifted	9	6.33
7	Blueshifted	No shift	7	4.92
8	Redshifted	No shift	4	2.81
9	Blueshifted	Redshifted	5	3.52

analyzed the histograms of intensity, line width, Doppler velocity and centroid for all the 142 data sets considered. The study of histograms of intensity shows a double-peak nature and a positive skew in most of the data sets. The study of line width histograms shows a positive skew in most data sets. They also show a negative skew and symmetric distribution sometimes. We primarily focused on the shifts observed in the Doppler velocity and centroid with respect to the line width. We have observed 9 different cases of shifts in Doppler velocity and centroid. It may be noted that we have found 3 more cases in addition to the 6 cases seen in active regions. In the first case, we see 15 % of data sets where both the Doppler velocity and the centroid peaks are centred at the rest wavelength. We see 13 % of data sets where both the parameters' peaks are centred in the blue wing and 6 % of data sets where both are peaking in the red. The majority of the data sets (36 %) are found to have Doppler velocity peaking at the rest wavelength and centroid shifted to the blue. There are 4 % data sets with the Doppler velocity shifted to the blue and centroid centred at the rest wavelength. This case is not found in the active regions. We have observed 12 % data sets where the Doppler velocity shows no shift but the centroid peak is centred in the red and 2.25 % data sets where the Doppler velocity is redshifted while the centroid shows no shift at all. The latter one is peculiar to the coronal holes data. We have observed 3 % data sets where the Doppler velocity shifts to blue and the centroid shifts to red. Complimentary to this, the Doppler velocity shifts to red and the centroid shifts to blue in 6 % of samples. These are only the preliminary results we have found. We intend to study the inter-dependence of the line profile parameters and their correlation with the solar cycle in future.

Chapter 6

Conclusions

The Sun, our host star, located in the Milky Way galaxy has been the source of all life forms on Earth. Due to its presence and various features like eclipses and sunspots, it has intrigued the human mind. For this very reason, it was initially feared by mankind. Almost all civilizations that have existed on Earth have worshipped it. It was understood how important it is for the survival of life on Earth. The Greeks, Chinese, Babylonians, Hindus and many other civilizations considered it a deity. There have been religions based on the Sun. Early Greek astronomers like Aristarchus proposed a heliocentric model. However, Ptolemy's geocentric model prevailed till the 15^{th} century when Copernicus came up with the heliocentric model of the planetary system.

The scientific approach to studying the Sun started with Galileo when he pointed the newly invented telescope towards the Sun. Gradually, spectroscopy became a new tool which revealed many solar mysteries. The existence of dark absorption lines in the solar spectrum paved the way for the understanding of the chemical composition of the Sun. One of the major mysteries of the Sun, energy generation was resolved at the beginning of the 20^{th} century. In the high-temperature core of the Sun, hydrogen ions fuse to form helium releasing an enormous amount of energy. The solar space missions started in the 1960s which give continuous information on the Sun. Recent space missions like SOHO, SDO, Hinode, IRIS, Solar Orbiter etc have also contributed to our present-day understanding of the Sun. India's first solar space mission Aditya-L1 which will be launched soon is expected to give a lot of information about the different layers of the Sun.

The structure of the Sun consists of the solar interior, a surface and the solar exterior. The solar interior has three different layers, namely the core, radiative zone and convection zone. The photosphere is the solar surface. The solar atmosphere consists of the chromosphere, transition zone and the solar corona. Because of the high temperature of the corona, it expands as solar wind and passes through interplanetary space. Magnetic field plays a crucial role in the existence of the solar atmosphere. It is believed to be due to a dynamo process in the tachocline, which is the transition layer between the radiative and convective zones. The Sun's magnetic field cycle occurs every 22 years resulting in the reversal of the polar magnetic fields. Sunspots appear, disappear and migrate in a cyclic manner every 11 years. They form the base for most of the eruptive features seen in higher

layers.

Large-scale solar eruptive events like CMEs and flares release enormous amounts of particles and radiations which are dangerous to life. Even though the surface of the Earth is protected to some extent, these eruptive events still affect the Earth's magnetic field and atmosphere. CMEs drive shock waves which can continuously produce energetic particles as they propagate through interplanetary space. The energetic ultraviolet radiation heats the Earth's outer atmosphere, causing it to expand. This process increases the drag on the Earth-orbiting satellites resulting in the reduction of their lifetimes in their orbits. The intense radio emissions from flares and CMEs can degrade satellite communications and cause temporary loss of electrical power. Astronauts in space are also exposed to cumulative radiation which can be dangerous. The eruptive events can cause geomagnetic storms which are more disruptive now than in the past due to our greater dependence on communication technology.

Two of the most important unresolved problems in coronal physics are coronal heating and the acceleration of the solar wind. The high temperature of the corona was known since the 1940s through the works of Edlen and Grotrian (1940). Earlier attempts to explain it through acoustic waves were found to be inadequate. Later attempts invariably rely on magnetic fields. Various mechanisms like type-II spicules, nanoflares, slow and fast magnetoacoustic waves, Alfvén waves etc, are proposed to heat the corona. The release of magnetic energy occurs through magnetic reconnection. Parker proposed the existence of solar wind as a consequence of a million-degree solar corona in 1958. The solar wind streams off the solar atmosphere at speeds of about 400 km s^{-1} in all directions. However, the details about how and where the coronal gases are accelerated to high velocities are not understood. There is also a fast solar wind with speeds around 800 km s^{-1} originating from the solar coronal holes.

Some of the major findings in coronal physics in recent years are the following. The multi-component nature of the coronal line profiles with asymmetries has been generally found. Redshifts in the transition region and blueshifts in the coronal region are generally observed. Dominant blueshifts in coronal lines are interpreted to be due to the nascent solar wind flow or type-II spicules. The inter-dependency of line profile parameters, especially the linewidth with the Doppler velocity and the centroid is reported. The coronal line profiles are known to have non-thermal line widths in addition to thermal widths. Variations of the non-thermal velocity with line width and height are also reported. Large outflows in the boundaries of the active regions have been discovered in recent years.

The aim of the thesis is to study the two most important and connected problems in astronomy, namely, solar coronal heating and the acceleration of solar wind. We have also studied the solar cycle variation of the physical parameters of the solar corona. We used the ground-based eclipse observations and the space based-Hinode/EIS observations. These involve two emission lines Fe XIV 5303 Å and Fe XII 195.12 Å. The formation temperature of the former is 1.8 MK and that of the latter is 1.25 MK. This gives an opportunity to study the solar corona at two different levels. The main emphasis of the study is to examine the variation of line profile parameters like intensity, linewidth,

non-thermal width, Doppler velocity, asymmetry and line centroid in different coronal regions like the active regions and the coronal holes. We also studied the inter-dependence of the line profile parameters and their variation with the coronal magnetic activity.

Spectroscopy is a scientific tool used to get the spectra of an object. Spectroscopic instruments disperse light into its component wavelengths and thereby provide information about the source. There are various types of spectrometers like prism spectrometers, grating spectrometers and interferometers. Generally, interferometers have the largest spectral resolution. Spectroscopic measurements can give line profiles which are a plot of intensity versus wavelength. They provide information on intensity, linewidth and Doppler velocity and one can further deduct the temperature, density, mass motions etc.

A line profile is simulated by combining a stationary main component and a varying subsidiary component. The intensity, velocity and linewidth of the subsidiary component are varied and the resultant profile is examined. It is found that the input parameters of the two components affect the resultant profile. The estimated velocities and centroids in the single Gaussian fit are much smaller than that of the subsidiary component. The resultant line profile is found to be more sensitive to the variations of velocity and linewidth than the intensity of the subsidiary component. In the case of velocity variations, the behaviour of linewidth with Doppler velocity shows that the resultant velocity starts decreasing at higher values, while the centroid continues to increase. In the case of linewidth variations, the results are similar with the velocity decreasing, but the centroid tends to become constant. In the case of intensity variations, the result is peculiar with the velocity and centroid being almost similar. The simulations are a sample of how the parameters of the subsidiary component affect the resultant component. There can be more realistic situations where the parameters of the two components are simultaneously varied. We compared these results with the actual line profiles obtained from the observations.

We studied various characteristics of the inner solar corona by analyzing the line profiles obtained from the analysis of the Fabry-Perot interferograms. The observations were done by the Physical Research Laboratory team during the total solar eclipse of 21 June 2001 at Lusaka, Zambia. We found that a majority of these line profiles comprise of multicomponents, with a higher contribution from the blueshifts (59 %) followed by the single component profiles (34 %). The redshifts were found very less with just 7 %. This result is in agreement with the related works reported earlier. Line profiles showing the greatest asymmetry were found to be blueshifted and they constituted close to 7.5% of the observed line profiles. Blueshifts were found to have a maximum Doppler velocity of -18 km s^{-1} and the redshifts have a maximum Doppler velocity of 11 km s^{-1}. These values specify the Doppler velocity of the composite profile and the actual values of the Doppler velocity of the components could be much higher. This is also seen in simulation studies. The excess blueshifts could be related to the type-II spicules or the nascent solar wind flow. Further, the variation of halfwidth and Doppler velocity with respect to the coronal height are found to be insignificant. The variation of halfwidth with respect to the Doppler velocity or centroid shows a parabolic trend with a weak correlation. The positive correlation is important as it suggests a flow associated with a

heating process. We have compared the results with line profile simulations and there is generally a good agreement except when the Doppler velocities are high.

Active regions from different parts of the Sun were analyzed for a period of 13 years using Hinode/EIS data in the Fe XII λ195.12 line. This period covers the last two years of solar cycle 23 and the solar cycle 24 fully. The physical parameters intensity, line width, Doppler velocity, and centroid are obtained from their line profiles. The behaviours of the parameters are studied and compared with the multicomponent line profile simulations. We found that the Doppler velocity and centroid are not always related, but shift relatively in six different ways. Firstly, the Doppler velocity and the centroid distributions were found to be centred around the rest wavelength (Case 1). Both were found to be shifted to blue or red in Cases 2 and 3. Further, we found that the Doppler velocity was centred around the rest wavelength, while the centroid was found to shift to the blue or red partially or completely (Cases 4 and 5). Lastly, we found that the Doppler velocity was shifting to the red, while the centroid was in blue (Case 6). The majority of the data were found to fall under Case 4 (46 %), followed by Case 5 (27 %) and Case 1 (25 %). The intensity distribution is skewed in most of the cases. The line width distribution is mostly symmetric but skewed in some cases. The average line width is found to be around 35 mÅ. The Doppler velocity and centroid are found to range between -60 and 60 km s^{-1} in most of the cases. In some extreme cases, the centroid is found to shift up to -100 – 100 km s^{-1}. The line width is found to follow a second-degree polynomial in its distribution with the Doppler velocity and the centroid. The line width increases with the increasing absolute value of Doppler velocity or centroid in most cases. This is shown in the simulation as well. Lastly, the intensity and the line width are found to show some dependence on the solar cycle, although there is no such correlation between the Doppler velocity and centroid with the solar cycle. The global dependence of intensity and linewidth on the solar cycle can have implications for solar irradiance and coronal heating.

Lastly, we carried out similar studies for the coronal hole data from Hinode/EIS in 195.12λ for 13 years. The period is the same as that for active regions. Here we found 9 different cases of shifts in Doppler velocity and centroid with respect to the linewidth. The six cases found in active regions are found here as well. In addition, we found 3 more cases complementary to cases 4, 5 and 6 seen in active regions. They are Case-7, where the Doppler velocity blueshifts and the centroid is at the rest wavelength, Case-8, where the Doppler velocity redshifts and the centroid is at rest wavelength, and Case-9 where the Doppler velocity shifts to blue and the centroid shifts to the red. The majority of the cases are where the centroid is blueshifted and the Doppler velocity is at the rest wavelength (Case-4, 36 %) similar to what we see in active regions. We have presented the preliminary results here and would like to further extend our studies by studying the inter-dependence of the line profile parameters and their dependence on the solar cycle.

We expect that our results give valuable inputs to the understanding of coronal heating and acceleration of solar winds. The behaviour of line profiles in different coronal regions such as active regions and coronal holes is important in coronal dynamics. The dependence of line profile parameters on the solar cycle has implications for solar irradiance and coronal heating. This needs to be further

probed using longer data sets. We plan to extend our work to quiet sun regions and flares using the Hinode data involving other emission lines and more recent data. In addition to Fe XII 195.12Å emission line, we can use other lines such as Fe XIII, Fe XIV etc, with higher formation temperatures. This will give information on different heights of the solar corona. We would also like to compare our results with the data from other solar space missions like IRIS, SDO, Solar Orbiter etc. We also look forward to the Aditya-L1 data where one of the emission lines involved is the coronal green line Fe XIV 5303 Å. This gives an opportunity to have a direct comparison of our results. Aditya-L1 also has several other solar instruments which may enrich coronal physics.

Bibliography

Book Sources

Taylor, John R. (1982). *An Introduction to Error Analysis. The Study of Uncertainties in Physical Measurements*. IOP Publishing Ltd.

Paper Sources

Antiochos, Spiro et al. (June 1997). *The Solar-B Mission*. Technical Report, Montana State Univ. Bozeman, MT United States.

Atherton, PD et al. (1981). "Tunable fabry-perot filters". In: *Optical Engineering* 20.6, pp. 806–814.

Ballik, E. A. (Jan. 1966). "The Response of Scanning Fabry-Perot Interferometers to Atomic Transition Profiles". In: *Appl. Opt.* 5.1, 170$_1$–172. DOI: 10.1364/AO.5.0170_1. URL: http://opg.optica.org/ao/abstract.cfm?URI=ao-5-1-170_1.

Bates, B. (June 1977). "Book Review: Detection and spectrometry of faint light. JOHN MEABURN Reidel, Dordrecht. 1976. vii + 270. Dfl. 90. U.S. $34.00". In: 25.6, pp. 605–605. DOI: 10.1016/0032-0633(77)90073-3.

Beck, C. et al. (Oct. 2016). "Spectroscopy at the Solar Limb: II. Are Spicules Heated to Coronal Temperatures?" In: 291, pp. 2281–2328. DOI: 10.1007/s11207-016-0964-4. arXiv: 1606.06132.

Beckers, J. M. (Mar. 1968). "Solar Spicules (Invited Review Paper)". In: 3.3, pp. 367–433. DOI: 10.1007/BF00171614.

Brekke, P. et al. (June 2000). "The Extreme-Ultraviolet Solar Irradiance Spectrum Observed with the Coronal Diagnostic Spectrometer (CDS) on SOHO". In: 536.2, pp. 959–970. DOI: 10.1086/308966.

Brooks, D. (Dec. 2015). "Full Sun Observations for Identifying the Source of the Slow Solar Wind." In: *AGU Fall Meeting Abstracts*. Vol. 2015, SH54B-06, SH54B–06.

Brooks, David H., Louise Harra, et al. (Aug. 2021). "The Formation and Lifetime of Outflows in a Solar Active Region". In: 917.1, 25, p. 25. DOI: 10.3847/1538-4357/ac0917. arXiv: 2106.03318.

Brooks, David H. and Harry P. Warren (Nov. 2012). "THE CORONAL SOURCE OF EXTREME-ULTRAVIOLET LINE PROFILE ASYMMETRIES IN SOLAR ACTIVE REGION OUTFLOWS".

In: *ApJL* 760.1, p. L5. DOI: 10.1088/2041-8205/760/1/l5. URL: https://doi.org/10.1088/2041-8205/760/1/l5.

Brooks, David H., Harry P. Warren, and Ignacio Ugarte-Urra (Aug. 2012). "Solar Coronal Loops Resolved by Hinode and the Solar Dynamics Observatory". In: 755.2, L33, p. L33. DOI: 10.1088/2041-8205/755/2/L33.

Brooks, David H., Harry P. Warren, and Peter R. Young (Apr. 2011). "EUV Spectral Line Formation and the Temperature Structure of Active Region Fan Loops: Observations with Hinode/EIS and SDO/AIA". In: 730.2, 85, p. 85. DOI: 10.1088/0004-637X/730/2/85. arXiv: 1101.5240.

Brown, Charles M. et al. (Nov. 2007). "Wavelength Determination for Solar Features Observed by the EUV Imaging Spectrometer on Hinode". In: 59, S865. DOI: 10.1093/pasj/59.sp3.S865.

Bryans, P., P. R. Young, and G. A. Doschek (June 2010). "Multiple Component Outflows in an Active Region Observed with the EUV Imaging Spectrometer on Hinode". In: 715, pp. 1012–1020. DOI: 10.1088/0004-637X/715/2/1012. arXiv: 1004.5085.

Chabbal, R (1953). "J. recherches centre nat recherche sci". In: *Lab. Bellevue (Paris)* 24, p. 138.

Chabbal, Robert (1959). "Recherches expérimentales sur la généralisation de l'emploi du spectromètre Fabry-Perot aux divers domaines de la spectroscopie". PhD thesis. Éditions de la" Revue d'optique théorique et instrumentale".

Chae, J., H. S. Yun, and A. I. Poland (Jan. 1998a). "Temperature Dependence of Ultraviolet Line Average Doppler Shifts in the Quiet Sun". In: 114, pp. 151–164. DOI: 10.1086/313064.

— (Jan. 1998b). "Temperature Dependence of Ultraviolet Line Average Doppler Shifts in the Quiet Sun". In: *The Astrophysical Journal Supplement Series* 114.1, pp. 151–164. DOI: 10.1086/313064. URL: https://doi.org/10.1086%2F313064.

Chandrasekhar, T. et al. (Feb. 1984). "Fabry-Perot interferometric observations of the coronal red and green lines during the 1983 Indonesian eclipse". In: 23, pp. 508–511. DOI: 10.1364/AO.23.000508.

Chen, F., M. D. Ding, and P. F. Chen (Aug. 2010). "SPECTROSCOPIC ANALYSIS OF AN EIT WAVE/DIMMING OBSERVED BYHINODE/EIS". In: *The Astrophysical Journal* 720.2, pp. 1254–1261. DOI: 10.1088/0004-637x/720/2/1254. URL: https://doi.org/10.1088%2F0004-637x%2F720%2F2%2F1254.

Cranmer, S. R. (Dec. 2018). "Unsolved Problems in the Middle Corona". In: *AGU Fall Meeting Abstracts*. Vol. 2018, SH34A-01, SH34A–01.

Culhane, J. L. et al. (June 2007). "The EUV Imaging Spectrometer for Hinode". In: 243.1, pp. 19–61. DOI: 10.1007/s01007-007-0293-1.

Curdt, W. (Jan. 2003). "Solar observations from space and from the ground". In: *Astronomische Nachrichten* 324.4, pp. 334–337. DOI: 10.1002/asna.200310117.

Dadashi, N., L. Teriaca, and S. K. Solanki (Oct. 2011). "The quiet Sun average Doppler shift of coronal lines up to 2 MK". In: 534, A90, A90. DOI: 10.1051/0004-6361/201117234. arXiv: 1109.4493.

De Pontieu, B., V. H. Hansteen, et al. (Jan. 2007). "High-Resolution Observations and Modeling of Dynamic Fibrils". In: 655.1, pp. 624–641. DOI: 10.1086/509070. arXiv: astro-ph/0701786.

De Pontieu, B., J. Martinez-Sykora, et al. (Dec. 2017). "Observations and Modeling of Transition Region and Coronal Heating Associated with Spicules". In: *AGU Fall Meeting Abstracts*. Vol. 2017, SH43A-2793, SH43A–2793.

De Pontieu, B., S. W. McIntosh, et al. (Aug. 2009). "Observing the Roots of Solar Coronal Heatingin the Chromosphere". In: 701, pp. L1–L6. DOI: 10.1088/0004-637X/701/1/L1. arXiv: 0906.5434.

De Pontieu, Bart, Robert Erdélyi, and Stewart P. James (July 2004). "Solar chromospheric spicules from the leakage of photospheric oscillations and flows". In: 430.6999, pp. 536–539. DOI: 10.1038/nature02749.

Delone, A. B. and E. A. Makarova (Sept. 1969). "Interferometric Investigation of the Red and Green Coronal Lines During the Total Solar Eclipse of May 30, 1965". In: 9, pp. 116–130. DOI: 10.1007/BF00145733.

— (Nov. 1975). "Interferometric investigation of the line of sight velocities in the 5303-A line during the eclipse of 11 September, 1968". In: 45, pp. 157–168. DOI: 10.1007/BF00152228.

Dere, Kenneth P. et al. (Nov. 2007). "The Structure and Dynamics of the Quiet Corona from Observations with the Extreme Ultraviolet Imaging Spectrometer on Hinode". In: *Publications of the Astronomical Society of Japan* 59.sp3, S721–S726. ISSN: 0004-6264. DOI: 10.1093/pasj/59.sp3.S721. eprint: https://academic.oup.com/pasj/article-pdf/59/sp3/S721/17451984/pasj59-S721.pdf. URL: https://doi.org/10.1093/pasj/59.sp3.S721.

Desai, J. N. (Jan. 1984). "Fabry-Perot spectroscopy in space science." In: *Proceedings of the Indian Academy of Science, Earth and Planetary Sciences* 93.3, pp. 189–200.

Domingo, V, B Fleck, and Arthur I Poland (1995). "The SOHO mission: an overview". In: *Solar Physics* 162.1, pp. 1–37.

Doschek, G. A. et al. (Oct. 2008). "Flows and Nonthermal Velocities in Solar Active Regions Observed with the EUV Imaging Spectrometer on Hinode: A Tracer of Active Region Sources of Heliospheric Magnetic Fields?" In: 686.2, pp. 1362–1371. DOI: 10.1086/591724. arXiv: 0807.2860.

Hara, Hirohisa et al. (May 2008). "Coronal Plasma Motions near Footpoints of Active Region Loops Revealed from Spectroscopic Observations with Hinode EIS". In: 678.1, p. L67. DOI: 10.1086/588252.

Harra, L. et al. (June 2021). "The active region source of a type III radio storm observed by Parker Solar Probe during encounter 2". In: 650, A7, A7. DOI: 10.1051/0004-6361/202039514. arXiv: 2102.04964.

Hernandez, G. (Nov. 1966). "Analytical Description of a Fabry–Perot Photoelectric Spectrometer". In: *Appl. Opt.* 5.11, pp. 1745–1748. DOI: 10.1364/AO.5.001745. URL: http://opg.optica.org/ao/abstract.cfm?URI=ao-5-11-1745.

Hollweg, Joseph V. (1978). "Some physical processes in the solar wind". In: *Reviews of Geophysics* 16.4, pp. 689–720. DOI: https://doi.org/10.1029/RG016i004p00689. eprint: https://agupubs.onlinelibrary.wiley.com/doi/pdf/10.1029/RG016i004p00689. URL: https://agupubs.onlinelibrary.wiley.com/doi/abs/10.1029/RG016i004p00689.

Humphries, Llŷr Dafydd et al. (July 2020). "Multiwavelength Imaging and Spectral Analysis of Jet-like Phenomena in a Solar Active Region Using IRIS and AIA". In: 898.1, 17, p. 17. DOI: 10.3847/1538-4357/ab974d.

Jarrett, A. H. and H. von Klüber (Jan. 1961). "Interferometric investigation of emission lines of the solar corona during the total solar eclipse of 1958 October 12". In: 122, p. 223. DOI: 10.1093/mnras/122.3.223.

Jordan, Carole (Jan. 1969). "The ionization equilibrium of elements between carbon and nickel". In: 142, p. 501. DOI: 10.1093/mnras/142.4.501.

Kim, Iraida S. (Apr. 1994). "On the Fabry-Perot investigations of the solar corona: Eclipse observations of large-scale dynamics". In: *Advances in Space Research* 14.4, pp. 45–48. DOI: 10.1016/0273-1177(94)90158-9.

Klimchuk, J. A. (Dec. 2012). "The role of type II spicules in the upper solar atmosphere". In: *Journal of Geophysical Research (Space Physics)* 117.A12, A12102, A12102. DOI: 10.1029/2012JA018170. arXiv: 1207.7048.

Klimchuk, James A. (Mar. 2006). "On Solving the Coronal Heating Problem". In: 234.1, pp. 41–77. DOI: 10.1007/s11207-006-0055-z. arXiv: astro-ph/0511841.

Korendyke, Clarence M. et al. (Dec. 2006). "Optics and mechanisms for the Extreme-Ultraviolet Imaging Spectrometer on the Solar-B satellite". In: 45.34, pp. 8674–8688. DOI: 10.1364/AO.45.008674.

Kosugi, T. et al. (June 2007). "The Hinode (Solar-B) Mission: An Overview". In: 243.1, pp. 3–17. DOI: 10.1007/s11207-007-9014-6.

— (2008). "The Hinode (Solar-B) Mission: An Overview". In: *The Hinode Mission*. Ed. by Takashi Sakurai. New York, NY: Springer New York, pp. 5–19. ISBN: 978-0-387-88739-5. DOI: 10.1007/978-0-387-88739-5_3. URL: https://doi.org/10.1007/978-0-387-88739-5_3.

Lang, James et al. (Dec. 2006). "Laboratory calibration of the Extreme-Ultraviolet Imaging Spectrometer for the Solar-B satellite". In: 45.34, pp. 8689–8705. DOI: 10.1364/AO.45.008689.

Macneil, Allan R. et al. (Dec. 2019). "Active Region Modulation of Coronal Hole Solar Wind". In: 887.2, 146, p. 146. DOI: 10.3847/1538-4357/ab5586.

Mariska, J. T. (Feb. 2013). "On-Orbit Sensitivity Evolution of the EUV Imaging Spectrometer on Hinode". In: 282.2, pp. 629–639. DOI: 10.1007/s11207-012-0200-9. arXiv: 1211.3694 [astro-ph.SR].

Mariska, John T. and K. Muglach (Apr. 2010). "Doppler-shift, Intensity, and Density Oscillations Observed with the Extreme Ultraviolet Imaging Spectrometer on Hinode". In: 713.1, pp. 573–583. DOI: 10.1088/0004-637X/713/1/573. arXiv: 1003.0420 [astro-ph.SR].

Marsch, Eckart et al. (Oct. 2008). "Plasma Flows Guided by Strong Magnetic Fields in the Solar Corona". In: 685.2, pp. 1262–1269. DOI: 10.1086/591038.

McIntosh, S. W. et al. (Apr. 2012). "On the Doppler Velocity of Emission Line Profiles Formed in the "Coronal Contraflow" that Is the Chromosphere-Corona Mass Cycle". In: 749, 60, p. 60. DOI: 10.1088/0004-637X/749/1/60. arXiv: 1202.1248.

McIntosh, Scott W., Bart de Pontieu, and Robert J. Leamon (Aug. 2010). "The Impact of New EUV Diagnostics on CME-Related Kinematics". In: 265.1-2, pp. 5–17. DOI: 10.1007/s11207-010-9538-z. arXiv: 1001.2022.

McIntosh, Scott W. and Bart De Pontieu (Nov. 2009). "OBSERVING EPISODIC CORONAL HEATING EVENTS ROOTED IN CHROMOSPHERIC ACTIVITY". In: *ApJL* 706.1, pp. L80–L85. DOI: 10.1088/0004-637x/706/1/l80. URL: https://doi.org/10.1088%2F0004-637x%2F706%2F1%2Fl80.

Mierla, M. et al. (Mar. 2008). "Analysis of the Fe X and Fe XIV line width in the solar corona using LASCO-C1 spectral data". In: 480, pp. 509–514. DOI: 10.1051/0004-6361:20078329. arXiv: 0903.0496.

Parker, E. N. (Nov. 1958). "Dynamics of the Interplanetary Gas and Magnetic Fields." In: 128, p. 664. DOI: 10.1086/146579.

— (July 1988). "Nanoflares and the Solar X-Ray Corona". In: 330, p. 474. DOI: 10.1086/166485.

Parnell, Clare E. and Ineke De Moortel (July 2012). "A contemporary view of coronal heating". In: *RSPTA* 370.1970, pp. 3217–3240. ISSN: 1471-2962. DOI: 10.1098/rsta.2012.0113. URL: http://dx.doi.org/10.1098/rsta.2012.0113.

Patsourakos, S. and J. A. Klimchuk (Aug. 2006). "Nonthermal Spectral Line Broadening and the Nanoflare Model". In: 647, pp. 1452–1465. DOI: 10.1086/505517.

Peter, H. (Oct. 2010a). "Asymmetries of solar coronal extreme ultraviolet emission lines". In: 521, A51, A51. DOI: 10.1051/0004-6361/201014433. arXiv: 1004.5403.

— (Oct. 2010b). "Asymmetries of solar coronal extreme ultraviolet emission lines". In: *Astronomy and Astrophysics* 521, A51. ISSN: 1432-0746. DOI: 10.1051/0004-6361/201014433. URL: http://dx.doi.org/10.1051/0004-6361/201014433.

Peter, H. and P. G. Judge (Sept. 1999). "On the Doppler Shifts of Solar Ultraviolet Emission Lines". In: 522, pp. 1148–1166. DOI: 10.1086/307672.

Prabhakar, M., K. P. Raju, and T. Chandrasekhar (2013). "Analysis of the solar coronal green line profiles from eclipse observations". In: *Astronomical Society of India Conference Series*. Vol. 10. Astronomical Society of India Conference Series. arXiv: 1307.0352.

Prabhakar, Maya and K. P. Raju (May 2022). "Line Profile Studies of Coronal Active Regions in Fe XII λ195.12 Using Hinode/EIS". In: 931.1, 40, p. 40. DOI: 10.3847/1538-4357/ac610e. arXiv: 2205.11441 [astro-ph.SR].

Prabhakar, Maya, K. P. Raju, and T. Chandrasekhar (Mar. 2019). "Characteristics of the Solar Coronal Line Profiles from Fabry-Perot Interferometric Observations". In: 294.3, 26, p. 26. DOI: 10.1007/s11207-019-1409-7. arXiv: 1901.11328.

Prasad, S. K., J. Singh, and D. Banerjee (Feb. 2013). "Variation of Emission Line Width in Mid- and High-Latitude Corona". In: 282, pp. 427–442. DOI: 10.1007/s11207-012-0160-0. arXiv: 1210.6434.

Raju, K. P. (Apr. 1999). "The Effect of Mass Motions Inside the Coronal Loops on Emission Line Profiles". In: 185, pp. 311–322. DOI: 10.1023/A:1005128428916.

Raju, K. P., T. Chandrasekhar, and N. M. Ashok (July 2011a). "ANALYSIS OF CORONAL GREEN LINE PROFILES: EVIDENCE OF EXCESS BLUESHIFTS". In: *The Astrophysical Journal* 736.2, p. 164. DOI: 10.1088/0004-637x/736/2/164. URL: https://doi.org/10.1088%2F0004-637x%2F736%2F2%2F164.

— (Aug. 2011b). "Analysis of Coronal Green Line Profiles: Evidence of Excess Blueshifts". In: 736, 164, p. 164. DOI: 10.1088/0004-637X/736/2/164. arXiv: 1106.3206.

Raju, K. P., J. N. Desai, et al. (Aug. 1993). "Line-Of Velocities Observed in the Inner Solar Corona during the Total Solar Eclipses of 1980 and 1983". In: 263, p. 789. DOI: 10.1093/mnras/263.3.789.

Reames, DV, IG Richardson, and K-P Wenzel (1992). "Energy spectra of ions from impulsive solar flares". In: *The Astrophysical Journal* 387, pp. 715–725.

Sakao, Taro et al. (2007). "Continuous Plasma Outflows from the Edge of a Solar Active Region as a Possible Source of Solar Wind". In: *Science* 318.5856, pp. 1585–1588. ISSN: 0036-8075. DOI: 10.1126/science.1147292. eprint: https://science.sciencemag.org/content/318/5856/1585.full.pdf. URL: https://science.sciencemag.org/content/318/5856/1585.

Scatliff, J. (July 1973). "An observation of the total solar eclipse of 1972 July 10." In: *Journal of the British Astronomical Association* 83, pp. 330–334.

Singh, J., A. K. Saxena, and M. K. V. Bappu (Sept. 1982). "Eclipse observations of coronal emission lines. I - Forbidden Fe X 6374 A profiles at the eclipse of 16 February 1980". In: *Journal of Astrophysics and Astronomy* 3, pp. 249–266. DOI: 10.1007/BF02714865.

Stellmacher, G., S. Koutchmy, and C. Lebecq (July 1986). "The 1981 total solar eclipse. III - Photometric study of the prominence remnant in the reversing south polar field". In: 162.1-2, pp. 307–311.

Team, Hinode Review et al. (Oct. 2019). "Achievements of Hinode in the first eleven years". In: *Publications of the Astronomical Society of Japan* 71.5. R1. ISSN: 0004-6264. DOI: 10.1093/pasj/psz084. eprint: https://academic.oup.com/pasj/article-pdf/71/5/R1/30161340/psz084.pdf. URL: https://doi.org/10.1093/pasj/psz084.

Thorne, Anne P and Chapman Spectrophysics (1974). *Hall Ltd.*

Tian, Hui, Louise Harra, et al. (Mar. 2021). "Upflows in the Upper Solar Atmosphere". In: 296.3, 47, p. 47. DOI: 10.1007/s11207-021-01792-7. arXiv: 2102.02429.

Tian, Hui, Scott W. McIntosh, Bart De Pontieu, et al. (Aug. 2011). "TWO COMPONENTS OF THE SOLAR CORONAL EMISSION REVEALED BY EXTREME-ULTRAVIOLET SPECTROSCOPIC OBSERVATIONS". In: *The Astrophysical Journal* 738.1, p. 18. DOI: 10.1088/0004-637x/738/1/18. URL: https://doi.org/10.1088%2F0004-637x%2F738%2F1%2F18.

Tian, Hui, Scott W. McIntosh, Tongjiang Wang, et al. (Oct. 2012). "PERSISTENT DOPPLER SHIFT OSCILLATIONS OBSERVED WITHHINODE/EIS IN THE SOLAR CORONA: SPECTROSCOPIC SIGNATURES OF ALFVÉNIC WAVES AND RECURRING UPFLOWS". In: *The Astrophysical Journal* 759.2, p. 144. DOI: 10.1088/0004-637x/759/2/144. URL: https://doi.org/10.10882F0004-637x2F7592F22F144.

Tian, Hui, Chuanyi Tu, et al. (Jan. 2010). "THE NASCENT FAST SOLAR WIND OBSERVED BY THE EUV IMAGING SPECTROMETER ON BOARD HINODE". In: *ApJL* 709.1, pp. L88–L93. DOI: 10.1088/2041-8205/709/1/l88. URL: https://doi.org/10.1088%2F2041-8205%2F709%2F1%2Fl88.

Tripathi, Durgesh and James A. Klimchuk (Nov. 2013). "ASYMMETRIES IN CORONAL SPECTRAL LINES AND EMISSION MEASURE DISTRIBUTION". In: *The Astrophysical Journal* 779.1, p. 1. DOI: 10.1088/0004-637x/779/1/1. URL: https://doi.org/10.1088%2F0004-637x%2F779%2F1%2F1.

Turgeon, E.C. and G.G. Shepherd (1962). "Upper atmospheric temperatures from Doppler line widths—II: Measurements on the OI 5577 and OI 6300 Å lines in aurora". In: *Planetary and Space Science* 9.6, pp. 295–304. ISSN: 0032-0633. DOI: https://doi.org/10.1016/0032-0633(62)90020-X. URL: https://www.sciencedirect.com/science/article/pii/003206336290020X.

van de Hulst, H. C. (1953). "The Chromosphere and the Corona". In: *The Sun*. Ed. by Gerard Peter Kuiper, p. 207.

Warren, Harry P., Ignacio Ugarte-Urra, George A. Doschek, et al. (Oct. 2008). "Observations of Active Region Loops with the EUV Imaging Spectrometer on Hinode". In: 686.2, p. L131. DOI: 10.1086/592960. arXiv: 0808.3227 [astro-ph].

Warren, Harry P., Ignacio Ugarte-Urra, and Enrico Landi (July 2014). "The Absolute Calibration of the EUV Imaging Spectrometer on Hinode". In: 213.1, 11, p. 11. DOI: 10.1088/0067-0049/213/1/11. arXiv: 1310.5324 [astro-ph.SR].

Watanabe, Tetsuya et al. (Nov. 2007). "Temperature and Density Structures of Solar Corona, A Test of Iron Line Diagnostic Capability of EIS Instrument on Board Hinode". In: 59, S669. DOI: 10.1093/pasj/59.sp3.S669.

Withbroe, George L. and Robert W. Noyes (1977). "Mass and Energy Flow in the Solar Chromosphere and Corona". In: *Annual Review of Astronomy and Astrophysics* 15.1, pp. 363–387. DOI: 10.1146/annurev.aa.15.090177.002051. eprint: https://doi.org/10.1146/annurev.aa.15.090177.002051. URL: https://doi.org/10.1146/annurev.aa.15.090177.002051.

Yardley, S. L., D. H. Brooks, and D. Baker (June 2021). "Widespread occurrence of high-velocity upflows in solar active regions". In: 650, L10, p. L10. DOI: 10.1051/0004-6361/202141131. arXiv: 2106.01396.

Young, P. R., B. O'Dwyer, and H. E. Mason (Jan. 2012). "Velocity Measurements for a Solar Active Region Fan Loop from Hinode/EIS Observations". In: 744.1, 14, p. 14. DOI: 10.1088/0004-637X/744/1/14. arXiv: 1107.2362 [astro-ph.SR].

Young, Peter R. et al. (Nov. 2007). "EUV Emission Lines and Diagnostics Observed with Hinode/EIS". In: 59, S857. DOI: 10.1093/pasj/59.sp3.S857. arXiv: 0706.1857 [astro-ph].